https://doi.org/10.1016/j.pecs.2017.06.001


# Advances in modeling and simulation of Li-air batteries

Peng Tan[1], Wei Kong[1,2], Zongping Shao[3,4], Meilin Liu[5,*], Meng Ni[1,6] *

1 Department of Building and Real Estate, The Hong Kong Polytechnic University, Hung Hom, Kowloon, Hong Kong, China
2 School of Energy and Power Engineering, Jiangsu University of Science and Technology, Jiangsu 212003, China
3 Jiangsu National Synergetic Innovation Center for Advanced Material, College of Energy, State Key Laboratory of Materials-Oriented Chemical Engineering, Nanjing Tech University, Nanjing 210009, China
4 Department of Chemical Engineering, Curtin University, Perth, WA 6845, Australia
5 School of Materials Science and Engineering, Center for Innovative Fuel Cell and Battery Technologies, Georgia Institute of Technology, Atlanta, GA 30332-0245, USA
6 Environmental Energy Research Group, Research Institute for Sustainable Urban Development (RISUD), The Hong Kong Polytechnic University, Hung Hom, Kowloon, Hong Kong, China

**Abstract:** Li-air batteries have potential to be the next generation power sources for various applications, from portable devices to electric vehicles and microgrids, due largely to their significantly higher theoretical energy densities than those of the existing batteries. The commercialization of this technology, however, is hindered by a variety of technical hurdles, including low obtainable capacity, poor energy efficiency, and limited cycle life. Breakthrough to these barriers requires a fundamental understanding of the complex electrochemical and transport behaviors inside the batteries. Mathematical modeling and simulation are imperative in gaining important insight into the mechanisms of these complex phenomena, which is vital to achieving rational designs of better materials for high-performance batteries. In this paper, we present a comprehensive review of the latest advances in modeling and simulation of Li-air batteries and offer our perspectives on new directions of future development. Unlike previous reviews that centered mainly on continuum modeling of non-aqueous Li-air batteries, the present

paper focuses on mathematical descriptions of the detailed transport and electrochemical processes in different types of Li-air batteries. We start with a brief introduction to the working principles of Li-air batteries. Then, the governing equations for mass transport and electrochemical reactions in non-aqueous Li-air batteries are formulated, including lithium ion and oxygen transport in the porous air electrode, the formation of solid discharge products, the kinetics of electrode reactions, the evolution of electrode structure, the distribution of active sites, the effect of the side reactions during cycling, the phenomena of the volume change, and the charge process. In addition, the modeling and simulations of aqueous and hybrid Li-air batteries are reviewed, highlighting the phenomena that are different from those in the non-aqueous ones. Finally, the challenges facing the modeling and simulation of Li-air batteries are discussed and perspectives for the development of a new generation of Li-air batteries are outlined.

**Keywords:** Li-air battery; Modeling; Working behavior; Mechanism; Challenges

## Contents

## 1. Introduction

The rapid development of advanced electronic devices and electric vehicles results in a great demand for high-energy-density storage systems [1]. To date, rechargeable lithium-ion batteries are the most widely used power sources for portable and mobile applications because of their reasonable energy density, rate capability, and cycle life [2]. During charge, lithium ions are extracted from a positive electrode material (e.g., a layered intercalation compound $LiFePO_4$ or $LiCoO_2$) and inserted into or reacted with a negative electrode material (e.g., graphite). During discharge, all the electrochemical processes proceed in the reverse direction [3]. The low theoretical capacity of the positive electrode materials, however, limits the energy density of the existing lithium-ion batteries to about 500−700 Wh $kg^{-1}$, which is insufficient for many emerging applications (e.g., electric vehicles) [4]. Thus, the exploitation of new energy storage technologies with much higher energy density is still a grand challenge.

Among various emerging energy storage technologies, metal-air batteries have the greatest potential for dramatically enhancing energy density, especially lithium-air, aluminum-air, and zinc-air batteries [5]. In these types of batteries, a pure metal is used as the negative electrode rather than an intercalation compound. Different from the intercalation reaction mechanism, oxygen enters the porous air electrode and participates in the oxygen reduction reaction (ORR) during the discharge process. The charge process is the reversed one through the oxygen evolution reaction (OER) to produce metal and oxygen. As oxygen can be obtained directly from ambient air, minimizing the required mass and volume of the air electrode, the energy density of a metal-air battery theoretically relies on the metal electrode only. Among the metal-air batteries, the

lithium-air (Li-air) battery has garnered the most attention, due largely to the lowest equivalent weight of lithium metal, corresponding to a theoretical energy density of ~11,680 Wh $kg^{-1}$, which is close to that of gasoline (~13,000 Wh $kg^{-1}$) [6].

A prototype rechargeable Li-air battery was demonstrated by Abraham and Jiang in 1996 [7], in which a polymer electrolyte composed of a lithium salt and carbonate-based solvents was used, and the reversibility was achieved through the hypothesized formation and decomposition of lithium oxides. Since then, many advancements have been made due to worldwide attention, and various types of Li-air batteries have been proposed and developed [6]. During discharge, lithium metal is oxidized at the lithium electrode (or anode), producing electrons and lithium ions. Oxygen is reduced at the air electrode (or cathode) and combined with lithium ions in the electrolyte to form the discharge product. During charge, the electrochemical processes are reversed. The discharge product is electrochemically oxidized at the air electrode, producing electrons, lithium ions, and oxygen [8]. Notably, the discharge product depends on the type of electrolytes used in the battery. In aqueous electrolytes, the product dissolves first and starts to precipitate when reaching its solubility. In non-aqueous electrolytes, on the contrary, the product is insoluble and deposits on the electrode surface from the beginning. Accordingly, careful design of the air (positive) electrode is vital to the performance of Li-air batteries based on different types of electrolytes.

The development of a high-performance rechargeable Li-air battery requires a profound understanding of the electrochemical and transport processes, the utilization of suitable electrolyte and electrode materials, and the design of proper battery structures. Tremendous efforts have been made in the recent decade to make Li-air batteries

commercially viable. Various electrolyte and electrode materials have been fabricated and tested [9,10]. The reaction, degradation, and failure mechanisms have been investigated and proposed [11]. Advanced characterization techniques and devices have been developed and utilized [12,13]. Although some breakthroughs have been made, the development of Li-air batteries is still in the early stage with many technical difficulties, such as the relatively low obtainable discharge capacity, poor rate capability, low energy efficiency, and limited cycle life [11]. In addition to the experimental explorations, modeling is a powerful and economical tool for understanding the working processes, evaluating the material capabilities, and improving the battery performance [14].

An overview of modeling techniques used for battery-related applications is shown in **Fig. 1**, which presents the modeling or simulation methods' relative computational cost (not to scale) versus the approximate characteristic time and length scales that they can resolve [15]. At the most fundamental level are *ab initio* molecular dynamics and *ab initio* methods such as density functional theory (DFT), which allow the calculation of reaction pathways and the corresponding activation energies to predict the stability, electrical conductivity, and catalytic activity of materials. However, the expense of these methods depends on the time scales of the electronic structure and the numerous interactions between atoms and molecules, and the computing power limits the size of the unit cell to roughly 100 atoms [16]. Molecular dynamics (MD) and Monte Carlo (MC) approaches use predetermined force fields to dictate molecular interactions instead of detailed calculations of the electronic structure [17]. Thus, the computational load can be reduced tremendously, allowing the treatment of a considerably larger system of molecules. Possible applications include the determination of diffusion coefficients and

kinetic parameters (MD) or properties of phase equilibrium like surface tension and vapor pressure (MC) [18]. Discrete element and phase field methods are often used to study the formation and evolution of grain and microstructure. The transport phenomena in discrete microstructures may be captured using methods built upon the Boltzmann transport equation like the lattice Boltzmann method (LBM), which is applicable from free molecular to the continuum scales and enables the use of a low resolution and regular mesh [19]. Continuum modeling methods rely on the conservation equations for mass, momentum, and total energy, such as species equation, Navier-Stokes equations, and energy equation. These methods are typically discretized using a finite element or finite volume approach and have a large range of applications such as studying transport and reaction mechanisms in electrochemical systems [20]. Generally, the computational cost tends to decrease with increasing time and length scales [21]. Combining the continuum models at the macroscopic level with high predictive capabilities toward the material atomistic, chemical and structural properties (microscopic level) results in a multiscale modeling, and two strategies are usually used [22]: top-down approach and bottom-up approach. For a top-down approach, a system is broken down into its compositional sub-systems, each of which is then refined in greater detail, until the entire specification is reduced to base elements. While the bottom-up approach is the opposite process, in which original sub-systems are pieced together to give rise to a more complex system. For instance, the electrolyte properties and the electrode architectures are first determined, and then give more accurate performance prediction of the battery system. Owing to the comprehensive scope and information of the battery system, a multiscale modeling is

crucial to elucidate the mechanisms of coupled electrochemistry and transport behaviors as well as shed light on the methods for performance improvement [23].

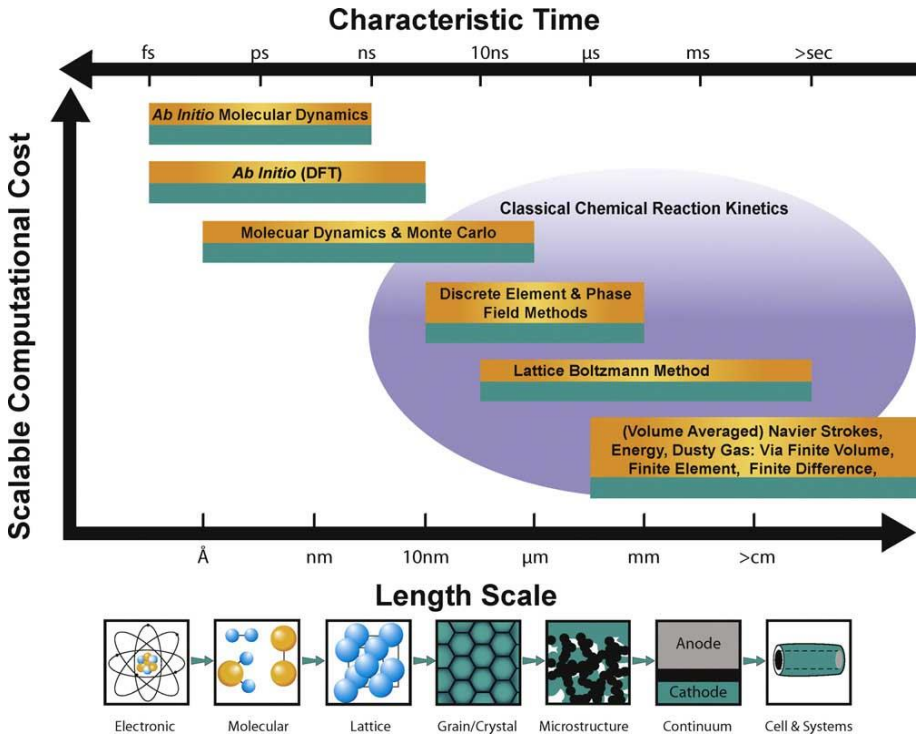


**Fig. 1** An overview of modeling techniques for battery-related applications. Reprinted from [15] with permission of Elsevier.

In the past decade, an impressive amount of review papers about Li-air batteries have been published with focuses on the electrolyte solvents and salts [24-26], electrode materials and structures [27-33], and mechanism investigations [34,35]. For example, Franco and Xue discussed the scientific and technological challenges for carbon-based electrodes from a modeling perspective [36]. Yuan *et al.* reviewed the transport governing equations commonly used for macroscopic continuum models [37]. Li *et al.* summarized the macroscopic modeling studies and relevant property data for numerical investigations [38]. These reviews focus on modeling Li-air batteries with non-aqueous electrolytes. However, a comprehensive review that summarizes the modeling of Li-air

batteries with other types of electrolytes, comparing the similarities and differences in modeling, is still lacking. In addition, the mathematical descriptions about some detailed phenomena, especially those that are hard to capture through continuum models, such as the product morphology formation, the transport through the $Li_2O_2$, and the pore structure evolution, have been rarely summarized and discussed. In this article, we try to provide a comprehensive review of the latest developments in modeling and simulation of different types of Li-air batteries. Although *ab initio* models (e.g., DFT) play a crucial role in unraveling the reaction routes and selecting suitable materials [39-44], the present paper focuses on models describing the transport and electrochemical processes in Li-air batteries. We first introduce the working principles and challenges of different types of Li-air batteries. Then, the governing equations for mass transport and electrochemical reactions in non-aqueous Li-air batteries are presented in detail, including lithium ion and oxygen transport in the porous air electrode, the precipitation of the solid product $Li_2O_2$, the kinetics of electrode reactions, the evolution of electrode structure, the distribution of active sites, the effect of the side reactions during cycling, the phenomena of the volume change, and the charge process. Moreover, the similarities and differences in modeling non-aqueous, aqueous and hybrid Li-air batteries are summarized. Finally, remaining challenges and new directions for modeling Li-air batteries are highlighted and discussed.

## 2. Working principles of Li-air batteries

Based on the type of electrolyte used, Li-air batteries can be classified into four types: non-aqueous, aqueous, hybrid non-aqueous/aqueous (or "hybrid" for short), and solid-state Li-air batteries, as schematically shown in **Fig. 2**. The working principles, important findings, and remaining challenges are introduced in this section.

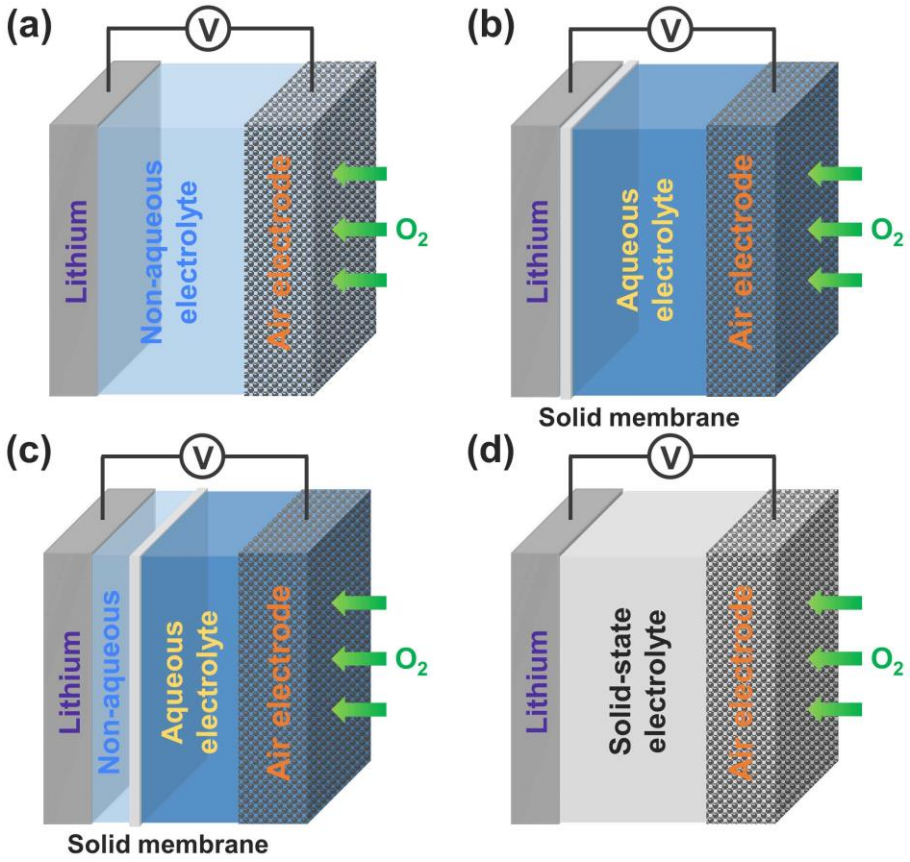


**Fig. 2** Schematic configurations for four types of Li-air batteries: (a) non-aqueous; (b) aqueous; (c) hybrid; and (d) solid-state.

### 2.1 Non-aqueous Li-air batteries

A typical non-aqueous Li-air battery consists of a lithium metal electrode, a porous air electrode with active materials, and an electrolyte made of a lithium salt in an aprotic solvent, as shown in **Fig. 2a**. In order to prevent the internal short-circuit between the lithium metal electrode and the air electrode, a porous separator (glass microfiber filter or propylene membrane) is usually used between them [45].

In the early stage, carbonate-based electrolytes (e.g., ethylene carbonate, EC; dimethyl carbonate, DMC) were applied in non-aqueous Li-air batteries due to their

successful application in lithium-ion batteries. However, the battery performance was poor with short cycle life [46-48]. It was quickly found that due to the poor stabilities of electrolytes to the formed highly oxidative species [49,50], the discharge products were irreversible lithium carbonate and lithium alkylcarbonate rather than reversible lithium peroxide ($Li_2O_2$) [51-53]. Accordingly, other non-aqueous electrolyte systems with improved stabilities against superoxide radicals and oxidation potentials were formulated to ensure longer cycle life, such as dimethoxyethane (DME) [54-57], tetraethylene glycol dimethyl ether (TEGDME) [58-65], and dimethyl sulfoxide (DMSO) [66-68]. During discharge, lithium metal is oxidized at the anode, producing electrons and lithium ions as:

$$Li \rightarrow Li^+ + e^- \quad (I)$$

Oxygen dissolved in the electrolyte first reduces at the cathode active surfaces through a one-electron transfer:

$$O_2 + e^- \rightarrow O_2^- \quad (II)$$

The formed superoxide ions combine with lithium ions to form the intermediate product lithium superoxide ($LiO_2$), followed by a disproportionation reaction:

$$2LiO_2 \rightarrow Li_2O_2 + O_2 \quad (IIIa)$$

and/or a second one-electron-transfer electrochemical process as:

$$LiO_2 + Li^+ + e^- \rightarrow Li_2O_2 \quad (IIIb)$$

to form the final product $Li_2O_2$. The total reaction is

$$O_2 + 2Li^+ + 2e^- \rightarrow Li_2O_2 \ (E^0=2.96 \text{ V vs. } Li/Li^+) \quad (IV)$$

Since $Li_2O_2$ is insoluble in the non-aqueous electrolyte, it deposits on the surface of the porous air electrode and accumulates in the void volume with an increase in the capacity, and eventually may block the electrode pores, affecting the transport of oxygen

and lithium ion [69]. In addition, due to the insulator nature of $Li_2O_2$, it is believed that the thickness of $Li_2O_2$ should have a limitation otherwise the electron transport will be blocked as well [70]. As a result, a film-like morphology of $Li_2O_2$ covering the air electrode surfaces is expected [71]. However, various kinds of $Li_2O_2$ morphologies have been observed, from films with thicknesses of several nanometers [71,72] to large particles of a few hundred nanometres and even micrometers [73,74]. To explain the formation of different $Li_2O_2$ morphologies, Bruce *et al.* proposed two mechanisms: the solution mechanism and the surface mechanism [75]. In the solution mechanism, two soluble $LiO_2$ molecules disproportionate to form $Li_2O_2$ with particle-like morphology (Reaction IIIa). In the surface mechanism, two sequential one-electron transfer steps to yield insoluble $Li_2O_2$ at the electrode surface with film-like morphology (Reaction IIIb). Hence, the detailed mechanism is governed by the competition between the $LiO_2$ solubility and the adsorption free energy of $LiO_2$ on the air electrode. For an electrolyte, both the solvent and the dissolved lithium salt can determine the $LiO_2$ solubility [76-78], affecting the reaction route. When the electrolyte is given, as different cathode surfaces have different adsorption energies, the electrode material can thus affect the reaction mechanism as well [79-81]. For instance, an electrode made of reduced graphene oxide with added iridium nanoparticles is able to stabilize the intermediate product $LiO_2$, achieving a non-aqueous Li-air battery based on $LiO_2$ instead of $Li_2O_2$ [82].

During charge, the decomposition of solid $Li_2O_2$ to lithium and oxygen is needed to make the battery rechargeable. The reaction is thought to be a direct two-electron process:

$$Li_2O_2 \rightarrow 2Li^+ + 2e^- + O_2 \qquad (V)$$

and/or a one-electron process involves the formation of $LiO_2$ as:

$$Li_2O_2 \rightarrow Li^+ + e^- + LiO_2 \quad \text{(VI)}$$

Due to the insulator nature of bulk $Li_2O_2$ [70], the charge overpotential is surprisingly high (>1.0 V) [12], leading to low energy efficiency. In addition, such a high charge potential can cause the decomposition of electrolyte and electrode materials, rendering the irreversible side products, which cover the active surfaces and consequently limit the battery's cycle life [83]. To facilitate the OER process, various kinds of catalyst materials have been used in the air electrode, and improved energy efficiency has been achieved [84-86]. However, the detailed mechanisms of $Li_2O_2$ oxidation are still under investigation [87-91]. It is also worth noting that different from the OER process in aqueous solutions, the kinetics of the OER in non-aqueous Li-air batteries is not only determined by the electrode materials, but also affected by how the solid $Li_2O_2$ is produced (e.g., morphology, composition), which is correlated with the ORR process [92]. Hence, the study of the OER process should also take the ORR process into consideration.

In short, the discharge process for non-aqueous Li-air batteries is the formation of solid $Li_2O_2$ at the two-phase boundaries between the electrolyte (liquid) and the active material (solid) in the porous cathode [93], and the electrochemical decomposition of $Li_2O_2$ during the charge process enables the rechargeability. However, a practical battery suffers from the low discharge capacity, low energy efficiency, and limited cycle life. Searching for stable electrolyte and electrode materials, optimizing the cathode structure to improve transport kinetics, and applying effective catalysts to increase reaction rates are the keys for solving these issues. In addition, most reported non-aqueous Li-air batteries were operated in a pure oxygen atmosphere rather than the ambient air [94] to avoid contamination from other gases (e.g., $CO_2$, $H_2O$), which may cause the formation

of irreversible side products [95], leading to rapid performance degradation or even operation failure [96]. In an open atmosphere, how to suppress the evaporation of liquid electrolytes during long-term operation is another important topic [97,98]. Moreover, due to the crossover of oxygen and other soluble species, the reactions on the interface between the lithium electrode and the electrolyte are complicated and result in a severe contamination of lithium metal [99-101]. Consequently, protecting the lithium metal through suitable membranes or passivation films, as well as solving the safety issues (e.g., dendrite formation) [102-106], are also crucial for practical applications of non-aqueous Li-air batteries.

**2.2 Aqueous and hybrid Li-air batteries**

To address the issues caused by the solid product $Li_2O_2$ in non-aqueous systems, a new type of Li-air batteries based on the aqueous solution was proposed by Visco *et al.* in 2004 [107]. As schemed in **Fig. 2b**, an aqueous Li-air battery is basically made up of a lithium electrode and a porous air electrode with an aqueous electrolyte, and a solid-state membrane in between as the separator [108-113]. Different from that in non-aqueous systems where the separator is a porous structure saturated with non-aqueous electrolyte, the separator in the aqueous system is a dense lithium ion conducting membrane (e.g., NASICON-type glass ceramics) so that the lithium electrode can be protected from the aqueous electrolyte. To avoid the reaction between the lithium metal and the solid membrane (e.g., $Li_{1+x}Al_xTi_{2-x}(PO_4)_3$, LATP) and to facilitate lithium ion transport, a polymer buffer layer is usually used [114]. Replacing the polymer buffer layer with a non-aqueous electrolyte leads to a hybrid non-aqueous/aqueous system [115-120], as shown in **Fig. 2c.**

The basic reaction mechanisms in aqueous solutions are general ORR and OER processes as:

$$O_2 + 2H_2O + 4e^- \leftrightarrow 4OH^- \quad \text{(VII)}$$

Combining with the reaction in the lithium electrode (Reaction I) leads to the whole reaction as:

$$4Li + O_2 + 2H_2O \leftrightarrow 4Li^+ + 4OH^- \ (E^0=3.45 \text{ V vs. } Li/Li^+) \quad \text{(VIII)}$$

Instead of forming solid $Li_2O_2$, the discharge product is lithium hydroxide (LiOH), which can dissolve in aqueous electrolytes. Hence, the active surfaces in the air electrode are not affected and a high power density may be delivered [115]. Besides, electrocatalysts applied in aqueous solutions can be used to lower the overpotentials during discharge and charge [9]. However, the solubility of LiOH is limited to 5.25 M at room temperature, otherwise $LiOH \cdot H_2O$ precipitates as:

$$Li^+ + OH^- + H_2O \rightarrow LiOH \cdot H_2O_{(deposit)} \quad \text{(IX)}$$

which results in the similar phenomena as observed in non-aqueous Li-air batteries. The solubility of LiOH can be effectively increased through the use of lithium acetate salts [109,110], since water acts as one reactant in the discharge process. However, the amount of discharge products is limited to the amount of available solvent, resulting in the lower theoretical energy densities of aqueous/hybrid Li-air batteries than those of non-aqueous ones [121,122].

In aqueous and hybrid Li-air batteries, an important component is the solid-state membrane, which not only protects lithium metal but also transports lithium ions from the anode to the aqueous electrolyte. Hence, a membrane with high stabilities in aqueous electrolytes and high lithium ion conductivity is required [110,112,123]. In addition, for

the safety concern, the battery structure should be robust enough in various operating conditions [111]. Moreover, searching for inexpensive alternative catalysts to noble metals (e.g., Ru, Ir), especially with bifunctional catalytic activities, is an ultimate target for performance improvement and cost reduction [124,125].

### 2.3 Solid-state Li-air batteries

The above-mentioned three types of Li-air batteries are mainly based on liquid electrolytes, which may cause the leakage and safety issues. A solution is to develop a solid-state Li-air battery without using any liquid electrolytes, as schemed in **Fig. 2d**. A typical solid-state Li-air battery contains a lithium electrode, a solid-state electrolyte membrane, and a porous air electrode [126]. The electrochemical reactions occur at the triple-phase boundaries among the solid electrolyte (lithium ion conductor), the air electrode skeleton (electron conductor), and gaseous oxygen. Similar to non-aqueous Li-air batteries, the discharge product in solid-state Li-air batteries is identified to be solid $Li_2O_2$ and the charge process involves its electrochemical decomposition [126], but detailed reaction mechanisms are still lacking in the literature [127].

Solid-state Li-air batteries have attractive features in better safety and stability than others with liquid electrolytes. However, the obstacles for a high battery performance lie in the high lithium ion transport resistance in the solid-state electrolyte membrane and limited reaction boundaries among the solid-state electrolyte, the air electrode, and gaseous oxygen. Till now, various types of solid-state electrolyte have been proposed and tested, including NASICON-type glass ceramic [127-132], single-crystalline silicon membranes [133], and polymer-based membranes [134], while a membrane with a high

lithium ion conductivity is in an urgent demand. To extend the reaction boundaries, novel air electrode architectures should also be developed [135].

Among the four types of Li-air batteries, the non-aqueous system has the simplest structure and also shows the high reversible capacity [136], and thus attracts the most research attention [137]. Since each configuration has specific pros and cons but with definite scientific and engineering challenges, the ultimate choice for the best one is still an open question [36]. It should be noted that in different systems, some phenomena are similar. For instance, in both aqueous and non-aqueous electrolyte, oxygen first dissolves into the liquid electrolyte and then transports to the active sites. When the discharge product ($Li_2O_2$ or LiOH) reaches its solubility, precipitation occurs in the porous electrode, leading to decreased amount of the active sites and an increase in the resistance for lithium ion and oxygen transport. Therefore, it is of paramount importance to conduct mathematical modeling and simulation to gain important insight into the mechanisms of these complex phenomena so as to achieve rational design for performance improvement.

## 3. Modeling of non-aqueous Li-air batteries

As introduced in Section 2.1, a typical non-aqueous Li-air battery is made up of a lithium electrode (or anode) and a porous air electrode (or cathode) with a non-aqueous electrolyte, and a porous separator (not shown in **Fig. 2a**). However, as the separator is saturated with electrolyte, oxygen can be dissolved and easily transported to the lithium metal which consequently cause severe contaminations [100]. A solution to address this issue is to use an anode protective layer (APL, e.g., LATP) to block the oxygen crossover as demonstrated experimentally [138,139]. In the modeling work, the concept of APL has also been assumed to avoid the complex descriptions of side reactions occurring on the

lithium surface. The computation domain of a non-aqueous Li-air battery is schematically shown in **Fig. 3a** [140]. Although lithium dissolution and deposition during the discharge and charge processes are important for the lithium electrode [102,103,141-143], as both ORR and OER occur in the porous air electrode, the transport process inside this electrode considerably affect the battery performance [144]. Hence, the main modeling domain is the electrolyte saturated parts, including the porous separator ($L_A$−L) and the air electrode ($L_C$−L), but the analyses usually focus on the air electrode. At the lithium electrode/separator interface ($x = L_A$), lithium metal is electro-oxidized to compensate the consumption of $Li^+$ and electric migration in the electrolyte, while the oxygen concentration is set to be zero. At the separator/air electrode interface ($x = L_C$), the continuous boundary conditions are specified for the fluxes of species (lithium ion, oxygen). At the air electrode/oxygen interface ($x$ = L), the oxygen concentration is estimated from the oxygen solubility and the external concentration (oxygen partial pressure), and the flux of each species (lithium ion, oxygen) is set to be zero. It is noted that there are two types of air electrodes reported, as schematically shown in **Fig. 3b**. One type is an integrated electrode directly made of active materials decorated substrates/current collector (e.g., nickel form, stainless steel felt) [145-150] with the thickness of 100−800 μm. In this case, the air electrode is homogeneous and is considered in most modeling works [38]. Due to the low transport coefficients of lithium ion and oxygen in non-aqueous electrolytes, a non-uniform distribution of species can be found, resulting in the low utilization of the electrode. To improve the transport kinetics and the utilization of active materials, the other type of electrode is composed of a thin active layer (<10 μm) on a gas diffusion layer/current collector (>100 μm, e.g., carbon

paper) [151-153] or a porous support (>25 μm) [154,155]. Hence, the real part that participates in reactions is the thin active layer rather than the whole electrode. In this review, unless specified otherwise, the term “air electrode” still refers to the active layer. Since the values of parameters used in modeling can tremendously affect the accuracy, we focus on introducing the mathematical descriptions of transport and electrochemical processes occurring at the air electrode instead of judging the accuracy of results. Owing to the low current densities in present non-aqueous Li-air batteries, the temperature changes are found to be negligible [156,157] so that the thermal effects are not considered in the introduced works.

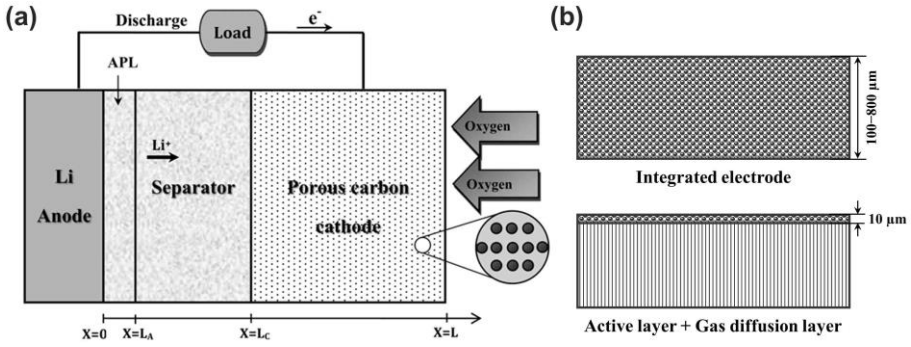


**Fig. 3** Schematic of (a) computation domain of a non-aqueous Li-air battery during discharge operation, the inset demonstrates the discharge products covering on the surface. Reprinted from [140] with permission of Elsevier. (b) two types of air electrodes.

### 3.1 Lithium ion transport

In the early models of non-aqueous Li-air batteries, the lithium ion ($Li^+$) transport was not considered [158,159] since its concentration in the electrolyte is sufficiently higher (1.0 M) than that of dissolved oxygen (~$10^{-3}$ M) [160,161]. Later on, to develop a comprehensive model of non-aqueous Li-air batteries, the $Li^+$ transport part was also included [162,163]. This problem looks very similar to that in lithium-ion batteries, for

which numerous attempts have been made to deal with the $Li^+$ transport in the electrolyte. Generally, three modeling approaches have been developed [36]: i) the coupled Poisson-Nernst-Planck equation that treats the transport of cations and anions as independent [164,165]; ii) the concentrated solution theory that considers the transport of both cations and anions and the role of solvent [166-168]; iii) the approach based on the electroneutrality assumption and a strict convection-free condition [169]. Since the lithium salt concentration in the electrolyte is usually 1.0 M or higher [170], the concentrated solution theory has been widely used in non-aqueous Li-air batteries [171-173]. In the porous air electrode, the conservation of $Li^+$ in the electrolyte is expressed as:

$$\frac{\partial(\varepsilon_e c_{Li^+})}{\partial t} = -\nabla \cdot \boldsymbol{N}_{Li^+} + S_{Li^+} \tag{1}$$

where $c_{Li^+}$ is the bulk concentration of $Li^+$ which is averaged over the volume of the electrolyte in the pores, $\varepsilon_e$ is the volume fraction of the electrolyte in the air electrode and changes with the volume fraction of the products ($\varepsilon_p$). The relationship between the volume fraction of electrolyte, solid product, and electrode porosity ($\varepsilon$) is:

$$\varepsilon_e + \varepsilon_p = \varepsilon \tag{2}$$

$S_{Li^+}$ is the generation or consumptions rates of $Li^+$ due to reactions, $\boldsymbol{N}_{Li^+}$ is the molar flux of $Li^+$ in the electrolyte. The molar flux of $Li^+$ in the electrolyte is [166,167]:

$$\boldsymbol{N}_{Li^+} = -D_{Li^+}^{eff} \nabla c_{Li^+} + \frac{\boldsymbol{i}_l t_+}{F} + \boldsymbol{u}_e c_{Li^+} \tag{3}$$

where $D_{Li^+}^{eff}$ is the effective diffusion coefficient of $Li^+$, $t_+$ is the transference number of $Li^+$, $F$ is Faraday constant (96485 C $mol^{-1}$), $\boldsymbol{u}_e$ is the electrolyte velocity, and $\boldsymbol{i}_l$ is the current density in the solution phase [174]:

$$\boldsymbol{i}_{\mathrm{l}} = -\kappa^{\mathrm{eff}} \nabla \phi_{\mathrm{l}} - \frac{\nu RT\kappa^{\mathrm{eff}}}{F}\left(\frac{s_+}{n\nu_+} + \frac{t_+}{z_+\nu_+} - \frac{s_0 c}{nc_0}\right)\left(1 + \frac{\partial \ln f_{\pm}}{\partial \ln c}\right)\nabla \ln c \tag{4}$$

where $\kappa^{\mathrm{eff}}$ is the effective ionic conductivity, $\phi_{\mathrm{l}}$ is the potential in the electrolyte, $R$ is the universal gas constant (8.3143 J mol$^{-1}$ K$^{-1}$), $T$ is the temperature in Kelvin, $n$ is the number of electrons transferred, $s_+$ and $s_0$ are the stoichiometric coefficients for cation and solvent, respectively; $\nu_+$ and $\nu$ are the numbers of cation and the number of moles of ions into which a mole of electrolyte dissociates, respectively; $z_+$ is the charge number, $c$ and $c_0$ are the molar concentrations of the electrolyte and solvent in the electrolyte, respectively; $f_{\pm}$ is the activity coefficient of lithium salt. A 1:1 binary electrolyte used in non-aqueous Li-air batteries gives $s_+ = -1$, $\nu_+ = 1$, $z_+ = 1$, $s_0 = 0$, and $\nu = 2$. Appling these values into Eq. 4 gives the current density in the solution phase as:

$$\boldsymbol{i}_{\mathrm{l}} = -\kappa^{\mathrm{eff}} \nabla \phi_{\mathrm{l}} - \frac{2RT\kappa^{\mathrm{eff}}}{F}(t_+ - 1)\left(1 + \frac{\partial \ln f_{\pm}}{\partial \ln c_{\mathrm{Li}^+}}\right)\nabla \ln c_{\mathrm{Li}^+} \tag{5}$$

For the continuum model, the charges are conserved between the solution and solid phases and can be expressed through the divergence of the current density as:

$$\nabla \cdot \boldsymbol{i}_{\mathrm{l}} + \nabla \cdot \boldsymbol{i}_{\mathrm{s}} = 0 \tag{6}$$

where $\boldsymbol{i}_{\mathrm{s}}$ is the current density in the solid phase and is governed by Ohm's law through the electric potential $\phi_{\mathrm{s}}$ as:

$$\boldsymbol{i}_{\mathrm{s}} = -\sigma^{\mathrm{eff}} \nabla \phi_{\mathrm{s}} \tag{7}$$

where $\sigma^{\mathrm{eff}}$ is the effective electronic conductivity of the electrode. The effective parameters $D_{\mathrm{Li}^+}^{\mathrm{eff}}$, $\kappa^{\mathrm{eff}}$ and $\sigma^{\mathrm{eff}}$ in the above equations usually depend on the tortuosity of

individual phase in the porous cathode. These parameters for the porous air electrode are corrected to account for the porosity effect using Bruggeman correlation as:

$$D_{\mathrm{Li}^+}^{\mathrm{eff}} = \varepsilon_{\mathrm{e}}^{\alpha} D_{\mathrm{Li}^+} \tag{8}$$

$$\kappa^{\mathrm{eff}} = \varepsilon_{\mathrm{e}}^{\alpha} \kappa \tag{9}$$

$$\sigma^{\mathrm{eff}} = (1-\varepsilon)^{\alpha} \sigma \tag{10}$$

where $\alpha$ is the Bruggeman coefficient and $\alpha$ = 1.5 has been generally used in modeling [37]. $D_{\mathrm{Li}^+}$, $\kappa$, and $\sigma$ are the diffusion coefficient of the $\mathrm{Li}^+$ in the electrolyte, the ionic conductivity of the electrolyte, and the electrical conductivity of the electrode, respectively. In simple dilute electrolytes containing fully dissociated species, the Nernst-Einstein equation can be used to relate conductivity and ion diffusivity [174,175]. However, this framework does not necessarily apply to concentrated electrolytes or electrolytes that contain ion clusters. For example, in the liquid electrolytes consisting of binary mixtures of lithium bis(trifluoromethanesulfonyl)imide (LiTFSI) and perfluoropolyethers (PFPE) with different end groups, some samples with high diffusivities exhibited low conductivities [176]. This result indicated that an insightful investigation of the relationship in the concentrated solution is required.

However, the $\mathrm{Li}^+$ transport in non-aqueous Li-air batteries is different from that in lithium-ion batteries in several aspects. The first one is that in lithium-ion batteries, $\mathrm{Li}^+$ intercalates into the solid particles across the electrochemical double layer (EDL) region and then diffuses away. In the concentrated solution theory, although the strict electroneutrality condition forbids its application to the EDL region, the high conductivity of the concentrated solution renders the EDL region very narrow, justifying its application in modeling the electrolyte phase transport in lithium-ion batteries [36]. In

non-aqueous Li-air batteries, $Li^+$ reacts with oxygen species to generate the solid product $Li_2O_2$ through different routes (Reactions IIIa and IIIb), making the mechanism complex as introduced in Section 3.3. To capture the detailed kinetics, an explicit treatment of the EDL region is significant, but related works in non-aqueous Li-air batteries are still absent [177]. The Poisson-Nernst-Planck equation may be a useful framework since it allows for the charge separation to describe the regions close to or inside the EDL of the electrodes [164,165], but adjusting it to the concentrated solution is challenging. Second, the electrolyte velocity (Eq. 3) is usually taken as zero in modeling without considering the convection effect [37]. While the consumption of lithium metal and the deposition of the solid product will cause a flow and thus the convection of the electrolyte, which will be introduced later in Section 3.8. Third, due to the formation of the solid product that affects the air electrode structure, the effective diffusion coefficient changes during the discharge process, resulting in the coupled lithium ion transport and reaction kinetics. Besides these aspects, as the electrolyte is a crucial component in non-aqueous Li-air batteries, some novels approaches have been reported to adjust the electrolyte properties for performance enhancement. For instance, room temperature ionic liquids have been used as the solvents to improve the electrochemical stability [178-180]; mixed solvents were applied to improve the stability [181-183] and change the reaction route [184]; more than one kind of lithium salts with different concentrations (e.g., 50 mM LiI and 1 M LiTFSI) were dissolved in the solvent to facilitate the charge process [185]. In these cases, the electrolytes cannot be simply treated as binary solutions and the corresponding modeling may require the development of new theories and methods.

### 3.2 Oxygen transport

In most reported non-aqueous Li-air batteries, the air electrode is flooded with the electrolyte [186], as schemed in **Fig. 4a** [187]. Gaseous oxygen needs to dissolve in the electrolyte first at the air side of the air electrode (**Fig. 3a**, $x$ = L) and then transport to the reaction sites. Similar to the governing equation of lithium ion transport, the conservation for oxygen in the electrolyte is expressed as:

$$\frac{\partial(\varepsilon_{\mathrm{e}} c_{\mathrm{O_2,e}})}{\partial t} = -\nabla \cdot \boldsymbol{N}_{\mathrm{O_2,e}} + S_{\mathrm{O_2,e}} \tag{11}$$

where $c_{\mathrm{O_2,e}}$ is the bulk concentration of oxygen in the electrolyte which is averaged over the volume of the electrolyte in the pores, $\boldsymbol{N}_{\mathrm{O_2,e}}$ is the molar flux of oxygen in the electrolyte. $S_{\mathrm{O_2,e}}$ is the generation or consumptions rates of oxygen due to reactions and is relevant to $S_{\mathrm{Li^+}}$ according to Reaction IV. The molar flux of oxygen in the electrolyte becomes:

$$\boldsymbol{N}_{\mathrm{O_2,e}} = -D^{\mathrm{eff}}_{\mathrm{O_2,e}} \nabla c_{\mathrm{O_2,e}} + \boldsymbol{u}_{\mathrm{e}} c_{\mathrm{O_2,e}} \tag{12}$$

where $D^{\mathrm{eff}}_{\mathrm{O_2,e}}$ is the effective diffusion coefficient of oxygen in the electrolyte and can be corrected to account for the porosity effect using Bruggeman correlation as

$$D^{\mathrm{eff}}_{\mathrm{O_2,e}} = \varepsilon_{\mathrm{e}}^{\alpha} D_{\mathrm{O_2,e}} \tag{13}$$

where $D_{\mathrm{O_2,e}}$ is the diffusion coefficient of oxygen in the electrolyte.

In practical non-aqueous Li-air batteries, due to the limited rate of oxygen transport in the electrolyte [11], the oxygen concentration decreases from the air side to the separator during discharge. The insufficient supply of oxygen near the separator side limits the reaction, causing a large polarization, low utilization of the surface areas and

low discharge capacity [74]. Hence, for a given air electrode, how to optimize the distribution of electrolyte inside electrode pores for facilitating the transport of species is a critical issue. It has been proposed that a wetted electrode is preferred for a battery [162,188], as schemed in **Fig. 4b** [187]. In this scenario, all surfaces of the air electrode are fully wetted by a thin electrolyte layer. In addition, the channel for gaseous oxygen transport from the air side to the inner side is maintained so that gaseous oxygen can rapidly penetrate the entire pore and quickly transport to the reaction sites through the thickness-reduced electrolyte. Since lithium ions are also present on the surface, all areas can be used for electrochemical reaction, resulting in an increased capacity [189-192]. To describe this phenomenon, the oxygen transport in the gas channel region should be considered [193]. The conservation for gaseous oxygen is expressed as:

$$\frac{\partial(\varepsilon_{\mathrm{g}} c_{\mathrm{O_2,g}})}{\partial t} = -\nabla \cdot \boldsymbol{N}_{\mathrm{O_2,g}} + S_{\mathrm{O_2,g}} \tag{14}$$

where $\varepsilon_{\mathrm{g}}$ represents the volume fraction of the gas channel in the electrode, and Eq. 2 should be rewritten as:

$$\varepsilon_{\mathrm{e}} + \varepsilon_{\mathrm{g}} + \varepsilon_{\mathrm{p}} = \varepsilon \tag{15}$$

$c_{\mathrm{O_2,g}}$ is the oxygen concentration in the air, and the saturated oxygen concentration in the electrolyte $c^{\mathrm{sat}}_{\mathrm{O_2,e}}$ is correlated with $c_{\mathrm{O_2,g}}$ using Henry's constant ($H$) as:

$$c^{\mathrm{sat}}_{\mathrm{O_2,e}} = \frac{c_{\mathrm{O_2,g}}}{H} \tag{16}$$

The molar flux of gaseous oxygen, $\boldsymbol{N}_{\mathrm{O_2,g}}$, can be expressed with the similar expression of Eq. 12 as:

$$\boldsymbol{N}_{\mathrm{O_2,g}} = -D^{\mathrm{eff}}_{\mathrm{O_2,g}} \nabla c_{\mathrm{O_2,g}} + \boldsymbol{u}_{\mathrm{g}} c_{\mathrm{O_2,g}} \tag{17}$$

where $D_{O_2,g}^{eff}$ is the effective diffusivity of oxygen gas and $\boldsymbol{u}_g$ is the gas velocity. When the pore radius of the air electrode, *r*, is sufficiently small (usually around tens of nanometer), the gaseous diffusive transport can be controlled by the Knudsen diffusion effect due to molecule to wall collisions as well as molecular diffusion caused by molecular collisions [194]. The Knudsen diffusion coefficient, $D_{O_2,g}^{K}$, can be computed according to the kinetic theory of gases as:

$$D_{O_2,g}^{K} = \frac{2}{3}\left(\frac{8RT}{\pi M_{O_2}}\right)^{1/2} r \tag{18}$$

where $M_{O_2}$ is the molecular weight of oxygen. Hence, the effective diffusivity of oxygen gas is obtained by combining both molecular diffusion ($D_{O_2,g}$) and Knudsen diffusion ($D_{O_2,g}^{K}$) with the effects of porosity and tortuosity of the air electrode using the Bruggeman correlation as:

$$D_{O_2,g}^{eff} = \varepsilon_g^{\alpha}\left(\frac{1}{D_{O_2,g}} + \frac{1}{D_{O_2,g}^{K}}\right)^{-1} \tag{19}$$

Eqs. 17–19 are based on the Fick model (FM), while more complex transport mechanism such as the Stefan Maxwell model (SMM) and the dusty-gas model (DGM) can also be applied [195]. SMM is suitable for multi-component diffusion, but the effects of Knudsen diffusion and pressure gradient in porous media are neglected. Thus, FM and DGM are by far the most frequently used models for simulating transport in porous media. FM is the simplest model with analytical solutions for the flux terms and thus it is the most frequently used in fuel cell and battery simulations. DGM is considered as the most accurate model for porous media transport. However, DGM usually requires

numerical solutions for fluxes and its advantage is significant for multi-component transport. The validations of FM and DGM in solving the mass transport accompanied by chemical reactions in porous media were investigated by Veldsink *et al.* [196]. The results showed that the fluxes of reactants predicted from FM are in reasonable agreement with the DGM results, but the mass transport with and without chemical reactions inside a porous slab facing two different gas phases, resembling catalytic membrane reactors, should be described according to DGM. In another research on gas transport in the anode of a solid oxide fuel cell (SOFC) without considering the pressure effect, the accuracies of FM, SMM, and DGM were compared [197]. It was found that SMM is a good approximation of DGM when the pore size is sufficiently large. However, when typical pore size of SOFC anode is used, the error of SMM is significant. For a binary diffusion system, FM can well approximate DGM when the current density is not too large. When treating the ambient air as a binary system ($O_2$ and $N_2$), DGM seems not to be a complicated approach. However, a comprehensive comparison between FM and DGM for the wetted electrode in non-aqueous Li-air batteries is still absent, and further investigation is needed.

In the wetted electrode, an expanded interface between the electrolyte and the air ensures a more uniform distribution of oxygen through the electrode. The oxygen transport resistance through the electrolyte film to the reaction sites, $R_{O_2,e}$, is expressed as a function of the electrolyte film thickness $\delta_e$ and the oxygen diffusion coefficient $D_{O_2,e}$ as

$$R_{O_2,e} = \frac{\delta_e}{D_{O_2,e}} \tag{20}$$

The conservation of oxygen in the air electrode requires that the consumption rate of oxygen by the ORR is equal to the rate of oxygen diffusion through the electrolyte film, which is represented by:

$$\frac{S_{O_2,g}}{a} = R_f \frac{c_{O_2,e} - c_{O_2,g} / H}{R_{O_2,e}} \tag{21}$$

where $a$ and $R_f$ denote the ratio of active surface area per unit electrode volume and a roughness factor of the electrochemically active area per unit geometric area, respectively.

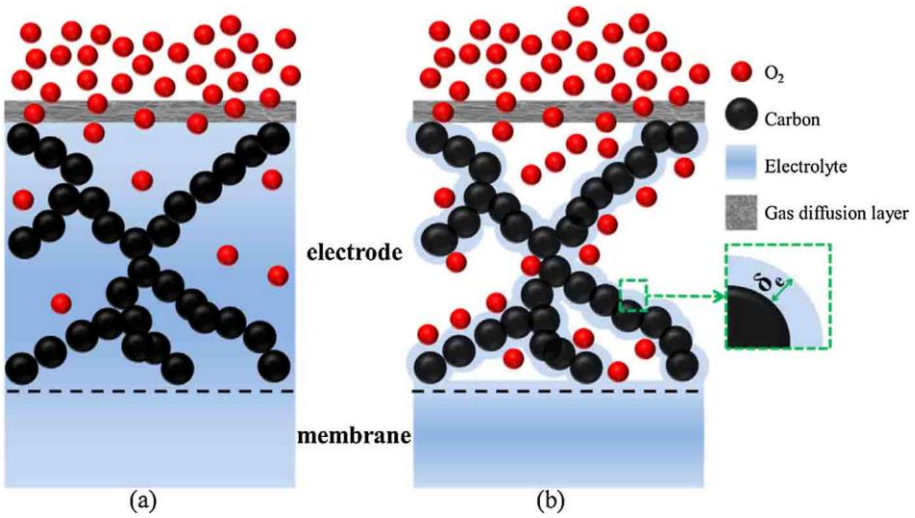


**Fig. 4** Schematic illustration of different degrees of electrolyte filling in an air electrode: (a) flooded electrode and (b) wetted electrode. Reprinted from [187] with permission of Elsevier.

The above-mentioned modeling of oxygen transport considering both scenarios of flooded and wetted electrodes. In a flooded electrode, the consumption of lithium metal and the deposition of the solid product will cause a flow of the electrolyte so that the electrolyte velocity should be considered in Eq. 12. While for a wetted electrode, the deposition of the solid product can cause a change of the electrolyte film thickness, resulting in a moving boundary which should be carefully addressed. In both kinds of

electrodes, the formation of the solid product alters the electrode structure and the corresponding effective diffusion coefficients. Thus, the oxygen transport and the electrochemical reaction are coupled and should be solved simultaneously.

### 3.3 Precipitation of $Li_2O_2$

The formation of solid discharge product $Li_2O_2$ is a unique feature of non-aqueous Li-air batteries, which not only decreases the active surfaces, but also affects the transport kinetics. The formation of solid $Li_2O_2$ is a complicated process with different reaction routes, mechanisms, and morphologies, which are closely linked to the battery performance. Hence, a comprehensive model considering all these aspects is needed.

#### 3.3.1 Formation mechanism

As introduced in Section 2.1, two formation mechanisms of $Li_2O_2$ have been proposed, namely the solution mechanism and surface mechanism, depending on the $LiO_2$ solubility in the electrolyte and the adsorption energy of $LiO_2$ on the electrode surface [75]. A kinetic model has been developed by Nazar *et al.* [198] to describe the detailed ORR process. As schematically shown in **Fig. 5**, an equilibrated process of the adsorption of oxygen on the surface free/active sites (S) is considered as:

$$O_2 + S \leftrightarrow O_2^* \tag{X}$$

where $^*$ denotes the adsorbed state. The fraction of the surface covered by the ad-oxygen ($\theta_{O_2}$) and free sites ($\theta_S$) is:

$$\theta_{O_2} = \frac{k_a c_{O_2}}{k_d} \theta_S = w\theta_S \tag{22}$$

where $c_{O_2}$ is the oxygen concentration in solution adjacent to the electrode surface, $k_a$ and $k_d$ are the adsorption and desorption rate constants, respectively, and $w$ stands for the dimensionless factor of the three constants.

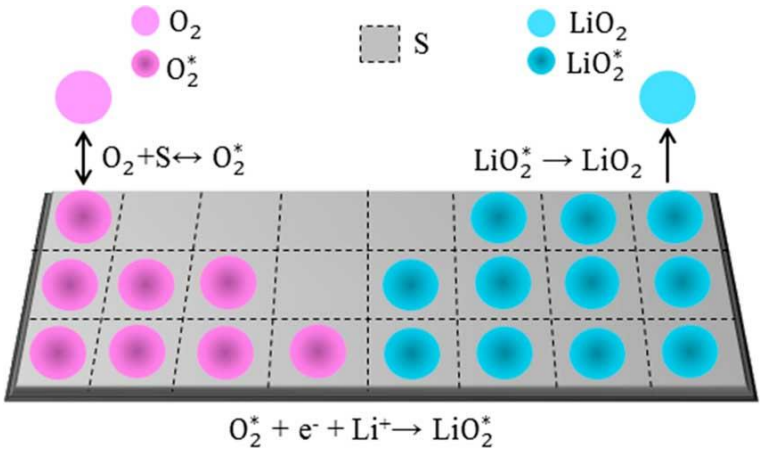


**Fig. 5** Schematic of the main steps accounted for in the kinetic model in the ORR of non-aqueous Li-air batteries. Reprinted from [198] with permission of American Chemical Society.

After the first electrochemical step in ORR to form $LiO_2$, the succeeding predominant pathways are derived either from the chemical disproportionation (Reaction IIIa) or the further electrochemical reduction (Reaction IIIb) to form $Li_2O_2$. When neglecting the backward reactions and in the abundance of $Li^+$, the rate of electrochemical reduction of ad-$O_2$ to ad-$LiO_2$ ($S_1$) (Reaction II) and ad-$LiO_2$ to ad-$Li_2O_2$ ($S_2$) (Reaction IIIb) can be described as

$$-S_1 = \frac{I_1}{FA} = -k_{c1}\Gamma\theta_{O_2}\exp\left(-\frac{\beta_1 F}{RT}\Psi\right) \tag{23a}$$

$$-S_2 = \frac{I_2}{FA} = -k_{c2}\Gamma\theta_{LiO_2}\exp\left(-\frac{\beta_2 F}{RT}\Psi\right) \tag{23b}$$

where ψ is the electrode potential, Γ is the maximum surface-site concentration, $k_{c1}$ and $k_{c2}$ are the rate constants, $\beta_1$ and $\beta_2$ are the charge transfer symmetry factors, and $I_1$ and $I_2$ are the current flows in the reduction of ad-$O_2$ and ad-$LiO_2$, respectively, $A$ is the total active area of the air electrode, $\theta_{LiO_2}$ is fraction of surface covered by the ad-$LiO_2$ with the mass balance:

$$\Gamma \frac{\partial \theta_{LiO_2}}{\partial t} = S_1 - S_2 - S_S \tag{24}$$

where $S_S$ represents the consumption rate of $LiO_2^*$ due to solution-mediated reactions and can be approximated with a first-order dependence on $LiO_2^*$ with rate constant $k_S$ as:

$$S_S = k_S \Gamma \theta_{LiO_2} \tag{25}$$

Upon rearrangement of Eqs 23−25 and under steady-state conditions, the surface overflow of $LiO_2$ to the rate of consumption in the solution-mediated reactions is:

$$\frac{(I_2 - I_1)}{FA} = k_S \Gamma \theta_{LiO_2} \tag{26}$$

Combining with the balance of total current ($I$) and surface-site yields:

$$I = I_1 + I_2 \tag{27}$$

$$\theta_{O_2} + \theta_{LiO_2} + \theta_S = 1 \tag{28}$$

The total current is expressed as a function of potential as:

$$-\frac{I}{FA\Gamma} = k_{c1} w \theta_S \exp\left(-\frac{\beta_1 F}{RT}\Psi\right) + k_{c2}[1-(1+w)\theta_S]\exp\left(-\frac{\beta_2 F}{RT}\Psi\right) \tag{29}$$

The kinetic model considered the influence of both chemical disproportionation and electrochemical reactions during the ORR process. From Eq. 29, with the values of related parameters which are system specific and sensitive largely to the electrode material and electrolyte composition, the potential can be plotted [199]. From this model,

the morphology of the discharge product is strongly dependent on the relative consumption rate of the $LiO_2$ at the surface (film) and the solution (particle) as

$$\frac{\text{particle}}{\text{film}} \propto \frac{S_S}{S_2} = \frac{k_S}{k_{c2}} \exp\left(\frac{\beta_2 F}{RT}\Psi\right) \tag{30}$$

which are related to the desorption of $LiO_2$ ($k_S$) and potential ($\psi$), matching the experimental observations shown in **Fig. 6** [75].

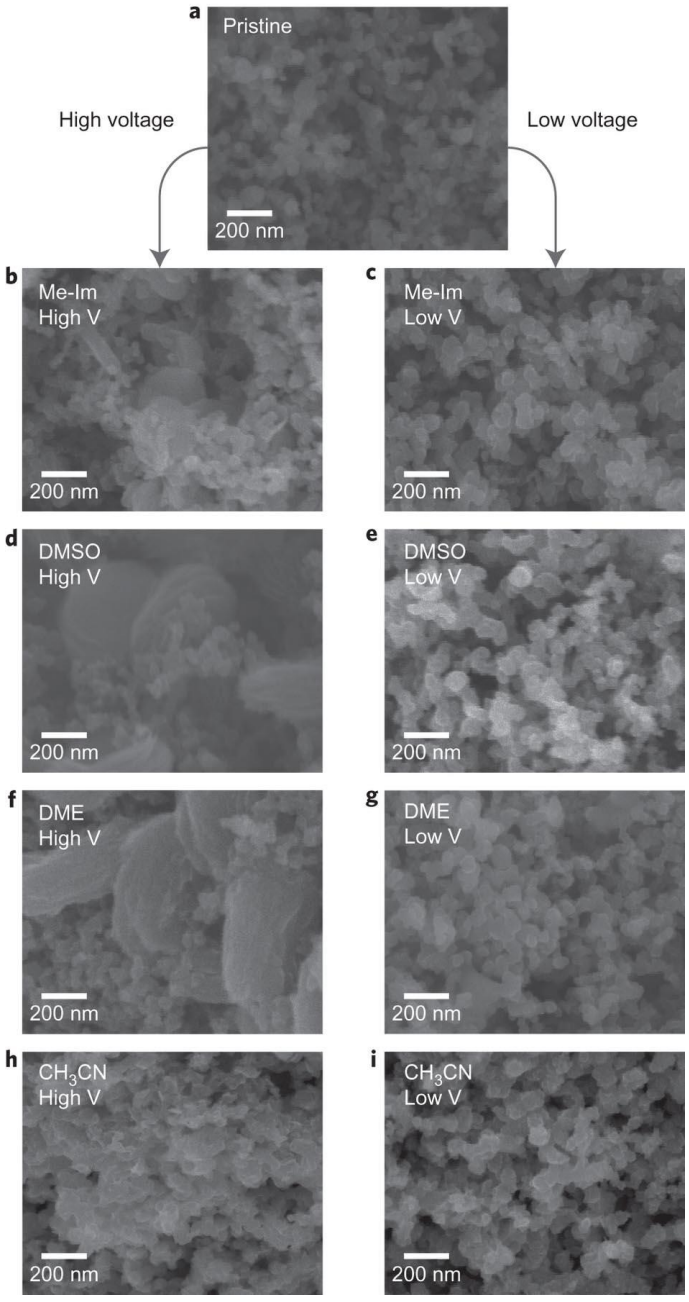

**Fig. 6** Scanning electron microscope (SEM) images showing the $Li_2O_2$ morphologies obtained in different solvents and at potentials: (a) pristine, (b, d, f, h) high, and (c, e, g, i) low potentials. Reprinted from [75] with permission of Nature Publishing Group.

Although Eqs. 22−30 can model the oxygen reduction process, the effects of porous air electrode are not taken into account. To describe the reaction mechanism in the porous electrode, Franco *et al.* defined an escape function $\chi(r)$ which characterizes the percentage of $O_2^-$ in the solvated form to escape the pore of radius $r$ toward the hall where most of the nucleation and growth is assumed to occur [200]. The formed $O_2^-$ in Reaction II could be rewritten as a combination of soluble $O_2^-$ in the electrolyte and adsorption $O_2^{-*}$ on the surface as:

$$O_2^- \rightarrow \chi(r)\, O_2^- + [1 - \chi(r)]\, O_2^{-*} \tag{XI}$$

So the solution mechanism (chemical disproportionation) could be written as:

$$\chi(r)\, O_2^- + \chi(r)\, Li^+ \rightarrow \left[\frac{\chi(r)}{2}\right] Li_2O_{2(particle)} + \left[\frac{\chi(r)}{2}\right] O_2 \tag{XIIa}$$

and the surface mechanism (electrochemical reduction) became:

$$[1 - \chi(r)]\, O_2^{-*} + 2[1 - \chi(r)]\, Li^+ + [1 - \chi(r)]\, e^- \rightarrow [1 - \chi(r)]\, Li_2O_{2(film)} \tag{XIIb}$$

which together with Reaction IV gave:

$$O_2 + 2Li^+ + 2e^- \rightarrow \left[\frac{\chi(r)}{2 - \chi(r)}\right] Li_2O_{2(particle)} + 2\left[\frac{1 - \chi(r)}{2 - \chi(r)}\right] Li_2O_{2(film)} \tag{XIII}$$

Hence, the morphology of $Li_2O_2$ can be discriminated, and the thin film is taken into further analyses since it causes surface passivation and blocks electron transport. The escape function was expressed as:

$$\chi(r) = \xi_{esc}^{\frac{r_{max} - r}{r_{max}}} \tag{31}$$

where $\xi_{esc}$ is the escape probability factor and the value ($0 \leq \xi_{esc} \leq 1$) is assumed to be mainly dependent on the donor number (DN) of the solvent used. At high DN solvents, $\xi_{esc}$ is close to 1, meaning that solution mechanism dominates in the $Li_2O_2$ formation. Thus, the effect of non-aqueous electrolyte on the reaction mechanisms can be described. In addition, the $\xi_{esc}$ value is also highly sensitive to current because the current decides the amount of intermediate species near the surface. At the given electrolyte and current where $\xi_{esc}$ is a fixed value, $\chi(r)$ is a function of pore radius so that the relationship between the product morphology and electrode microstructure can be described.

### 3.3.2 Morphology of $Li_2O_2$ versus current

The above-mentioned modeling works enable the discrimination of formation mechanisms of $Li_2O_2$, and the different morphologies are qualitatively described through Eqs. 30 and 31. While for a given non-aqueous Li-air battery, the product morphology also depends on the operating conditions (e.g., current density, temperature, oxygen pressure) [201-203]. Nazar *et al.* investigated the discharge performance at current densities ranging from 5−100 μA $cm^{-2}$, as shown in **Fig. 7** [204]. The discharge overpotential increases with the current density, and the overall capacity decreases. The significant differences in capacity are correlated to a distinct change in the surface structure: Low current densities in the range of 5−25 μA $cm^{-2}$ give rise to large toroidal morphologies of $Li_2O_2$ (**Figs. 7b−7d**), whereas the highest current densities of 50 and 100 μA $cm^{-2}$ give deposition products on the carbon that are scarcely visible (**Figs. 7e and 7f**), forming the film-like $Li_2O_2$. The results demonstrate that the current density dramatically affects the product morphology in a very systematic way. Generally, a low current density results in a high potential and particle-like product, whereas a high current

density leads to a low potential and film-like product [201]. To accurately model the battery behaviors under different current densities, a clear description of the corresponding $Li_2O_2$ morphology is essential.

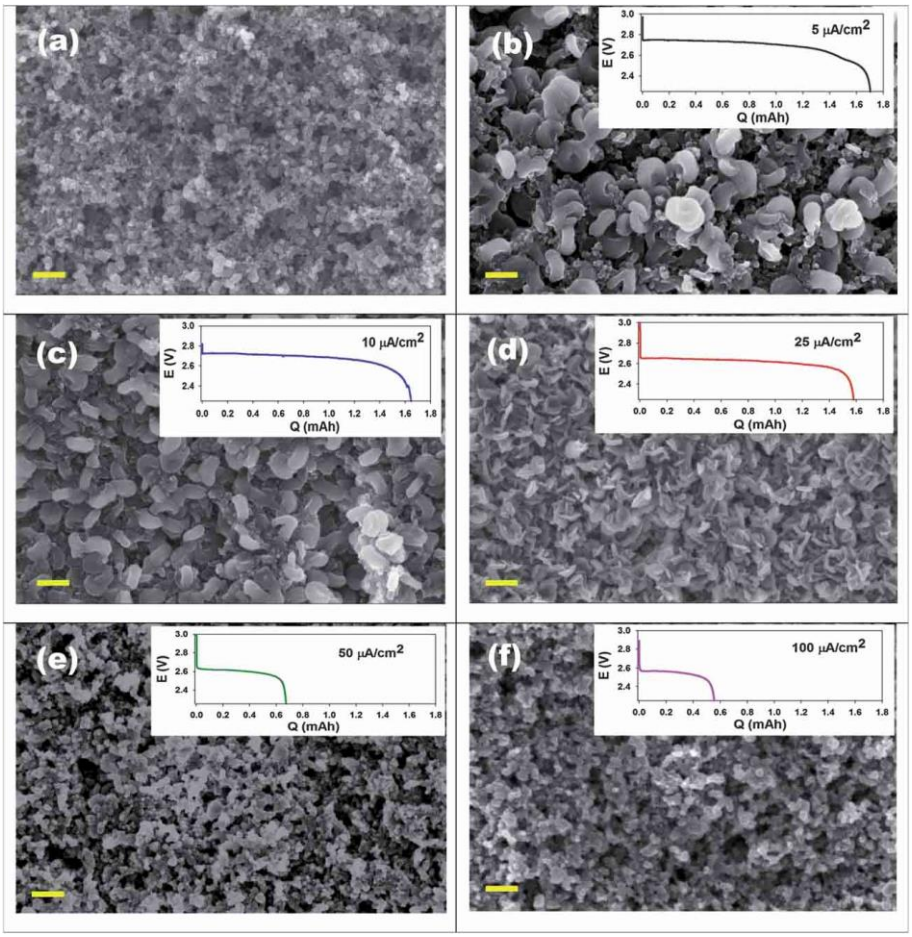


**Fig. 7** Field emission scanning electron microscope (FESEM) images at a magnification of 20,000× of (a) the pristine cathode and after full discharge at (b) 5 μA $cm^{-2}$, (c) 10 μA $cm^{-2}$, (d) 25 μA $cm^{-2}$, (e) 50 μA $cm^{-2}$, and (f) 100 μA $cm^{-2}$, with the corresponding discharge curves. Scale bar = 400 nm. Reprinted from [204] with permission of The Royal Society of Chemistry.

Horstmann *et al.* developed a nanoscale continuum model for the initial stages of $Li_2O_2$ growth based on a theory of electrochemical nonequilibrium thermodynamics, as

schematically shown in **Fig. 8a** [205]. The ORR process (Reaction IV) on a carbon surface is modeled in (1 + 1)-dimensional space through the height of the $Li_2O_2$ crystal *h* as a function of the surface coordinate *x*. In this way, $Li_2O_2$ molecules align in columns growing at the electrochemically controlled rate $\partial h/\partial t$. The potential of $Li_2O_2$ was expressed as:

$$\mu_{Li_2O_2} = \frac{\delta G[c_{Li_2O_2}]}{\delta c_{Li_2O_2}} = d_{\parallel} d_{\perp} \frac{\delta G[h]}{\delta h} \tag{32}$$

which is the variational derivative of the Gibbs free energy *G*, $c_{Li_2O_2}$ is the concentration of $Li_2O_2$ molecules per substrate length, $d_{\parallel}$ and $d_{\perp}$ are the distances between molecules in the horizontal and vertical direction, respectively. At a reference state, $\mu^{\Theta}_{Li_2O_2}$, without any $Li_2O_2$ at room temperature and atmospheric pressure ($h$ = 0, 298.15 K, 1 atm), the voltage increment, $\Delta E$, in equilibrium is given by the Nernst equation as:

$$\Delta E_{eq} = -\frac{k_B T}{2e} \ln a_{Li_2O_2} = \frac{\mu^{\Theta}_{Li_2O_2} - \mu_{Li_2O_2}}{2e} \tag{33}$$

where $k_B$ is the Boltzmann constant ($1.38\times10^{-23}$ J $K^{-1}$), *e* is the electron charge, $a_{Li_2O_2}$ is the activity of $Li_2O_2$. Out of equilibrium, the relationship between the activation overpotential ($\eta$) and the two-dimensional current density per substrate area $I_{2D}$ could be obtained by the Butler−Volmer equation as:

$$I_{2D} = \frac{I_0}{\sqrt{1+\left(\frac{\partial h}{\partial x}\right)^2}} \left\{ \exp\left( \frac{-\alpha 2e\eta}{k_B T} \right) - \exp\left[ \frac{(1-\alpha)2e\eta}{k_B T} \right] \right\} \tag{34}$$

where $I_0$ is the exchange current density:

$$I_0 = \frac{2ek_0 a_{Li_2O_2}^{\alpha_{ch}}}{\gamma_{\ddagger}} \tag{35}$$

in which $k_0$ is the rate constant and is determined by Tafel analysis, $\alpha_{ch}$ is the charge transfer coefficient, and $\gamma_{\ddagger}$ is the activity coefficient of the transition state. For galvanostatic discharge, Eq. 34 is solved subject to the constraint of constant mean current density ($\tilde{I}$) in the substrate length ($L_s$) as:

$$\tilde{I} = \frac{1}{L_s}\int_0^{L_s} I_{2D} / 2ek_0 dx \tag{36}$$

The modeling results are shown in **Fig. 8b**. At a very low surface specific discharge rate (2 nA cm$^{-2}$), distinct disc-like particles nucleate and evolve into toroid-like ones. At an intermediate rate (50 nA cm$^{-2}$), small particles are coated on the surface. At a very large rate (400 nA cm$^{-2}$), a film is presented.

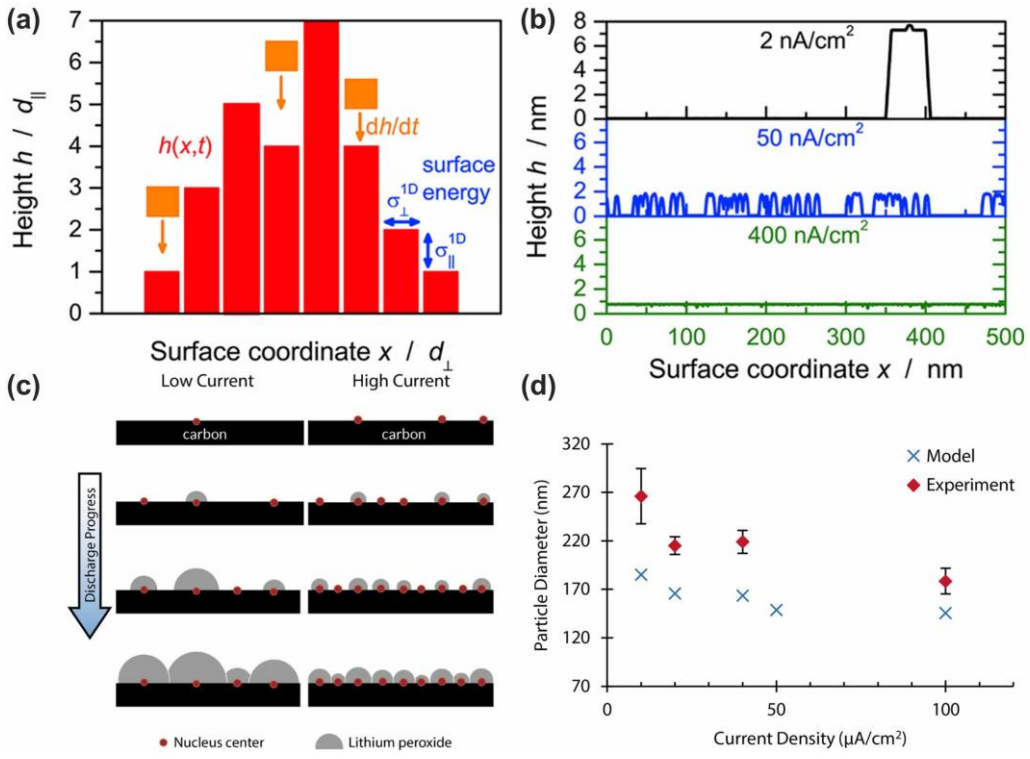

**Fig. 8** Scheme and result of the models in the relationship between $Li_2O_2$ morphology and current density: (a) (1 + 1)-D surface model in which individual $Li_2O_2$ molecules are added on top of a surface crystal of height $h(x,t)$ at the rate $\partial h/\partial t$ and (b) height profile in during discharge to two molecular monolayers. Adapted from [205] with permission of American Chemical Society. (c) nucleation and growth model showing the effect of current density on nucleation rate and the final amount of $Li_2O_2$ deposited and (d) comparison of experimentally observed dominant particle sizes to those predicted by the model. Adapted from [206] with permission of American Chemical Society.

This model well predicts the experimental observations in the initial discharge stage. However, how $Li_2O_2$ nucleation and growth affect the shape of the discharge curve or the final discharge capacity has not been considered. To this end, Archer *et al.* took the $Li_2O_2$ nucleates and grows as discrete nanosized particles (**Fig. 8c**) and analyzed the effect of the current density [206]. First, because the high electrical resistivity of $Li_2O_2$, the current through the $Li_2O_2$-covered portion may be considered negligible compared to the uncovered part. The overpotential could be written using a modified Tafel equation

$$\eta = \frac{k_B T}{e\alpha_O} \ln\left( \frac{i}{i_0} \cdot \frac{1}{1-\theta_{Li_2O_2}} \right) \tag{37}$$

where $\theta_{Li_2O_2}$ is the fraction of the cathode surface covered by $Li_2O_2$ and increases to 1 upon approaching complete coverage, $i$ is the current density, $i_0$ is the exchange current density. Thus, through the model for the nucleation and growth of $Li_2O_2$, the coverage could be determined as a function of time to obtain the discharge curve.

The atomistic theory of electrolytic nucleation was adapted to model the $Li_2O_2$ nucleation kinetics [207]. Solid $Li_2O_2$ is regarded to form through the disproportionation route (Reaction IIIa) with the nucleation rate:

$$J = J_0 \exp\left(\frac{2\alpha_{ch}^{'} e\eta_0}{k_B T}\right)\exp\left(\frac{\alpha_{ch} e\eta}{k_B T}\right)\left(1-\theta_{Li_2O_2}\right) \tag{38}$$

where the first exponential term represents the effect of overpotential on the formation rate of the two $LiO_2$ molecules. $\alpha_{ch}^{'}$ is the charge transfer coefficient of the superoxide formation step, and $\eta_0$ is the effective overpotential for this step. The second exponential represents the effect of overpotential on the rate of adsorption. $J_0$ is the background rate of attachment and is given by:

$$J_0 = K_{+0} c_{O_2} N_0 \exp\left(-\frac{U_0}{k_B T}\right) \tag{39}$$

where $K_{+0}$ is a frequency factor, $N_0$ is the surface concentration of active sites, and $U_0$ is the energy barrier to attachment.

During galvanostatic discharge, the $O_2^-$ concentration reaches a steady state so that the growth rate can be modeled by a constant flux of $Li_2O_2$ at the electrolyte-facing surfaces. For simplicity, the particle shape is taken to be hemispherical and all particles are assumed to grow at the same radial growth rate, which scales with $1/r_{Li_2O_2}^2$ for a fixed amount of $Li_2O_2$ precipitate, where $r_{Li_2O_2}$ is the $Li_2O_2$ particle radius. Under these assumptions, the $Li_2O_2$ growth rate can be derived from a simple conservation of current for a set of non-overlapping particles. As the coverage increases, the growth fronts begin to overlap, which is described as:

$$\frac{dV_{ex}}{dt} = \frac{1}{1 - V / V_{max}} \cdot \frac{dV}{dt} \tag{40}$$

where $V_{ex}$ is the extended volume, $V_{max}$ is the maximum volume defined by the system boundaries, and $V$ is the real volume. Since the maximum volume is confined by the surface area of the cathode, the volume fraction $V/V_{max}$ can be approximated by the surface coverage $\theta_{Li_2O_2}$. The real volumetric growth rate is simply derived from the conservation of current and thus the equation for the radial growth rate was obtained as:

$$\frac{dr_{Li_2O_2}}{dt} = \frac{1}{1 - \theta_{Li_2O_2}} \cdot \frac{i}{2F} \cdot \frac{M_{Li_2O_2}}{\rho_{Li_2O_2}} \cdot \frac{1}{2\pi \sum_j n_j r_{Li_2O_2,j}^2} \tag{41}$$

where $M_{Li_2O_2}$ and $\rho_{Li_2O_2}$ are the molecular weight and density of $Li_2O_2$, respectively, $r_{Li_2O_2,j}$ is a particular radius, and $n_j$ is the number of particles with that radius. Base on the hemispherical-particle assumption, the coverage was expressed as:

$$\theta_{Li_2O_2} = 1 - \exp\left( -\frac{\pi}{A} \cdot \sum_j n_j r_{Li_2O_2,j}^2 \right) \tag{42}$$

With this model, $Li_2O_2$ particle sizes at different current densities can be estimated. When compared with those observed experimentally, as shown in **Fig. 8d**, the predicted size is in good agreement with the experiments. Moreover, the particle size distribution can be simulated with this model at a low current density, and it is found that the sharp voltage drop at the end of discharge is caused by an increased kinetic overpotential due to the coverage of $Li_2O_2$ on the active surfaces.

### 3.3.3 Transport through $Li_2O_2$

In addition to describing the reaction mechanism and product morphology, understanding the transport process through the solid $Li_2O_2$ is important for analyzing the

limiting factor. Three different transport mechanisms have been proposed, as schematically shown in **Fig. 9** [208].

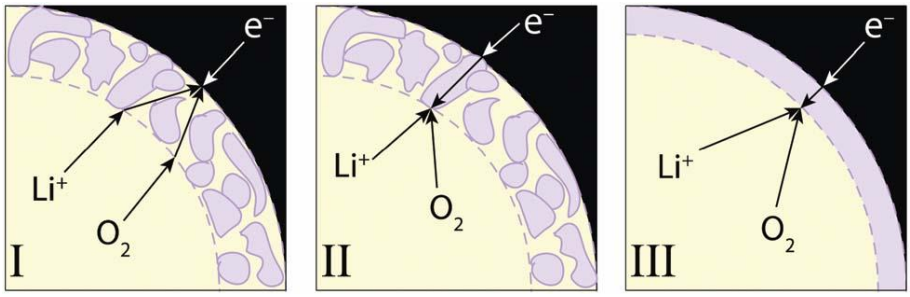


**Fig. 9** Schematic diagrams of discharge reaction mechanisms among three phases: liquid electrolyte (yellow), solid backbone (black), and discharge product layer (bounded by the solid backbone and the dashed line). Reprinted from [208] with permission of The Royal Society of Chemistry.

The first mechanism (I) is that $Li_2O_2$ growth is controlled by electron exchange at the discharge-product/solid interface. In this case, the $Li_2O_2$ layer is not compact and can be permeated by the liquid electrolyte. Current exchanged between the liquid phase and the solid backbone is carried by ion transport through the liquid electrolyte within the product layer, and the electron exchange occurs at the solid surface. Since the electron-transfer site is on the solid surface, the area associated with electron exchange keeps constant as discharge progresses. As no electron transfer through the $Li_2O_2$ layer, the voltage loss due to the electronic resistance ($\Delta\phi_{Li_2O_2}$) is set as zero.

From Jung's work, the thickness of the porous deposit layer, $\delta_{Li_2O_2,por}$, is estimated as [171]:

$$\delta_{Li_2O_2,por} = \left( \sqrt[3]{\frac{\varepsilon_{layer}}{(1-\varepsilon)}} + 1 \right) r \tag{43}$$

where $\varepsilon_{\text{layer}}$ is the volume fraction of the $Li_2O_2$ deposit layer and is defined as:

$$\varepsilon_{\text{layer}} = \frac{\varepsilon_{\text{p}}}{\theta_{\text{Li}_2\text{O}_2}} \tag{44}$$

The transport of $Li^+$ and $O_2$ can be analyzed using the Fick's law, and thus the species molar concentration at the backbone surface becomes:

$$c_{i,\text{int}} = c_i + \frac{\delta_{\text{Li}_2\text{O}_2,\text{por}} j_{\text{c}}}{D^{\text{eff}}_{i,\text{Li}_2\text{O}_2} \cdot nF} \tag{45}$$

where $c_i$ is the molar concentration of species $Li^+$ and $O_2$, $j_{\text{c}}$ is local transfer current density between electrode and electrolyte interface. The effective diffusion coefficient of species $i$, $D^{\text{eff}}_{i,\text{Li}_2\text{O}_2}$, is estimated by:

$$D^{\text{eff}}_{i,\text{Li}_2\text{O}_2} = (1-\theta_{\text{Li}_2\text{O}_2})^{\alpha} D_i \tag{46}$$

The second mechanism (II) is that $Li_2O_2$ growth is controlled by electron exchange at the electrolyte/discharge-product-layer interface. In this case, the $Li_2O_2$ layer is not compact but electron propagation across it supports electrochemical formation at sites displaced from the native porous-electrode surface. Hence, the transport of species in the porous $Li_2O_2$ layer is no need to be considered (Eq. 45) but the electronic resistance should be considered as [171]:

$$\Delta\phi_{\text{Li}_2\text{O}_2} = \frac{j_{\text{c}} \delta^2_{\text{Li}_2\text{O}_2,\text{por}}}{\int \kappa^{\text{eff}} dt_{\text{Li}_2\text{O}_2}} \tag{47}$$

The third mechanism (III) is that $Li_2O_2$ growth is controlled by electron transfer through a compact product film, which is also widely applied in modeling works [38]. This case is similar to the second mechanism, in which the electronic resistance must be

considered. Based on the specific cathode microstructure [209,210], different formulas for $\Delta\phi_{Li_2O_2}$ have been given [38], while the key is established according to Ohm's law as:

$$\Delta\phi_{Li_2O_2} = j_c\delta_{Li_2O_2} / \sigma_{Li_2O_2} \quad (48)$$

where $\sigma_{Li_2O_2}$ is the electrical conductivity of $Li_2O_2$, which is very low (~ $10^{-19}$ S $cm^{-1}$) [211], $\delta_{Li_2O_2}$ is the thickness of the compact $Li_2O_2$ film. In addition to using a constant resistance, it is also suggested that the conductivity of the $Li_2O_2$ thin film decreases with an increase in the thickness [70], resulting in a fitted power law as [212]:

$$\sigma_{Li_2O_2} = 10^7 \cdot \delta_{Li_2O_2}^{-17.18} \ (S \cdot m^{-1}) \quad (49)$$

Due to the extremely high electrical resistance, it is suggested that the charge transport through $Li_2O_2$ at practical current densities is based principally on hole tunneling [213], and the tunneling current through the film can no longer support the electrochemical current when the thickness of $Li_2O_2$ film reaches ~5 to 10 nm [70]. Based on this, Franco *et al.* considered the resistance of transport through $Li_2O_2$ as a decrease of the available surface area ($a_{ava}$) instead of voltage loss as [214]:

$$a_{ava} = \left[\frac{1-\mathrm{erf}(\delta_{Li_2O_2}-7)}{2}\right] a \quad (50)$$

which means that for those surface areas covered by $Li_2O_2$ thinner than the tunneling range, the resistance is approximately as zero, otherwise the surface areas will be regarded as inactive.

The above-mentioned three mechanisms are based on either porous $Li_2O_2$ layer or compact $Li_2O_2$ film with electron tunneling as the main transport mechanism. Siegel *et al.* proposed a new continuum transport model to explore an alternative scenario, in which

the charge transport is mediated by polaron hopping [215]. They defined the dimensionless current ( $j_{\mathrm{d}}$ ) and dimensionless $Li_2O_2$ layer thickness ( $\delta^{\mathrm{d}}_{Li_2O_2}$ ) as:

$$j_{\mathrm{d}} = \frac{2i\delta_{Li_2O_2}}{FD_{\mathrm{pol}}(c_0 + c_{\mathrm{t}})} \tag{51}$$

$$\delta^{\mathrm{d}}_{Li_2O_2} = \left[\frac{F^2\delta^2_{Li_2O_2}(c_0 + c_{\mathrm{t}})}{2\varepsilon_{\mathrm{pd}}RT}\right]^{1/2} \tag{52}$$

where $D_{\mathrm{pol}}$ is the polaron diffusivity, $\varepsilon_{\mathrm{dp}}$ is the dielectric permittivity, $c_0$ and $c_{\mathrm{t}}$ is the polaron concentration at the layer/electrolyte and layer/electrode interface, respectively. If the dimensionless layer thickness is large, the overpotential is:

$$\Delta\phi_{Li_2O_2} = -\frac{1}{4\pi^2}\frac{i\delta^3_{Li_2O_2}}{D_{\mathrm{pol}}\varepsilon_{\mathrm{dp}}} \tag{53}$$

from which the overpotential is independent of the boundary concentrations, but increases with the cube of the $Li_2O_2$ layer thickness and decreases with increasing temperature. If the dimensionless layer thickness is small, the overpotential associated with charge-transport limitations becomes Ohmic if the current is large or small:

$$-\frac{F^2D_{\mathrm{pol}}\Delta\phi_{Li_2O_2}}{i\delta_{Li_2O_2}RT} = \begin{cases} 1/c_{\mathrm{t}} & \text{when } j_{\mathrm{d}} \ll -1 \\ (1/c_0 - 1/c_{\mathrm{t}})\ln(c_0/c_{\mathrm{t}}) & \text{when } |j_{\mathrm{d}}| \ll 1 \\ 1/c_0 & \text{when } j_{\mathrm{d}} \gg 1 \end{cases} \tag{54}$$

Unlike the thick-layer or low-current regime, the overpotential in the thin-layer limit is asymmetric when the polaron concentrations at the layer/electrolyte and layer/electrode interfaces are different.

### 3.4 Discharge reaction kinetics

For the electrochemical reaction at the lithium anode, as expressed in Reaction I, the local transfer current density between anode and electrolyte interface ( $j_a$ ) can be given by the general Bulter-Volmer equation as:

$$j_a = i_{a0}\left\{\exp\left[\frac{(1-\beta)nF}{RT}\eta_a\right]-\exp\left(\frac{-\beta nF}{RT}\eta_a\right)\right\} \tag{55}$$

where $i_{a0}$ is the exchange current density at the anode, and $\beta$ is the symmetry factor, $\eta_a$ is surface or activation overpotential for reaction at the anode.

For the electrochemical reaction at the cathode electrode, different formations of $j_c$ have been applied [37], while the generally used one is using two rate coefficients which depend on both concentration of $Li^+$ and $O_2$ and concentration of $Li_2O_2$ (Reaction IV):

$$\frac{j_c}{nF} = k_a(c_{Li_2O_2,s})\exp\left[\frac{(1-\beta)nF}{RT}\eta_c\right]-k_c(c_{Li^+,s})^2(c_{O_2,s})\exp\left(\frac{-\beta nF}{RT}\eta_c\right) \tag{56}$$

where $c_{i,s}$ is the molar concentration of species $i$ at the wall or surface of the electrode, $k_a$ and $k_c$ are the anodic and cathodic rate constant, respectively. $\eta_c$ is surface or activation overpotential for reaction at the cathode and is given by:

$$\eta_c = \phi_s - \phi_l - \Delta\phi_{Li_2O_2} - E^0 \tag{57}$$

in which the voltage loss through the $Li_2O_2$ layer ( $\Delta\phi_{Li_2O_2}$ ) is according to the assumed mechanism as introduced in Section 3.3.3.

The electrochemical reaction coupling with species and charge transport gives:

$$\nabla\cdot\boldsymbol{i}_l = aj \tag{58}$$

$$S_i = -\frac{as_i}{nF}j_c \tag{59}$$

where $S_i$ is the source term of species *i* ($Li^+$, $O_2$) in the electrolyte as expressed in Eq. 1 and 11, $s_i$ is the corresponding stoichiometric coefficient. Hence, the reaction kinetics is coupled with transport processes and also changes with time during the whole discharge region. Wang *et al.* assumed the exchange current density to be uniformly distributed across the cathode and neglected the transient term, through which they presented an analytical expression of the total voltage loss with the Damköhler number (Da) [216-218]. As the discharge process in non-aqueous Li-air batteries accompanies with the solid product deposition, which changes the species transport, reaction kinetics, and surface areas, detailed analyses of the transient behavior is still needed.

### 3.5 Electrode structure evolution

The solid $Li_2O_2$ precipitates in the porous air electrode during discharge, covering the surface and occupying the void volume. From Reaction IV, the volume change due to the accumulation of solid $Li_2O_2$ can be easily obtained as:

$$\frac{\partial \varepsilon_{\mathrm{p}}}{\partial t} = a j_{\mathrm{c}} \frac{M_{\mathrm{Li_2O_2}}}{2F\rho_{\mathrm{Li_2O_2}}} \tag{60}$$

However, the change of surface area is more complicated which is related to the pore size, pore shape, as well as product morphology, and should be carefully treated.

#### 3.5.1 Continuum models

In macroscopic continuum models, the effective local surface area per unit volume of the air electrode due to $Li_2O_2$ coverage is commonly written by a geometric relation as [38]:

$$\frac{a}{a^0} = 1 - \left( \frac{\varepsilon_{\mathrm{p}}}{\varepsilon} \right)^p \tag{61}$$

where $a^0$ is the initial specific surface area, $p$ is a geometrical factor indicating the morphology shape of the solid product that covers the active area. Small values of $p$ indicate that the flat, plate-like precipitate of $Li_2O_2$, whereas large values of $p$ reflects the needle-like solid product. As the $Li_2O_2$ morphology is related to the current density, an expression of $p$ was given by Jung *et al.* as [171]:

$$p = \frac{C_{\text{emp}}}{i_{\text{m,app}}} \tag{62}$$

where $C_{\text{emp}}$ is the empirical constant which is mainly affected by electrode materials and electrolytes, $i_{\text{m,app}}$ is the mass-specific current density. Hence, a large current will lead to a small value of $p$, corresponding to a plate-like morphology as experimental observations [204].

Usually, the solid $Li_2O_2$ is treated as a compact film covering the air electrode surface. As the pore structures in the air electrode are different due to various electrode materials as schematically shown in **Fig. 10** [210], the specific surface area changes from the macroscopic view are expressed as:

$$\frac{a}{a^0} = \begin{cases} \left(1-\varepsilon_{\text{p}}/\varepsilon\right)^{1/2} & \text{cylindrical pore} \\ \left(1-\varepsilon_{\text{p}}/\varepsilon\right)^{2/3} & \text{spherical pore} \\ \left[1+\varepsilon_{\text{p}}/(1-\varepsilon)\right]^{1/2} & \text{cylindrical nanoparticle} \\ \left[1+\varepsilon_{\text{p}}/(1-\varepsilon)\right]^{2/3} & \text{spherical nanoparticle} \end{cases} \tag{63}$$

Although Eq. 63 describes the specific surface area changes for different pore structures, it is worth noting that the actual pore structure may evolve during the discharge process. For instance, for the electrode made of cylindrical nanoparticles (e.g., nanotubes and nanofibers, **Fig. 10c**), the effective radius is continuously increasing

because of the deposition of the $Li_2O_2$, resulting in an increase in specific surface area. However, when the deposit layer growth on one fiber congregates with the growth on adjacent fibers, the structure changes to the cylindrical pores (**Fig. 10a**). Hence, a hybrid model that can correctly capture the structure change is needed [210].

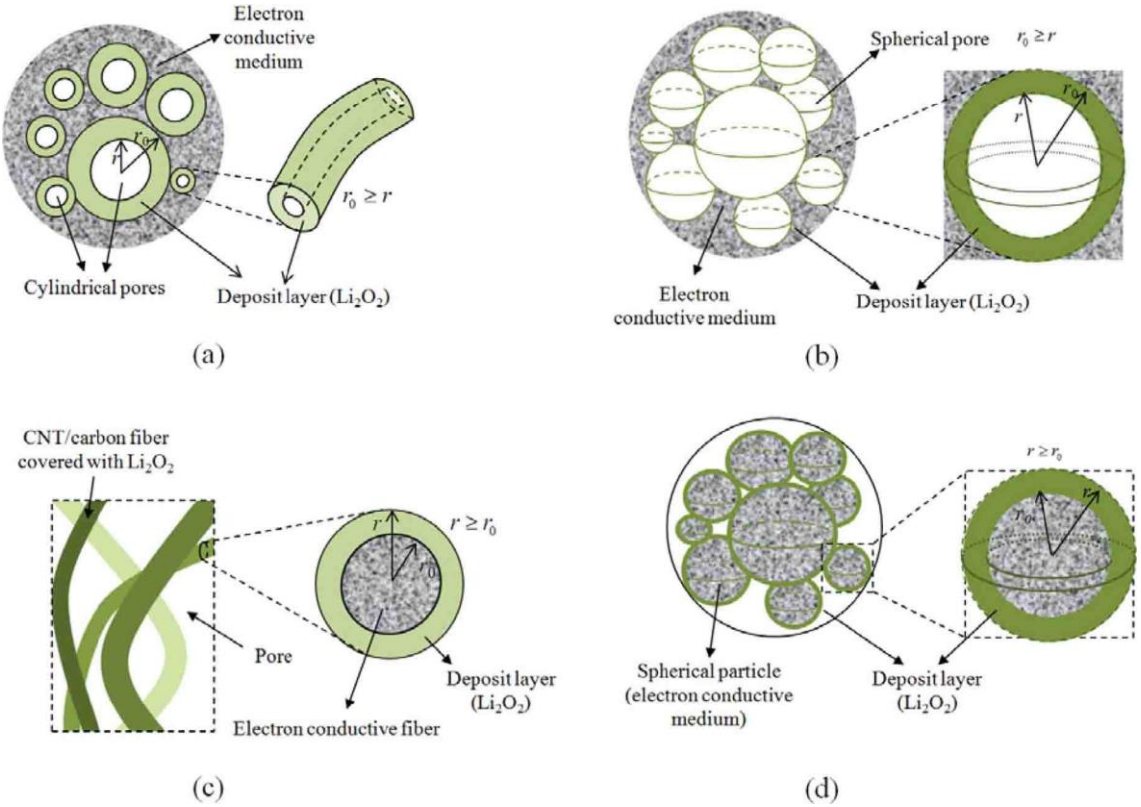


**Fig. 10** Deposition of the discharge product for the four structures: (a) cylindrical pores, (b) spherical pores, (c) cylindrical nanoparticles, and (d) spherical nanoparticles. Reprinted from [210] with permission of The Electrochemical Society.

In continuum models, the porous air electrode is usually characterized by porosity, specific surface area, and average pore radius, and some important guidance can be obtained for performance improvements. For instance, from the modeling investigation, Li and Faghri found that the $Li_2O_2$ volume fraction gradually decreases from the air side toward the separator side due to the concentration gradient of oxygen [27]. Based on this

result, they proposed that a cathode structure with a gradient porosity which is higher closer to the air side and lower at the separator side can improve the discharge capacity. This concept was proven to be effective through experiments [21]. Although the geometrical changes can be captured through Eq. 63, for a practical electrode with various kinds of pores, directly using these parameters may result in inaccurate results. Tonti *et al.* prepared four kinds of porous carbons with the similar specific surface areas and total pore volumes, namely C233 (596 $m^2\ g^{-1}$, 1.50 $cm^3\ g^{-1}$), C235 (638 $m^2\ g^{-1}$, 1.20 $cm^3\ g^{-1}$), C250 (603 $m^2\ g^{-1}$, 0.85 $cm^3\ g^{-1}$), and C237 (641 $m^2\ g^{-1}$, 0.55 $cm^3\ g^{-1}$), but with different pore size distribution (PSD), as shown in **Figs. 11a** and **11b** [219]. When tested in a battery with an ionic liquid-based electrolyte, they delivered different discharge capacities (**Figs. 11** and **11d**). In particular, C250 with the pore radius of 22 nm showed the largest specific capacity, in agreement with the literature that mesopores are the most effectively used by the discharge product [220]. This result indicated that the capacity could not be established through a simple correlation between the specific surface area or total pore volumes. As schematically shown in **Fig. 12**, when the surface area is mainly contributed from micropores, a lot of available surface area will be lost if these pores are clogged by the solid product (shaded area); but this phenomenon cannot be described using the average pore radius. Therefore, the pore structure of the carbon materials has a significant influence on the discharge capacity. To more precisely capture the surface area change during the discharge process, considering the PSD is needed [210,214,221-223].

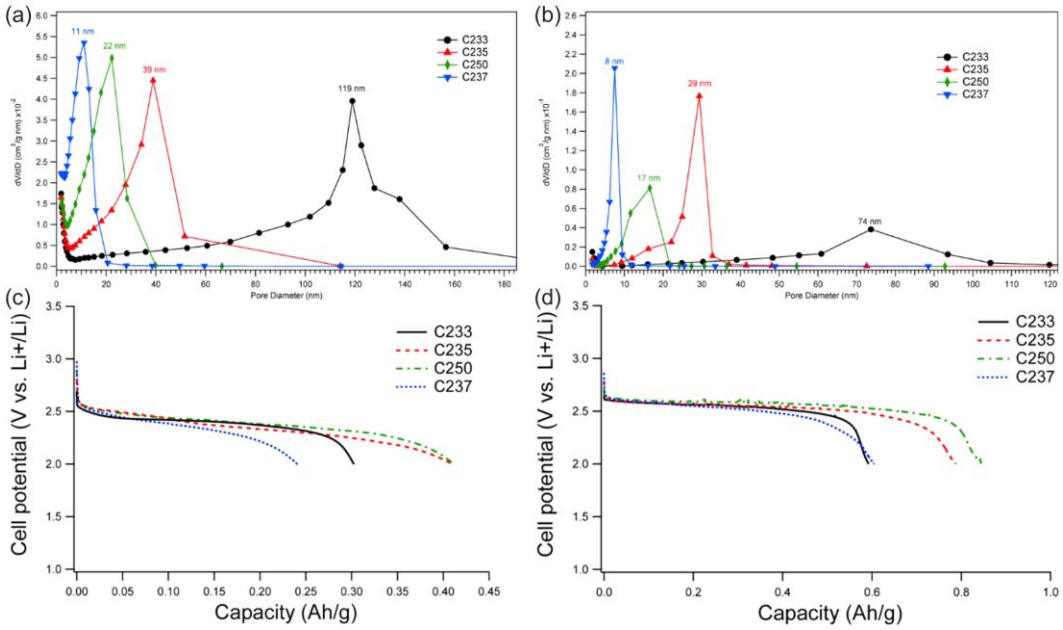


**Fig. 11** (a-b) Pore distribution of four carbons from $N_2$ (a) adsorption and (b) desorption branch using Barrett-Joyner-Halenda (BJH) method. (c-d) Corresponding discharge capacities of four carbons at (c) room temperature and (d) 60 $^{o}$C. Adapted from [219] with permission of American Chemical Society.

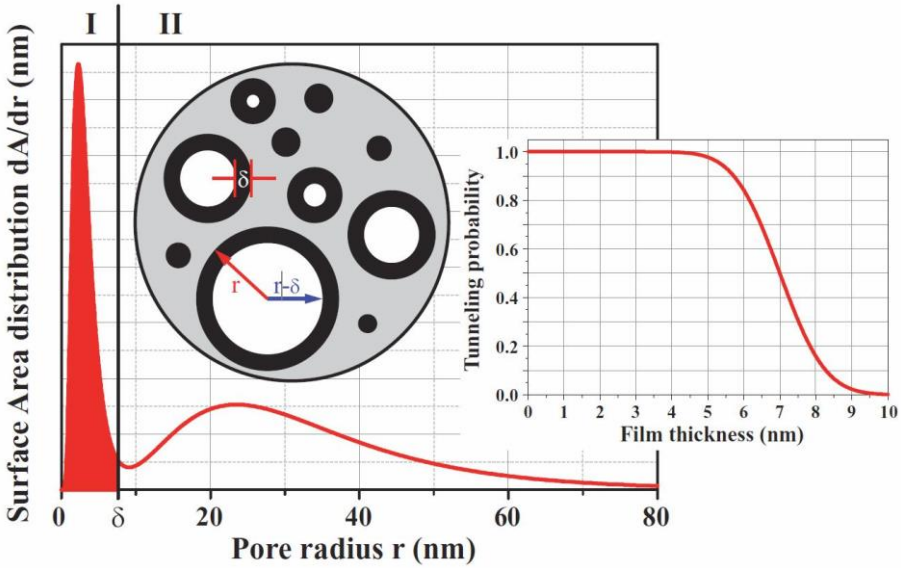


**Fig. 12** A typical surface area distribution function. Round inset: the clogged pores as well as unclogged pores with surface area modification by the finite thin film thickness

$\delta_{Li_2O_2}$ . Right inset: the electron tunneling probability function versus $Li_2O_2$ layer thickness (Eq. 50). Reprinted from [214] with permission of The Electrochemical Society.

Assuming the air electrode is composed of spherical pores, the relationship between the surface area and pore radius is expressed as [214]:

$$\frac{da}{dr} = 4\pi(r - \delta_{Li_2O_2})^2 \frac{dN_p}{dr} = \left[\frac{3(r - \delta_{Li_2O_2})^2}{r^3}\right]\frac{d\overline{V}}{dr} \tag{64}$$

where $dN_p/dr$ is the number density distribution of pore sizes. The PSD of some carbon blacks can be mathematically described by a bimodal log-normal distribution function as:

$$\frac{d\overline{V}}{dr} = \frac{1}{\sqrt{\pi}(\ln s_1 + \zeta \ln s_2)r}\left\{\exp\left[-\left(\frac{\ln(r/r_1)}{\ln s_1}\right)^2\right] + \zeta \exp\left[-\left(\frac{\ln(r/r_2)}{\ln s_2}\right)^2\right]\right\} \tag{65}$$

where $r_1$ and $r_2$ indicate the peak positions of primary and secondary pores, respectively; $s_1$ and $s_2$ control peak widths; $\zeta$ represents the volume ratio of secondary to primary pores. The thickness of the compact $Li_2O_2$ layer is correlated to the reaction as:

$$\frac{\partial \delta_{Li_2O_2}}{\partial t} = j_c \frac{M_{Li_2O_2}}{2F\rho_{Li_2O_2}} \tag{66}$$

Different from Eqs. 61−63 in which the available surface area depends on the electrode porosity, Eqs. 64−66 show that the surface area relies on the pore size distribution, and to consider the resistance caused by the compact $Li_2O_2$ film, Eq. 50 should also be combined to describe the electron tunneling effect.

### 3.5.2 Other methods

The continuum approach can give good results of the electrode structure changes from the macroscopic view. However, it may reach its limit when the investigation scales down to the meso-level where the collision frequency of species with boundaries (e.g.,

pores, channel walls) is comparable with the intermolecular collision frequency. Besides, continuum models use representation geometrical parameters of the electrode (e.g., porosity, pore volume), while in reality pores can have different shapes and coordination (number of interconnections with the neighbors). Such a simplification may lead to misinterpretation of experimental data and inaccurate modeling results. Therefore, to detailedly describe the electrode microstructure, other modeling approaches are required.

A three-dimensional (3D) Kinetic Monte Carlo (KMC) model was developed to describe the coupled transport and reaction processes inside a pore as a representative of a porous air electrode, as shown in **Fig. 13** [224]. The geometry of the modeled pore is assumed to be a spherical cavity with two cylindrical channels linking with the sources of $O_2$ and $Li^+$, respectively. The radius of the pore, channel, and the channel length are within the range of 5 to 15 nm. Cubic meshes are used to build the 3D grid network with the mesh size of 5 Å, which is similar to the size of solvated $Li^+$ in DMSO. Four species that get involved in the electrochemical or chemical reactions ($Li^+$, $O_2$, $LiO_2$, and $Li_2O_2$) are considered, in which each $Li^+$ or $O_2$ occupies one grid unit, each $LiO_2$ occupies two adjacent grid units, and each $Li_2O_2$ occupies three grid units (**Fig. 13d**). The impact of the electrolyte on the particles motion and reactions is captured implicitly by the related kinetic and diffusion parameters. Through this method, the impacts of geometric parameters, i.e., pore radius and channel radius, were investigated considering four systems with a pore radius of 10 or 15 nm combining channels with a radius of 7.5 or 5 nm. Results showed that the enlarged channel is preferred, as the benefit from the growth of $O_2$ population counteracted and even overwhelmed the loss from the decrease of

collision frequency. In addition, the pore size has an effect on the reaction rate, especially after the passivation of the channel surface.

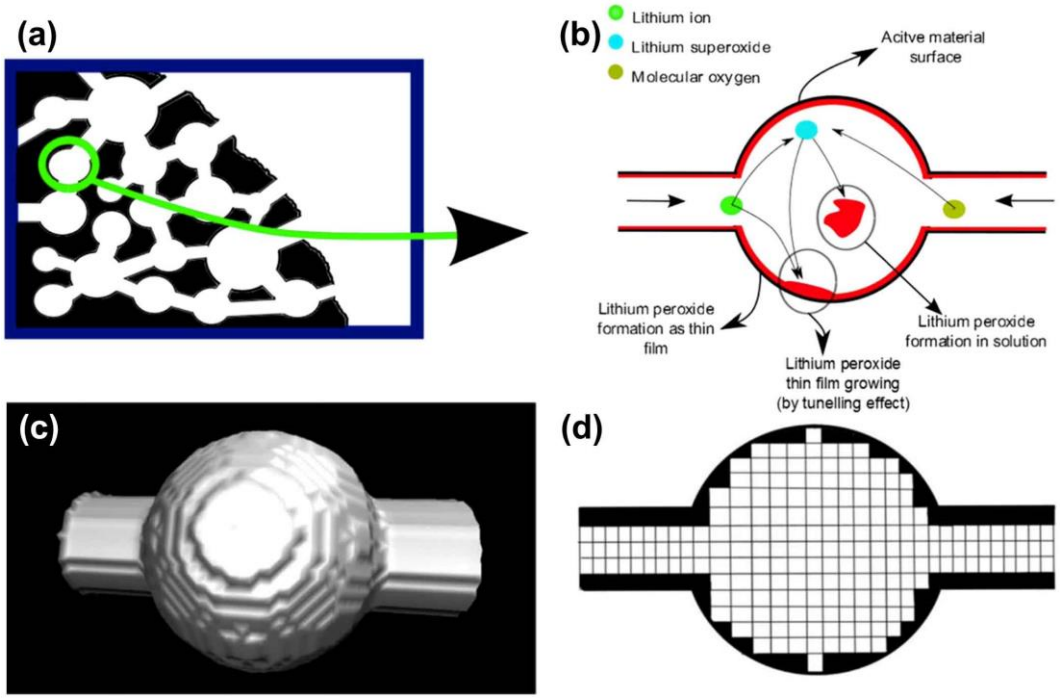


**Fig. 13** Schematic of (a) the nanoporous cathode structure, (b) different reactions considered in the present model, (c) 3D visualization of the simulated pore-channel system, and (d) 2D projection of the simulated pore-channel system with the cut-view of the grid structure indicated. Adapted from [224] with permission of The Electrochemical Society.

To probe the effect of precise electrode microstructures on the battery performance, a pore-scale transport resolved model was developed by Sun *et al.* [212], which can take any microstructure of the electrode and solid $Li_2O_2$ as a geometric input. The microscale computational domain ($\Omega$) consists of three distinct phases: electrolyte ($\Omega_1$), electrode ($\Omega_2$), and $Li_2O_2$ ($\Omega_3$), and the species and charge conservation are given in each domain. Different from Section 3.1 and 3.2 where only bulk values (volume-averaged values) are

applied, localized values of concentration and voltage near the active surface are used in governing equations in each domain without any approximations regarding the surface quantities. The effects of cathode nanostructure on the discharge performance were investigated through numerical implementation with an implicit 2D finite-volume method. As shown in **Fig. 14a**, at the same electrode surface area (S + W = 40 nm), different nanostructure spacings can have different effects on the battery performance. At a constant height of the nanostructure (H), as presented in **Fig. 14b**, the specific discharge capacity increases monotonically with increasing nanostructure spacing (S), while the discharge voltage does not change significantly. In addition to the finite-volume method, Jithin *et al.* employed a multi-relaxation time lattice Boltzmann method to solve the multi-physics coupling of transport and electrochemistry at the pore-scale of a non-aqueous Li-air battery [225]. They generated an idealized electrode-electrolyte porous media from the known macroscopic variables. Then, the mass transport and electrode structure changes due to $Li_2O_2$ formation were investigated. Through the pore-scale model, a detailed electrode microstructure can be focused [226], contributing to the understanding of the electrode morphological evolution.

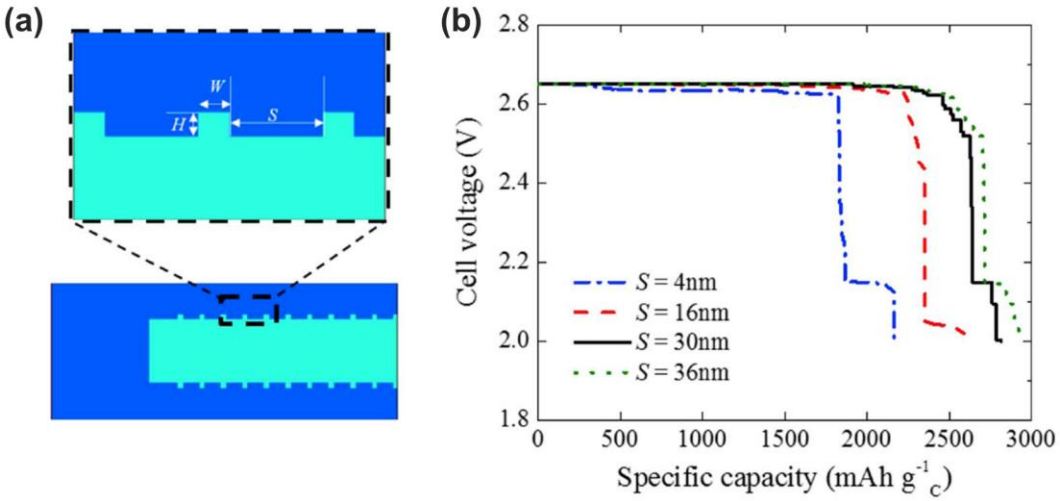

**Fig. 14** Pore-scale model: (a) schematic of square nanostructured cathode, where W, S and H denote the width, spacing and height of the nanostructure, respectively, (b) discharge voltage as a function of specific capacity at different nanostructure spacings. Reprinted from [212] with permission of The Electrochemical Society.

### 3.5.3 Multiscale three-dimensional reconstruction

To precisely model the discharge behavior, Bao *et al.* used a multiscale modeling approach where the mesoscale (10−1000 nm) and nanoscale (0.5−100 nm) features of a real air electrode were captured by effectively reconstructing its porous structure [227]. The porosity, surface area per unit volume ($a$), and pore size distribution were captured through a Monte Carlo sampling technique, and a cross section of the reconstructed 3D pore structure is shown in **Fig. 15a**, which is a good representation of the real electrode. The species transports, electrochemical reactions, and electrode structure evolutions were numerically solved on the reconstructed 3D mesoscale structure (**Fig. 15b**). The modeling framework is schemed in **Fig. 15c**. The nanoscale model calculates the correlation between the active surface percentage and the $Li_2O_2$ layer thickness in the nanoscale structure, which is passed along to the mesoscale model to calculate the constitutive relation of $a$ as a function of the averaged $Li_2O_2$ concentration in the mesoscale structure. In addition to the $Li_2O_2$ layer, the $Li_2O_2$ particles are also considered. The result is then put into the device-scale model to calculate the discharge curves. Therefore, this approach offers a reliable guidance to optimize the air electrode microstructures.

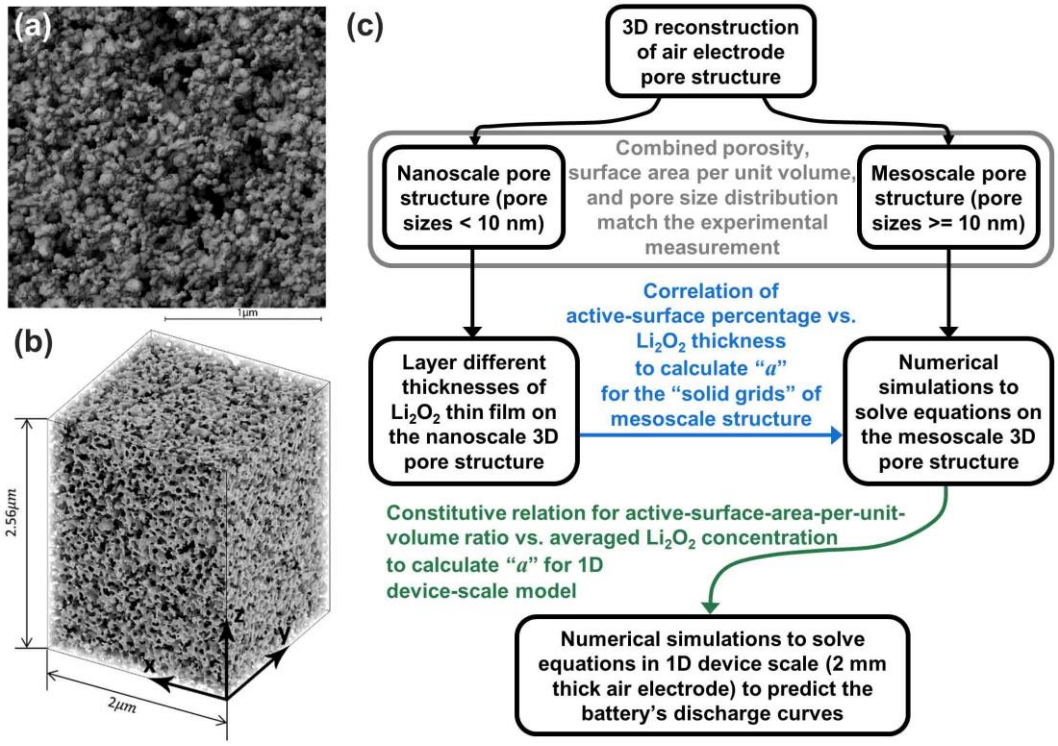


**Fig. 15** Multiscale modeling approach for non-aqueous Li-air batteries: (a) cross section of the reconstructed air electrode using the particle-packing method, (b) pore volumes of the reconstructed 3D mesoscale structure, and (c) diagram of the developed multiscale modeling framework. Adapted from [227] with permission of American Chemical Society.

### 3.6 Catalyst distribution

Catalysts are usually used in the air electrode to improve the electrochemical performance. As introduced in Section 2.1, the reaction kinetics and reaction mechanisms can be changed due to the different activities and adsorption free energies of catalyst materials. However, catalytic sites will become deactivated when passivated by the solid product. As introduced in Section 3.5, the accumulation of the solid product can affect the species transport (e.g., $O_2$), and eventually result in a low utilization of the catalyst

sites and low discharge capacity. Hence, understanding the effects of catalyst distribution inside the air electrode is crucial for the performance optimization.

Taylor *et al.* introduced discrete Pd nanoparticles distributed on the anodic aluminum oxide (AAO) nanopore walls to investigate the effect of catalyst position on mechanistic function, as schematically shown in **Fig. 16** [228]. They found that in both cases with and without Pd, the discharge product grows from the oxygen electrode side and infiltrates into the separator side during discharge. In addition, the product morphology transforms from planar to particulate structures due to the disproportionation reaction (Reaction IIIa). However, in the case of the AAO membrane without Pd, isolated partial products remain on the pore walls due to the inefficiency of the charge reaction. While in the case of Pd-decorated AAO membrane, the geometrically dispersed Pd catalyst sites result in uniform migration of the product interface during discharge and improved kinetics of oxidation, resulting in the improved energy efficiency and reduced irreversible capacity.

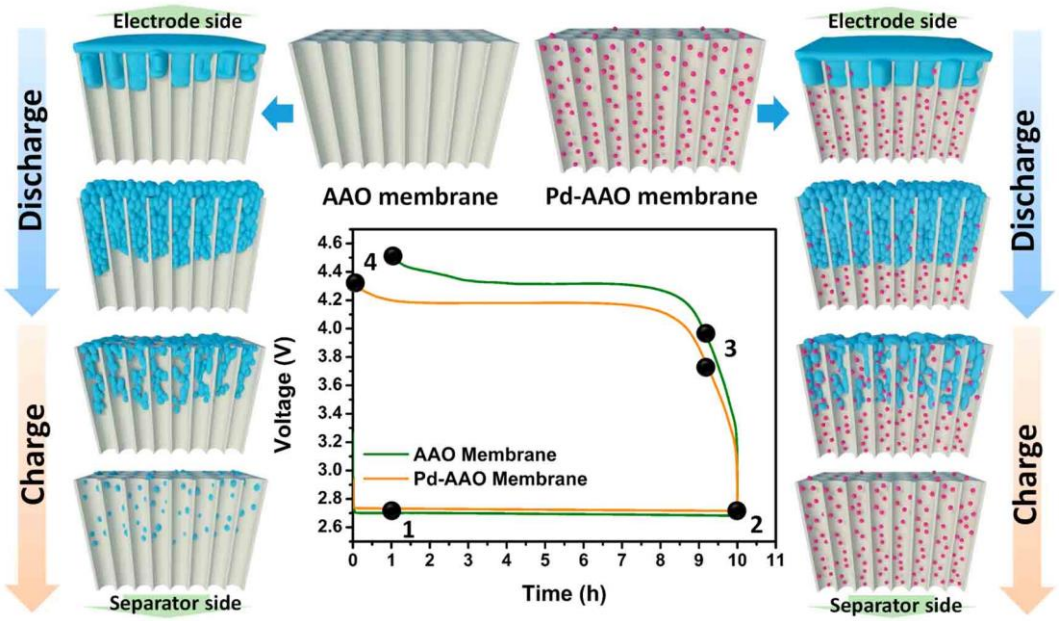

**Fig. 16** Morphological evolution schematic of products for discharge and charge in the AAO and Pd-AAO membrane. Each cross-section schematic corresponds to an electrochemical state in the charge/discharge profiles. Pink dots and blue regions indicate the Pd catalyst and discharge products, respectively. Adapted from [228] with permission of American Chemical Society.

To model the catalytically-induced growth of $Li_2O_2$ on selected sites along the pore surface, Ciacchi *et al.* developed a model through treating the air electrode as a set of cylindrical pores with radius $r_p$ [229]. The decrease of free pore volume was modified by a catalytic function $cat_s^t \in [0,1]$ according to

$$r_s^{t+1} = r_s^t - cat_s^t \cdot \Delta t \gamma c_s^t \tag{67}$$

where $r = r_p / r_p^0$, $c = c_{O_2,e} / c_{O_2,e}^0$ $r_p^0$ and $c_{O_2,e}^0$ is the pore radius and oxygen concentration initially. $\Delta t$ is a discrete time step, $\gamma$ is a parameter that related to the air electrode geometry. The effect of the catalytic function is to switch on ($cat_s^t$ = 1) or off ($cat_s^t$ = 0) the $Li_2O_2$ growth at position *s* in the pore at a given time *t*. Once the radius $r_s^t$ reaches a given threshold value at time *t*, the catalytic function at the next neighbors of the position *s* is switched on through $cat_{s-1}^t$ = 1 and $cat_{s+1}^t$ = 1. The threshold is defined as the fraction $(r_s^0 - r_s^t)/r_s^0$ of the initially free radius becoming occupied by newly deposited at time *t*.

**Fig. 17a** shows that the discharge product grows solely at the catalytic site initially. Once the threshold is reached, growth starts also at the neighboring sites. Due to the oxygen concentration difference (oxygen enters the pore from the left), the deposition rate is higher on the left than that on the right. Consequently, the threshold is reached earlier at the pore entrance side, leading to an asymmetric growth profile, as shown in Fig.

**17b**. Using a greedy algorithm with the free volume of a single pore after clogging as the objective function, the number and distribution of catalysts that lead to the minimum free pore volume can be optimized analytically, providing useful guidance for catalyst decoration along the thickness of the electrode.

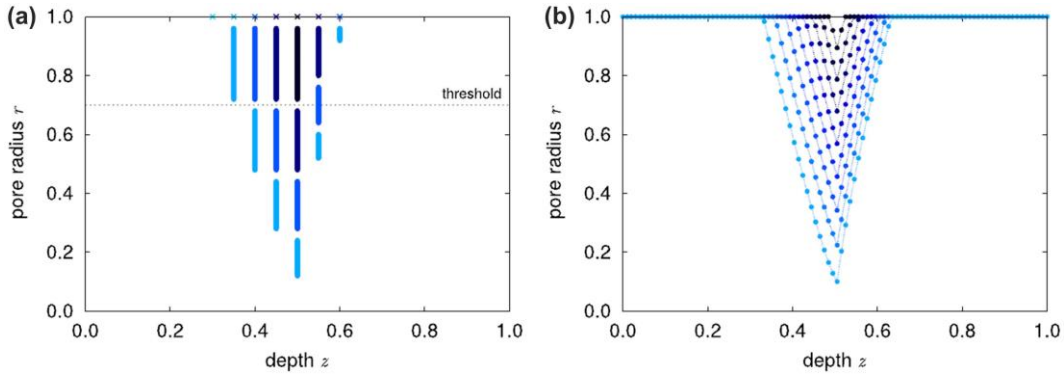


**Fig. 17** Growth profiles of $Li_2O_2$ in the presence of a single catalyst at the pore center. (a) Scheme of the employed propagation strategy for the catalytic function toward neighbor sites. (b) Simulation results until pore clogging with a threshold of 6%. The time evolution of the profiles is represented with colors ranging from dark to light blue. Reprinted from [229] with permission of The Electrochemical Society.

### 3.7 Side reactions

In the discharge process of non-aqueous Li-air batteries, the desired reaction is the formation of $Li_2O_2$ as the final product. However, due to the appearance of superoxide radical anions (Reaction II) which are highly active, the decomposition of electrolyte and electrode materials generally occur [83]. Even with ether-based electrolytes (e.g., DME, TEGDME) with improved stabilities, their decompositions have also been reported with the formation of side products as lithium carbonate, lithium formate, lithium acetate, $CO_2$ and $H_2O$ [53,230]. Hence, considering the side reactions and analyzing their effects on the battery performance are meaningful.

The modeling of electrolyte degradation and corresponding cycling behaviors was first reported by Sahapatsombut *et al.* in which $Li_2CO_3$ was considered as the main side product [231]. Two mechanisms were proposed for the $Li_2CO_3$ formation. The first one involves the superoxide radical anions as:

$$O_2 + 2e^- \xrightarrow{k_{1a}} 2O_2^- \quad \text{(XIVa)}$$

$$2O_2^- + 2CO_2 \xrightarrow{k_{1b}} C_2O_6^{2-} + O_2 \quad \text{(XIVb)}$$

$$C_2O_6^{2-} + 4Li^+ + 2O_2^- \rightarrow 2Li_2CO_3 + 2O_2 \quad \text{(XIVc)}$$

Overall: $4Li^+ + 4e^- + O_2 + 2CO_2 \rightarrow 2Li_2CO_3$ ($E^0$=7.19 V vs. $Li/Li^+$) (XIV)

where superoxide radical anion is initially formed (Reaction XIVa) and attacks $CO_2$ generated from the solvent decomposition to form $Li_2CO_3$. The reaction kinetics were expressed as:

$$j_{1a} = Fk_{1a}(c_{O_2,e})\left[-\exp\left(\frac{-\beta nF}{RT}\eta_m\right)\right] \quad (68)$$

$$r_{1b} = k_{1b}(c_{O_2^-,e})(c_{CO_2,e}) \quad (69)$$

where $k_{1a}$ and $k_{1b}$ are the rate constants for the electrochemical reaction to form $O_2^-$ and chemical reaction to generate $Li_2CO_3$, respectively. $\eta_m$ is surface or activation overpotential for individual reaction, $m$, at the air electrode. $c_{O_2^-,e}$ and $c_{CO_2,e}$ are the concentration of $O_2^-$ and $CO_2$ in the electrolyte, respectively. Here a Tafel form was used in Eq. 68 rather than the Butler-Volmer form as the large kinetic overpotential during discharge puts the reaction in the Tafel region and considers the irreversible formation of $O_2^-$ for $CO_2$ reduction. In addition, it has been demonstrated that the Reaction XIVb is first-order and is the rate determining step [232], so that the other reaction (Reaction XIVc) was considered as equilibrium.

The second reaction mechanism is the direct reduction of $CO_2$ as:

$$CO_2 + e^- \xrightarrow{k_{2a}} CO_2^- \quad \text{(XVa)}$$

$$CO_2^- + CO_2 + e^- \xrightarrow{k_{2b}} CO_3^{2-} + CO \quad \text{(XVb)}$$

$$2Li^+ + CO_3^{2-} \rightarrow Li_2CO_3 \quad \text{(XVc)}$$

Overall: $2CO_2 + 2Li^+ + 2e^- \rightarrow Li_2CO_3 + CO$ ($E^0$=2.49 V vs. $Li/Li^+$) (XV)

The kinetic for this reaction was systematically proposed by Welford *et al.* as [233]:

$$r_2 = \frac{k_1}{1+K'}(c_{CO_2,e})\exp\left(\frac{-\alpha_{CO_2}F}{RT}\eta_m\right) \quad (70)$$

in which

$$K' = \frac{k_1}{k_2}\exp\left(\frac{-\alpha_{CO_2}F}{RT}\eta_m\right) \quad (71)$$

where $k_1$ and $k_2$ are the rate constants for the electrochemical reaction, $\alpha_{CO_2}$ is the transfer coefficient which is given the value as 0.43 ± 0.05.

The degradation of solvent was described as:

$$O_2 + e^- \xrightarrow{k_{sol}} O_2^- \quad \text{(XVIa)}$$

$$O_2^- + [Solvent] \rightarrow [Solvent]^- \quad \text{(XVIb)}$$

$$[Solvent]^- + O_2 \rightarrow CO_2 + H_2O + HCO_2Li + CH_3CO_2Li \quad \text{(XVIc)}$$

Overall: $2O_2 + [Solvent] + e^- \rightarrow CO_2 + H_2O + HCO_2Li + CH_3CO_2Li$ (XVI)

Here only the $CO_2$ generated from the solvent degradation was accounted. Considering the irreversible decomposition of the solvent, a Tafel form was used to address this kinetic expression as:

$$j_{sol} = Fk_{sol}(c_{O_2,e})\left[-\exp\left(\frac{-\beta nF}{RT}\eta_m\right)\right] \quad (72)$$

where $k_{sol}$ is the rate constant for the electrochemical reaction to form $CO_2$ and other side products, and the solvent concentration was taken as a constant.

As all reactions occurred during discharge, the conservation of current became:

$$\nabla \cdot \boldsymbol{i}_l = \sum_m a j_m \tag{73}$$

Eq. 73 includes the formation of solid products ($Li_2O_2$ and $Li_2CO_3$) and the decomposition of the solvent. In addition, the volume fraction of the solid discharge products ($Li_2O_2$ and $Li_2CO_3$) was expressed by:

$$\frac{\partial \varepsilon_p}{\partial t} = \sum_{\text{solid phase } m} a j_m \frac{M_m}{nF\rho_m} \tag{74}$$

With these side reactions being considered, the modeling results for initial ten cycles of a battery are shown in **Fig. 18a**. The discharge voltage during cycling was around 2.5−2.7 V, whereas the charge voltages increased over time around 4.0−4.25 V. The increase in the charge overpotential could be attributed to the loss of active surfaces due to the accumulation of irreversible $Li_2CO_3$ during discharge (**Fig. 18b**), consistent with the experimental observations [234].

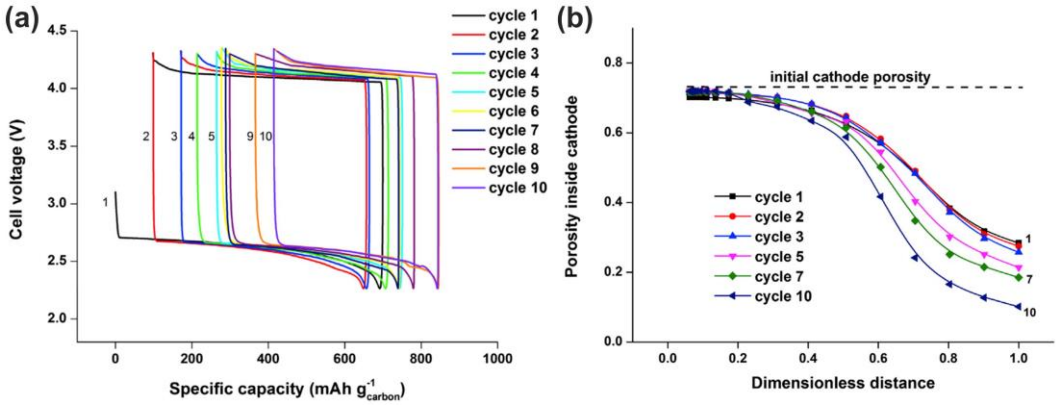


**Fig. 18** Modeling results of the cycling performance of a non-aqueous Li-air battery operating in pure oxygen with side reactions: (a) variation of voltage-capacity curves; (b)

local porosity profiles inside the cathode electrode. Adapted from [231] with permission of Elsevier.

Using the similar method, the operation in ambient air has also been modeled considering the low oxygen pressure and the formation of $Li_2CO_3$ [235]. However, when operating in ambient air, in addition to the proposed side reactions (Reactions XIV−XVI), the following side reactions also occur in the air electrode:

$$4Li^+ + 4e^- + O_2 + 2CO_2 \rightarrow 2Li_2CO_3\ (E^0=3.82\ \text{V vs. Li/Li}^+) \quad \text{(XVII)}$$

$$4Li^+ + 4e^- + O_2 + 2H_2O \rightarrow 4LiOH\ (E^0=3.39\ \text{V vs. Li/Li}^+) \quad \text{(XVIII)}$$

$$2Li_2O_2 + 2H_2O \rightarrow 4LiOH + O_2 \quad \text{(XIX)}$$

$$2LiOH + CO_2 \rightarrow Li_2CO_3 + H_2O \quad \text{(XX)}$$

which include not only the electrochemical reactions but also the chemical reactions to form the solid side products LiOH and $Li_2CO_3$, both are irreversible in the carbon electrode [95,236]. In addition, it has been shown that $H_2O$ has a more detrimental influence on the battery performance due to the surface passivation by LiOH [96]. Therefore, to more realistically model the operating behavior in ambient air, more side reactions should be taken into account.

### 3.8 Volume change

In non-aqueous Li-air batteries, a porous separator is usually applied and the electrolyte is in contact with the lithium anode. Volume change can occur due to the lithium metal oxidation/reduction in the lithium electrode and the formation/decomposition of solid $Li_2O_2$ in the air electrode during discharge/change [237], which affects the electrolyte distribution, resulting in the changes of two-phase

boundaries [188]. In most modeling works, although a solid separator (APL) is assumed so that the electrolyte is confined in the air electrode, the electrolyte movement due to the volume change of solid $Li_2O_2$ is still seldom considered.

Dutta *et al.* developed a model to account for the movement of lithium electrode interface during charge and discharge using the moving boundary method [238]. **Fig. 19** shows the interface location of the lithium electrode at the beginning of discharge and at an instant time *t*, indicating a change in the volume of $\Delta V_{\mathrm{Li}} = \delta(t) S_{\mathrm{cs}}$, where $\delta(t)$ is the length between the lithium interface and the separator, and $S_{\mathrm{cs}}$ is the cross-section area of the battery (assume anode and cathode share the same superficial surface area). Considering the conservation of lithium, the volume change is expressed as:

$$\Delta V_{\mathrm{Li}} = \frac{M_{\mathrm{Li}} S_{\mathrm{cs}}}{s_{\mathrm{Li}} \rho_{\mathrm{Li}} F} \int_0^{T_{time}} I_{\mathrm{app}} dt \tag{75}$$

where $M_{\mathrm{Li}}$, $\rho_{\mathrm{Li}}$, $s_{\mathrm{Li}}$ are the molecular weight, density, and stoichiometric coefficient of lithium, respectively, and $I_{\mathrm{app}}$ is the applied current density, $T_{time}$ is the final time. Through Eq. 75, the boundary velocity ($v_{\mathrm{b}}$) of the lithium electrode and total displacement ($\delta_{T_{time}}$) are obtained as:

$$v_{\mathrm{b}} = \frac{M_{\mathrm{Li}} I_{\mathrm{app}}}{s_{\mathrm{Li}} \rho_{\mathrm{Li}} F} \tag{76}$$

$$\delta_{T_{time}} = \delta(t = T_{time}) = \frac{M_{\mathrm{Li}}}{s_{\mathrm{Li}} \rho_{\mathrm{Li}} F} \int_0^{T_{time}} I_{\mathrm{app}} dt \tag{77}$$

To obtain the governing equations for pertinent variables, a moving boundary technique with coordinate transformation is used. As shown in **Fig. 19**, assuming that the electrolyte occupies the gap between the lithium interface and the separator, the origin of

the moving coordinate ($\xi$) is at the reaction interface of the lithium electrode. If the origin of fixed coordinate system ($x$) is located at the initial lithium-electrolyte interface position, the relation between moving and fixed coordinate can be given as:

$$\xi = x + \int_0^t \alpha_v(x,t)dt \tag{78}$$

where $\alpha_v(x,t)$ is the velocity of the grid points in moving coordinate system:

$$\alpha_v(x,t) = v_b\left[1 - \frac{x+\delta}{\delta_t}\right] \tag{79}$$

Here $\delta_t$ is the length of the electrolyte region at any instant $t$, and it consists of the separator ($L_{Sep}$), the cathode region ($L_{Cat}$) and the space due to boundary movement ($\delta$):

$$\delta_t = \delta + L_{Sep} + L_{Cat} \tag{80}$$

Thus, the temporal and spatial derivative terms can be rewritten as:

$$\frac{\partial}{\partial t} = \frac{\partial}{\partial t} + v_b\left(1 - \frac{\xi - \alpha_v t + \delta}{\delta_t}\right)\frac{\partial}{\partial \xi} \tag{81a}$$

$$\frac{\partial}{\partial x} = \left(1 - \frac{v_b}{\delta_t}\right)\frac{\partial}{\partial \xi} \tag{81b}$$

When putting them into the governing equations for lithium ion and oxygen transport (Eqs. 1 and 11), the corresponding descriptions in the moving coordinate system are obtained.

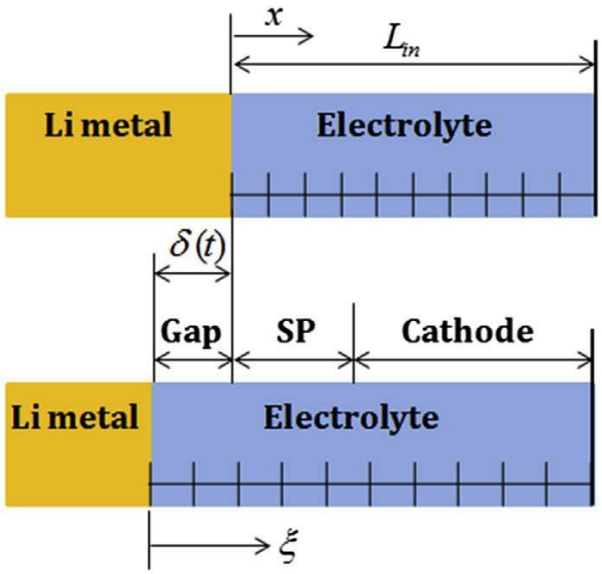


**Fig. 19** Schematics of the one-dimensional computational domain at the beginning of discharge and at an instant time *t* [238]. Adapted from [231] with permission of Elsevier.

The increased volume of solid $Li_2O_2$ will also push the electrolyte. For an incompressible electrolyte, the effective surface area $S_{cs}^{eff}$ due to electrolyte movement is:

$$S_{cs}^{eff}(t) = S_{cs} \cdot \frac{\varepsilon_{Sep} L_{Sep} + \int_0^{L_{Cat}} \varepsilon_e(t=0)dx}{\delta(t) + \varepsilon_{Sep} L_{Sep} + \int_0^{L_{Cat}} \varepsilon_e(t)dx} \tag{82}$$

which indicates that the effective area for the reaction is also affected by the volume change.

In addition to the electrolyte movement caused by lithium metal and solid $Li_2O_2$, another issue that leads to the volume change is the electrolyte evaporation during operation, especially for those solvents with high vapor pressure [25]. Huang *et al.* developed a model to analyze the electrolyte change with including the air chamber that provides oxygen to the battery [239]. The velocity of the moving electrolyte level ($v_1$) consists of two parts:

$$v_1 = -(v_{1v} + v_{1e}) \tag{83}$$

where $v_{1v}$ is the velocity due to the liquid replacing the vanishing solid phase (lithium oxidation and lithium peroxide formation), and $v_{1e}$ is the velocity caused by solvent evaporation:

$$v_{1v} = \frac{I_{app}}{\varepsilon_e F}\left(\frac{M_{Li}}{\rho_{Li}} - \frac{M_{Li_2O_2}}{2\rho_{Li_2O_2}}\right) \tag{84}$$

$$v_{1e} = \frac{\int_{S_{es}} N_{sv} dS}{S_{es}} \frac{M_{sv}}{\varepsilon_e \rho_{sv}} \tag{85}$$

where $S_{es}$ denotes the area of the electrolyte surface and the subscript sv denotes solvent. The molar flux of evaporated solvent $N_{sv}$ is calculated by:

$$N_{sv} = -D_{sv} \left.\frac{\partial c_{sv}}{\partial x}\right|_{S_{es}} \tag{86}$$

where $D_{sv}$ and $c_{sv}$ are respectively the diffusion coefficient and concentration of solvent vapor in the air. With the velocities of the moving boundaries, the arbitrary Lagrangian-Eulerian method is employed to describe the geometry deformation [240].

A key finding from this work is that the volume fraction of $Li_2O_2$ shows a peak in the middle of the air electrode when the electrolyte level drops during discharge [239]. This finding is different from the previously predicted $Li_2O_2$ distribution which decreases from the air side to the inner side, indicating the importance in considering the electrolyte movement to more realistically predict the discharge behaviors.

### 3.9 Charge process

Most reported modeling works mainly focused on the discharge process. In Sahapatsombut's work [140,231,235], the decomposition of $Li_2O_2$ is assumed to be the reversible process of $Li_2O_2$ formation based on Reaction IV. However, the charge process

is much more complex with various proposed mechanisms [87-91], among which the reversible reaction is seldom reported [82]. Hence, various factors in the charge process should be considered in modeling.

### 3.9.1 Effect of $Li_2CO_3$

Lithium carbonates are formed during the working processes of non-aqueous Li-air batteries. In Section 3.7, $Li_2CO_3$ is treated as an irreversible side product that covers the surface areas of the air electrode, resulting in the capacity fading in cycling [231]. McCloskey *et al.* found that $Li_2O_2$ reacts with the carbon electrode and forms approximately a monolayer of $Li_2CO_3$ at the carbon-$Li_2O_2$ interface, while the reaction with the electrolyte forms approximately a monolayer of carbonate at the $Li_2O_2$-electrolyte interface during charge, as schematically shown in **Fig. 20a** [241]. They developed an electrochemical model to demonstrate the effect of $Li_2CO_3$ on the discharge and charge processes. On charge, the current associated with the OER of $Li_2O_2$, occurring at a low overpotential of about 0.3 V, was given by:

$$i_{\mathrm{Li_2O_2}} = -i_0 c_{\mathrm{Li_2O_2}}^{\mathrm{sur}} \exp\left[-\max\left(\frac{E-\Delta G}{b_1}, 0\right)\right] \tag{87}$$

where $c_{\mathrm{Li_2O_2}}^{\mathrm{sur}}$ is the surface concentration of $Li_2O_2$ and $b_1$ stands for the corresponding Tafel slope. The reaction associated with the formation of $Li_2CO_3$ is allowed to continue during change. In addition, the reaction associated with the oxidation of $Li_2CO_3$ was chosen to occur at a high potential of about 4.2 V with the overall current of:

$$i_{\mathrm{Li_2CO_3}} = -i_0 c_{\mathrm{Li_2CO_3}}^{\mathrm{sur}} \exp\left[-\max\left(\frac{E-\Delta G}{b_2}, 0\right)\right] + i_{\mathrm{Li_2CO_3,D}} \tag{88}$$

where $c^{sur}_{Li_2CO_3}$ is the surface concentration of $Li_2CO_3$, $b_2$ stands for the corresponding Tafel slope, and $i_{Li_2CO_3,D}$ is the current for background reaction. The overall current ($i_{oa}$) during charge is given by:

$$i_{oa} = i_{Li_2O_2} + i_{Li_2CO_3} \tag{89}$$

The modeling results are shown in **Fig. 20b**, which qualitatively matches well with the experimental data. The charge potential depends on the relative surface concentrations of $Li_2O_2$ and $Li_2CO_3$, and the existence of one monolayer of carbonate at the $Li_2O_2$-electrolyte interface drives the charging potential to be larger than 4 V. The result indicated that eliminating the formation of this monolayer of carbonate at the interface is essential for a low charge voltage.

### 3.9.2 Effect of $Li_2O_2$ morphology

As introduced in Section 3.3, various kinds of $Li_2O_2$ morphologies have been observed during the discharge process. The impact of $Li_2O_2$ morphology on the charge process has been modeled by Franco *et al.* [242]. As shown in **Fig. 20c**, the thin film and the large particles are set to coexist after discharge, and the thin film is assumed to be composed of small particles. Both the thin-film and the large particles are assumed to be hemispherical. In addition, different decomposition mechanisms are adopted for $Li_2O_2$ based on their particle sizes, as presented in the chart of **Fig. 20c**. For the large particles ($Li_2O_{2(p)}$), the oxidation starts with the deintercalation of $Li^+$ from its particle surface to form $LiO_2$-like species ($LiO_{2(s)}$). Then, the $LiO_{2(s)}$ is dissolved into the electrolyte in the form of ion pair ($LiO_{2(ip)}$), followed by a further oxidation on the electrode surface to produce $Li^+$ and $O_2$. For the thin film particles ($Li_2O_{2(f)}$), a two-step decomposition mechanism is adopted to directly form $LiO_{2(ip)}$, followed by its subsequent oxidation.

Because of the very fast decomposition of $LiO_{2(ip)}$ during the third step of charge, the oxidation of $Li_2O_{2(f)}$ can be regarded as a one-step reaction involving two electrons.

The electrochemical reaction rate at the air electrode is characterized by the local faradaic current density $i^{\text{far}}$ as:

$$i_j^{\text{far}} = nF\left\{k_{\text{f}j}\prod_i c_i^{s_{i,j}}\exp\left[\frac{(1-\alpha)nF(\Psi-\Phi)}{RT}\right]-k_{\text{b}j}\prod_i c_i^{s_{i,j}}\exp\left[\frac{-\alpha nF(\Psi-\Phi)}{RT}\right]\right\} \quad (90)$$

where $c_i$ is the dimensionless concentration (activity), $s_{i,j}$ is the stoichiometric coefficient of species $i$ in reaction $j$, $k_{\text{f}j}$ and $k_{\text{b}j}$ are the heterogeneous rate constants, respectively. $\psi$ and $\Phi$ are the electrostatic potentials of the electrode and the electrolyte, respectively. The relationship between the local faradaic current density and the applied current is:

$$I_{\text{app}} = \int_0^V \sum_j \frac{A_j}{V}\cdot i_j^{\text{far}} dV \quad (91)$$

where $A_j$ is the active surface area of the electrochemical reaction $j$. For large (p) and thin-film (f) particles, the active surface areas are expressed as:

$$A_{\text{p}} = 2\pi r_{\text{p}}^2 N_{\text{p}} V \quad (92a)$$

$$A_{\text{f}} = 2\pi r_{\text{f}}^2 N_{\text{f}} V \quad (92b)$$

where $r_{\text{p}}$, $r_{\text{f}}$ and $N_{\text{p}}$, $N_{\text{f}}$ are the radius and density of the large and thin-film particles, respectively. The $LiO_{2(ip)}$) oxidation takes place mainly on the uncovered part of the electrode by $Li_2O_2$, which gives the active surface area ( $A_{\text{LiO}_{2(ip)}}$ ) for the reaction as:

$$A_{\text{LiO}_{2(ip)}} = A - \pi r_{\text{f}}^2 N_{\text{f}} V - \pi r_{\text{p}}^2 N_{\text{p}} V \quad (93)$$

For the chemical reaction for $LiO_{2(s)}$ dissolution, the reaction rate is described by:

$$S_{\text{che}} = k_{\text{f}} A_{\text{p}} \theta_{\text{LiO}_2,\text{p}} - k_{\text{b}} \frac{c_{\text{LiO}_{2(ip)}}}{c_{\text{LiO}_{2(ip)},\text{ref}}} \quad (94)$$

where $k_f$ and $k_b$ are the kinetic rate constants for the forward and backward processes, respectively; $c_{LiO_{2(ip)}}$ is the concentration of $LiO_2$ in the electrolyte. $\theta_{LiO_2,p}$ stands for the surface coverage of $LiO_{2(s)}$ on the $Li_2O_2$ large particles surface and is given by:

$$\theta_{LiO_2,p} = \begin{cases} \dfrac{V_{LiO_{2(s)}}}{\delta N_p V 2\pi r_p^2}, & \dfrac{V_{LiO_{2(s)}}}{\delta} < N_p V 2\pi r_p^2 \\ 1, & \dfrac{V_{LiO_{2(s)}}}{\delta} \geq N_p V 2\pi r_p^2 \end{cases} \tag{95}$$

where $V_{LiO_{2(s)}}$ is the volume of the $LiO_{2(s)}$.

For the electroactive species that are soluble in the electrolyte ($Li^+$, $O_2$, and $LiO_{2(ip)}$), it is assumed that the mass transport is governed by diffusion. The evolution of the large $Li_2O_2$ particles volume during the charge is given by:

$$V_p(t) = V_{p,0} + \omega_{Li_2O_2} \int_0^t S_p(t) V dt \tag{96}$$

where $V_{p,0}$ represents the initial volume of the large $Li_2O_2$ particles, $\omega_{Li_2O_2}$ is the molar volume, $S_p$ is the evolution rate of $Li_2O_2$ particles. Under the assumption of isotropic volume change, the evolution of the large particles size is obtained as:

$$r_p(t) = \left( \frac{3}{2\pi N_p V} V_p(t) \right)^{1/3} \tag{97}$$

With this model, the simulated charge voltage curve is shown in **Fig. 20d**, which is a two-step process. During the initial stage of the charge process, decomposition of small particles takes place, which continues until its complete removal, and then the decomposition of large particles starts. This stepwise behavior of the charge curve implies that small particle oxidation accounts for the lower potential plateau whereas

large particle oxidation is related to the higher potential plateau, fitting well with experimental results [243].

### 3.9.3 Effect of redox mediator

The charge voltages for non-aqueous Li-air batteries are usually high, owing to the difficulties in charge transport between solid $Li_2O_2$ and electrode surface. To facilitate the charge process, a redox mediator (RM) is introduced into the electrolyte. On charge, the RM is oxidized to $RM^+$ at the air electrode surface as:

$$RM \rightarrow RM^+ + e^- \quad \text{(XXI)}$$

which in turn oxidizes the solid $Li_2O_2$ and results in the regeneration of RM:

$$Li_2O_2 + 2RM^+ \rightarrow 2Li^+ + O_2 + 2RM \quad \text{(XXII)}$$

Consequently, the RM acts as an electron-hole transfer agent that permits efficient oxidation of solid $Li_2O_2$, resulting in the low charge potential and long cycle life. Until now, various kinds of RMs have been reported, including tetrathiafulvalene (TTF) [244], lithium iodine (LiI) [185], iron phthalocyanine (FePc) [245], 2,2,6,6-tetramethylpiperidinyloxyl (TEMPO) [246], indium tri-iodide ($InI_3$) [247], and lithium bromide (LiBr) [248]. To elucidate the impact of the major factors of RMs, Janek *et al.* derived an electrochemical model using TEMPO as an example [249]. The model is restricted to the intermediate space between $Li_2O_2$ and an uncovered part of the carbon electrode with a constant distance *d*, as shown in **Fig. 20e**. On the steady state conditions, the concentrations of RM and $RM^+$ at the carbon electrode ($x$ = 0) control the electrode potential by the Nernst equation:

$$E = E^0 + \frac{RT}{nF} \ln \frac{c_{RM^+}^{SS}(0)}{c_{RM}^{SS}(0)} \quad (98)$$

where $c^{SS}_{RM^+}(x)$ and $c^{SS}_{RM}(x)$ are the concentrations of $RM^+$ and RM at position *x* under steady state conditions, and satisfy the relationship as:

$$c^{SS}_{RM^+}(x) + c^{SS}_{RM}(x) = c^{0}_{RM} \tag{99}$$

where $c^{0}_{RM}$ is the initial concentration of the RM. Fick's law is adapted to describe the charge transport along the distance *d*:

$$j^{SS} = nFD_{RM}\frac{c^{SS}_{RM}(d) - c^{SS}_{RM}(0)}{d} \tag{100}$$

where $j^{SS}$ is the current density under stationary conditions, and $D_{RM}$ is the diffusion coefficient of RM. From **Fig. 20e**, the redox potential $E^0$ has a distinctly higher impact on the charging profiles than the diffusion coefficient, while the parameter *d* describes the lengths of the $RM/RM^+$ diffusion paths. Based on a multistep reaction mechanism, Bessler *et al.* further modeled the effect of RM on the charge voltage, as shown in **Fig. 20f** [250]. The charge voltage is failed in reproducing the particular shape of the experimental charge curve, implying the complexity of the reaction mechanism for further investigation.

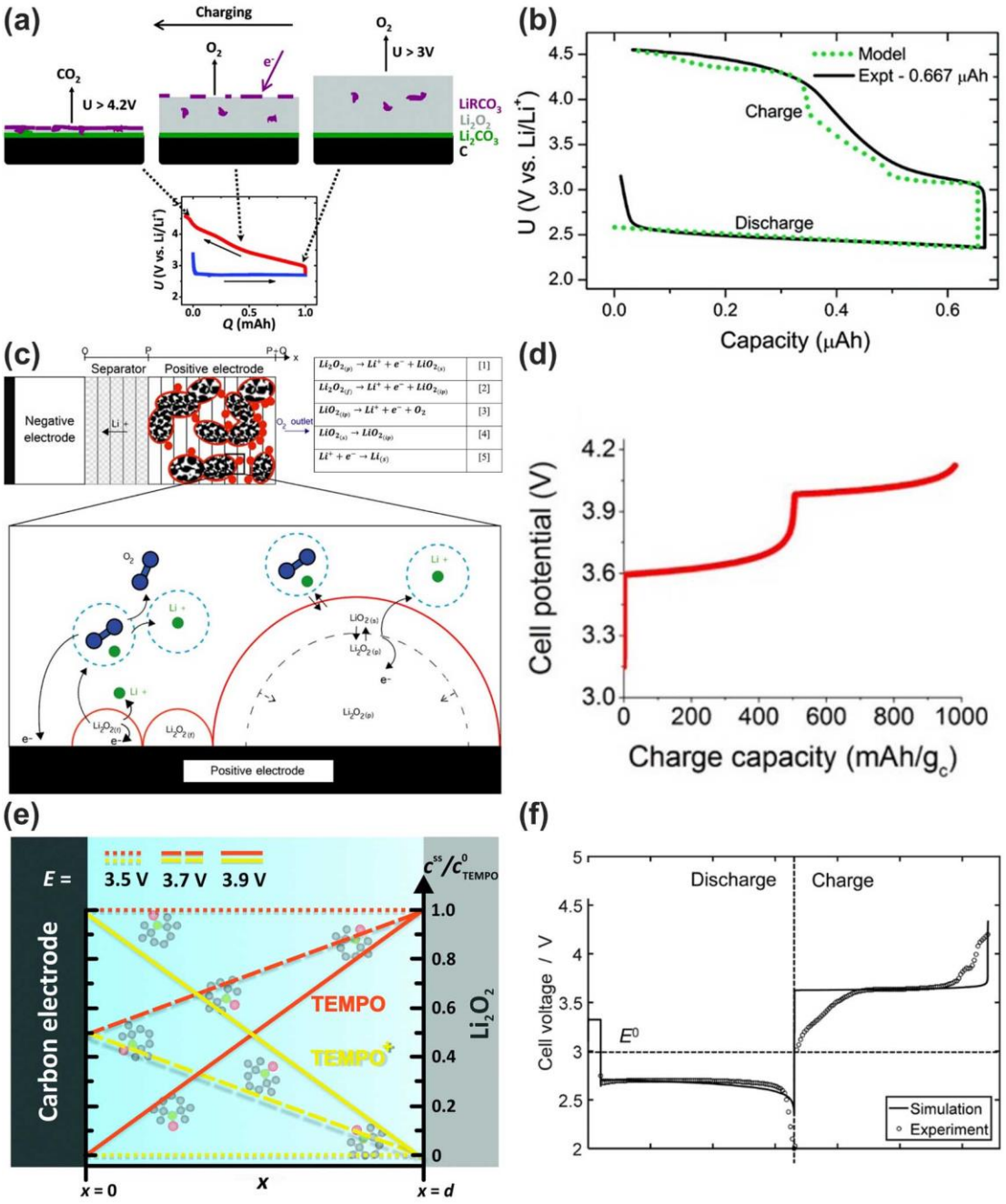


**Fig. 20** Scheme and result for the charge process: (a) charge process with the formation of lithium carbonates; (b) comparisons between experimental and kinetic model results. Adapted from [241] with permission of American Chemical Society. (c) charge mechanisms for thin-film (small hemispheres) and large $Li_2O_2$ large particles (large hemispheres), inset chart illustrates the possible reaction routes; (d) simulated result of

potential evolution as a function of charge capacity. Adapted from [242] with permission of American Chemical Society. (e) TEMPO and $TEMPO^+$ concentration profiles between the carbon electrode and the $Li_2O_2$ surface at different electrode potentials. Reprinted from [249] with permission of The Royal Society of Chemistry. (f) voltage as a function of time compared to experimental data. Adapted from [250] with permission of American Chemical Society.

### 3.10 Critical challenges for non-aqueous systems

Accompanied with experimental findings of non-aqueous Li-air batteries, modeling and simulation have been adopted to understand the working process, predict the performance, and optimize the electrode and battery structures. We summarized the reported modeling works in **Table 1**. The critical challenges facing the modeling and simulation are discussed here.

**Table 1** Summary of modeling works of non-aqueous Li-air batteries

| Published year | $Li^+$ transport | $O_2$ transport | $Li_2O_2$ formation mechanism | $Li_2O_2$ morphology vs. current | Transport through $Li_2O_2$ | Reaction kinetics | Electrode structure evolution | Catalyst distribution | Side reaction | Electrolyte volume change | Charge process | Remark | Ref. |
|---|---|---|---|---|---|---|---|---|---|---|---|---|---|
| 2007 | | ✓ | | | | ✓ | ✓ | | | | | Continuum | [158] |
| 2009 | | ✓ | | | | ✓ | ✓ | | | | | Continuum | [159] |
| 2010 | ✓ | ✓ | | | ✓ | ✓ | ✓ | | | | | Continuum | [163] |
| | ✓ | ✓ | | | ✓ | ✓ | ✓ | | | | | Continuum | [162] |
| 2011 | ✓ | ✓ | | | | ✓ | ✓ | | ✓ | | | Continuum | [251] |
| 2012 | ✓ | ✓ | | | | ✓ | ✓ | | | | | Continuum | [157] |
| | ✓ | ✓ | | | ✓ | ✓ | | | | | | Analytical | [209] |
| | | | | | | ✓ | | | ✓ | | ✓ | Kinetics | [241] |
| 2013 | ✓ | ✓ | | | ✓ | ✓ | ✓ | | | | ✓ | Continuum | [140] |
| | | | | ✓ | | ✓ | | | | | | Nonequilibrium thermodynamics | [205] |
| | ✓ | ✓ | | | ✓ | ✓ | | | | | | Analytical | [216] |
| | ✓ | ✓ | | | | ✓ | ✓ | | | | | Continuum | [221] |
| | ✓ | ✓ | | | | ✓ | | | | | | Meso-scale | [226] |
| | ✓ | ✓ | | | ✓ | ✓ | ✓ | | ✓ | | ✓ | Continuum | [231] |
| 2014 | | | ✓ | | | ✓ | | | | | | Kinetics | [198] |

| | | | | | | | | | | | | | | |
|---|---|---|---|---|---|---|---|---|---|---|---|---|---|---|
| | ✓ | ✓ | | | ✓ | ✓ | ✓ | | | | | Continuum | [210] | |
| | | ✓ | | | ✓ | ✓ | ✓ | | | | | Continuum | [214] | |
| | ✓ | ✓ | | | ✓ | ✓ | ✓ | | | | | Continuum | [222] | |
| | ✓ | ✓ | | | ✓ | ✓ | ✓ | | ✓ | | ✓ | Continuum | [235] | |
| | ✓ | ✓ | | | ✓ | ✓ | ✓ | | | ✓ | | Continuum | [252] | |
| | ✓ | ✓ | | ✓ | ✓ | ✓ | ✓ | | | | | Continuum | [171] | |
| | ✓ | ✓ | | | | ✓ | ✓ | | | | | Continuum | [172] | |
| | | ✓ | | | | | | | | | | Continuum | [194] | |
| | | ✓ | ✓ | | ✓ | ✓ | ✓ | | | | | Continuum | [200] | |
| | | | | ✓ | | | ✓ | | | | | Nucleation and growth | [206] | |
| 2015 | ✓ | ✓ | | | ✓ | ✓ | ✓ | | | | | Pore-scale | [212] | |
| | | | | | ✓ | | | | | | | Continuum | [215] | |
| | ✓ | ✓ | | | ✓ | | ✓ | | | | | Continuum | [217] | |
| | ✓ | ✓ | | | ✓ | ✓ | ✓ | | | | | Analytical | [218] | |
| | ✓ | ✓ | | | ✓ | ✓ | ✓ | | | | | Continuum | [223] | |
| | | ✓ | | | | ✓ | ✓ | ✓ | | | | Continuum | [229] | |
| | ✓ | ✓ | | | ✓ | ✓ | ✓ | | | | | Continuum | [253] | |
| | ✓ | ✓ | | | ✓ | ✓ | ✓ | | | | | Continuum | [187] | |
| | ✓ | ✓ | | | ✓ | ✓ | ✓ | | | | | Continuum | [193] | |
| | | | | | | ✓ | ✓ | | | | | Analytical | [199] | |
| | ✓ | ✓ | | | ✓ | ✓ | ✓ | | | | | Continuum | [208] | |
| 2016 | ✓ | ✓ | ✓ | | ✓ | ✓ | ✓ | | | | | Kinetic Monte Carlo | [224] | |
| | ✓ | ✓ | | | ✓ | ✓ | ✓ | | | | | Lattice Boltzmann Simulation | [225] | |
| | ✓ | ✓ | | | ✓ | ✓ | ✓ | | | ✓ | | Continuum | [239] | |
| | ✓ | ✓ | | | ✓ | ✓ | | | | | ✓ | Continuum | [242] | |
| | ✓ | ✓ | | | ✓ | ✓ | | | | | ✓ | Continuum | [250] | |
| | ✓ | ✓ | ✓ | | ✓ | ✓ | ✓ | | | | | Continuum | [254] | |
| 2017 | ✓ | ✓ | ✓ | | | ✓ | ✓ | ✓ | | | | Kinetic Monte Carlo | [255] | |
| | ✓ | ✓ | | | ✓ | ✓ | ✓ | | | ✓ | | Continuum | [256] | |

The simulation results of lithium ion and oxygen transport in non-aqueous electrolytes rely on the accuracies of experimental data, such as the electrolyte properties and the reaction rates. However, most of these data are lacking in the literature. For instance, the transport properties (e.g., oxygen solubility, diffusion coefficient) used in calculations are usually based on carbonate-based electrolytes (e.g., EC, DMC) [38], which are proven to be unstable and no longer applied in experiments. Whereas the

related properties of the most widely used solvents (e.g., DME, TEGDME, and DMSO) have rarely been reported [257], causing difficulties in quantitatively prediction of the electrochemical performance. To improve the result accuracies, efforts should be made to characterizing and measuring these fundamental data.

For the solid discharge product $Li_2O_2$, a lot of works have been devoted to revealing its properties. Until now, the reaction route, morphology formation, and transport mechanism have been considered. To get a profound understanding of its influences on the discharge performance, more factors should be included. First, although the effects of electrolyte properties on the reaction routes have been modeled, the role of electrode surface in the route determination has not been considered yet. In addition, the product morphology is usually taken as a compact/porous film, hemisphere, or sphere in modeling, whereas the description of the unique toroid-like particles has not been reported [258]. Besides the current density, the operating conditions (e.g., oxygen pressure) can also alter the product morphology [202,203], while their influences have not been modeled. Moreover, the reported electronic and ionic conductivities of $Li_2O_2$ are not in consistency due to its complex composition and crystal structure [57], causing difficulties in assessing the limiting factor for charge transport [259].

Different modeling approaches have been used to describe the structure changes of the air electrode during discharge. A prerequisite of the modeling accuracy relies on the accurate geometrical parameters of the pristine electrode. As carbon materials have been widely used in the air electrode, their properties (e.g., specific surface area, pore distribution) are sometimes directly used in modeling [214]. However, the fabrication of the air electrode involves the use of binders, which may cover the carbon surface and

decrease significantly the actual surface area [260]. Hence, to precisely capture the structure evolution, a multiscale three-dimensional model with actual electrode reconstruction is needed. Because the two-phase boundaries also depend on the electrolyte distribution [188], the electrolyte movement has to be included in modeling the transport and reaction processes.

Compared with the models for the discharge process, the works for the charge process are quite limited. The main obstacle lies in the lack of reaction mechanism [250]. Although the effects of some aspects, including the $Li_2CO_3$ layer, the $Li_2O_2$ morphology, and the redox mediator, have been considered, more practical situations should be taken into account [202]. Meanwhile, the transport process should be coupled with the above-mentioned phenomena, such as the electrolyte movement and the electrode structure evolution. It is noted that although the irreversibility of LiOH and $Li_2CO_3$ in carbon electrodes has been demonstrated [95,236], recent studies found that these products might be decomposed with the introduction of catalysts [261-266]. For instance, $Ru/RuO_2$ can demonstrate high activity towards the oxidation of LiOH [261,262], and NiO can promote the decomposition of $Li_2CO_3$ [263,264]. The influence of catalyst and the corresponding novel mechanisms during the charge process should be further included in modeling.

In most non-aqueous Li-air batteries, diffusion dominates in the transport mechanisms. To improve the transport kinetics, some novel structures have been developed. For instance, a non-aqueous Li-air flow battery with the transport domination of convection has been reported [267-269], and the corresponding analyses have also been made [270,271]. However, to estimate the whole battery system, a comprehensive

model incorporating the energy consumption through the pump or flow field should be presented, instead of analyzing the performance improvement in the air electrode only.

## 4. Modeling of aqueous and hybrid Li-air batteries

As shown in **Figs. 2b** and **2c**, a typical aqueous/hybrid Li-air battery is made up of a lithium electrode, a porous air electrode with an aqueous electrolyte (water as the solvent), and a dense lithium ion conducting membrane as the separator. A buffer layer (for aqueous) or a non-aqueous electrolyte (for hybrid) is filled between the lithium metal and the solid membrane. At the active surfaces of the air electrode, oxygen and water electrochemically react to form hydroxide ions ($OH^-$). At the lithium metal electrode, lithium ions are electrochemically formed, passing the lithium ion conducting membrane and dissolving in the electrolyte. Lithium hydroxide monohydrate particles will nucleate when the ion concentration increases sufficiently beyond its solubility limit (Reaction IX). When analyzing the transport process, as both ORR and OER processes occur in the air electrode, the key modeling domain is still the porous air electrode. Different from non-aqueous Li-air batteries in which the air electrodes are generally flooded by the liquid electrolytes, in aqueous and hybrid Li-air batteries gaseous oxygen and liquid electrolyte may coexist in the air electrode due to the hydrophobic binders (e.g., polytetrafluoroethylene, PTFE) and carbons (e.g., Ketjen black) [118], as schematically shown in **Fig. 21** [272]. When estimating the battery voltage, due to the low ionic conductivity of the solid-state membrane and the high contact resistance [24], the modeling domain is extended to the whole battery. In Section 3, we have introduced the models for non-aqueous Li-air batteries in detail. So in this section, we will omit the duplicate process but emphasize the different electrochemical phenomena.

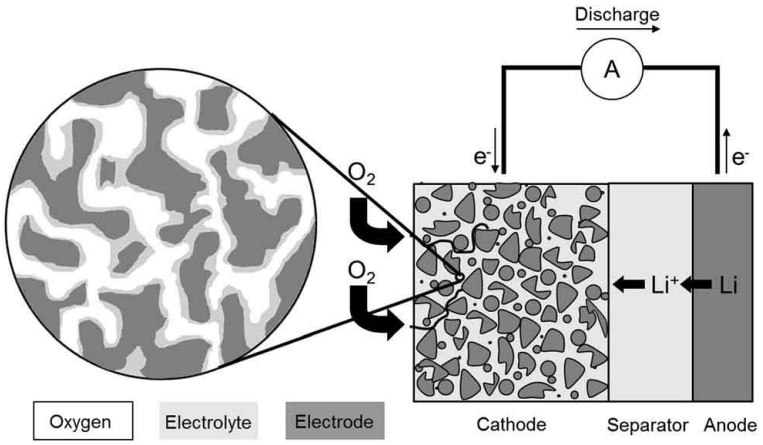


**Fig. 21** Schematic representation of an aqueous Li-air battery with an air electrode in which gaseous oxygen and liquid electrolyte coexist. Reprinted from [272] with permission of The Royal Society of Chemistry.

### 4.1 Air electrode coexisted with liquid electrolyte and gas

Different from non-aqueous Li-air batteries where most organic solvents can flood PTFE and the carbon electrode pores [273], the hydrophobic materials in the air electrode results in the coexistence of liquid electrolyte and gas in aqueous and hybrid Li-air batteries (**Fig. 21**). Hence, the description of the phase states in the air electrode is essential for the following modeling works.

Horstmann *et al.* tracked the states of the coexisting phases through macroscopic parameters and balanced their pressures with an empirical coarse-grained approach [272]. The volume fraction ($\varepsilon$) depend on the pressures ($P$) of the phase, and only liquid and gas are considered to depend on pressures. Hence, Eq. 15 represents a condition for the pressures of the gas phase $P_g$ and the liquid phase $P_e$. In the hydrophobic environment, the aqueous phase has a larger pressure than the gaseous phase, which is analogous to regular capillary depression with the empirical law as:

$$P_{cap} = P_g - P_e = -J(sa) \tag{101}$$

where $J(sa)$ is the Leverett function and $sa = \varepsilon_e(\varepsilon_e + \varepsilon_g)^{-1}$ is the saturation of the liquid phase in the free pore space. The equation of state $\varepsilon_g$ is given by the ideal gas law:

$$P_g V_g = N_g RT \tag{102}$$

and the equation of state $\varepsilon_e$ is:

$$\sum_i \frac{\partial V_e}{\partial N_i} c_i = \varepsilon_e \tag{103}$$

which follows from basic thermodynamics valid for any phase. The partial molar volume of species $i$ contains the partial molar volume $\overline{V}$ at standard pressure $P_0$ and the partial molar compressibility $\overline{\kappa}$ as:

$$\frac{\partial V_e}{\partial N_i} = \overline{V}_i + (P - P_0)\overline{\kappa}_i \tag{104}$$

In this method, details of the complex pore network containing hydrophilic/hydrophobic and microscopic/mesoscopic pores are neglected. To more precisely describe the air electrode, Grübl *et al.* applied the Lattice-Boltzmann method (LBM) to describe two-phase flow on the pore-space domain considering the wetting properties of multiple solid materials [274]. 3D reconstructions of a model electrode were first employed [20], in which the binder phase was reconstructed using a random walk algorithm on the particle surface. Simulations were then performed using unity density and viscosity ratio. The calculated capillary pressure of the simulation $\Delta P_{cap}^{LBM}$ was rescaled according to:

$$\Delta P_{cap} = \frac{\sigma_{st}}{\sigma_{st}^{LBM}} \frac{1(lu)}{\Delta x} \Delta P_{cap}^{LBM} \tag{105}$$

where $\sigma_{st}$ and $\sigma_{st}^{LBM}$ are the surface tension of the real fluids and simulation, respectively. $\Delta x$ is the one lattice unit (*lu*) and is determined by the reconstructed electrode geometry. In experimental studies, the capillary pressure/saturation characteristics are typically measured during the dynamic imbibition and drainage of the liquid phase. These two processes are possible to be mimicked by a suitable choice of initial conditions. For instance, for the simulation of the drainage process, it can be assumed that the electrolyte preferentially remains on the hydrophilic electrode surface.

The results of 3D LBM simulations are presented in **Fig. 22**. An exemplary distribution of liquid electrolyte at a saturation of 60 % in fluid mechanical equilibrium is shown in **Fig. 22a**. The final distribution can be used for the calculation of the diffusivity in the gas and liquid phase at varying saturation. From the results in **Fig. 22b**, the liquid phase diffusivity consistently increases with saturation as the tortuosity of transport pathways decreases. While at low saturations, more and shorter transport pathways are available for the gas phase. The saturation behavior of the air electrode and corresponding effective transport properties are important input parameters for further simulations.

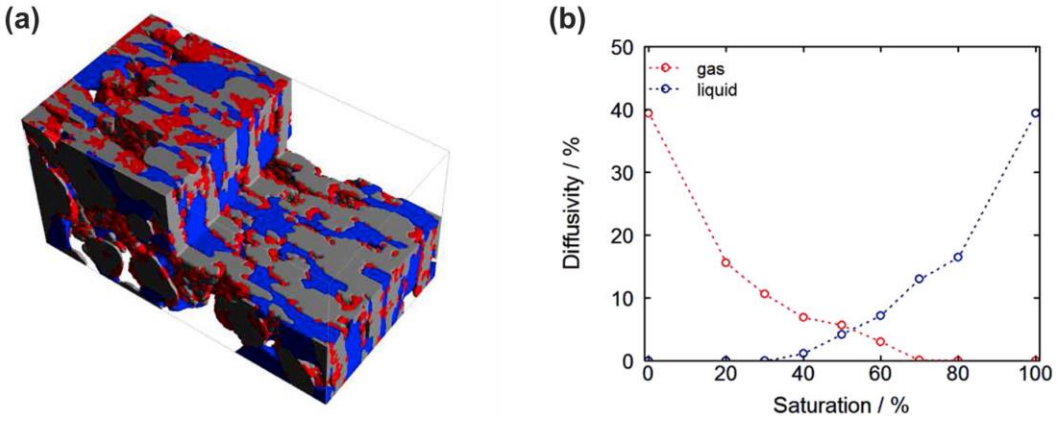

**Fig. 22** (a) Distribution of the liquid electrolyte in fluid mechanical equilibrium at a saturation of 60 %. Electrode particles are shown in grey, red areas represent the hydrophobic binder material, and the liquid electrolyte is in blue. (b) Diffusivity in the gas and liquid phase as a function of saturation. Reprinted from [274] with permission of The Electrochemical Society.

### 4.2 Species transport

Different from the scenario in non-aqueous electrolyte in which the total number of anions and cations remains constant during discharge, in aqueous electrolytes the $Li^+$ and $OH^-$ concentrations increase with the discharge process until reaching the saturation of LiOH in water ( $c_{Li^+}^{sat} = 5.17 \times 10^{-3}$ mol cm$^{-3}$). In addition, the porosity of the air electrode remains constant before saturation, but decreases afterward due to the precipitation of $LiOH \cdot H_2O$. The oxygen transport can be described through the similar approached introduced in Section 3.2, but the lithium ion transport should be carefully addressed considering these different characters.

#### 4.2.1 Before saturation

The transport of lithium ions can be basically described using the similar equations in non-aqueous electrolytes. Due to the different reaction mechanism, the relationship between $S_{Li^+}$ and $S_{O_2,e}$ is converted according to Reaction VII. It is worth noting that in aqueous electrolytes, the $Li^+$ concentration increases with the discharge process and can reach the value at saturation as high as 5.25 M. At low $Li^+$ concentrations (e.g., initial discharge stage), the dilute solution theory should be used in modeling. The current density $\boldsymbol{i}_l$ is [275]:

$$\boldsymbol{i}_l = -\kappa^{eff} \nabla \phi_l - c_{Li^+} (D_{Li^+}^{eff} - D_{OH^-}^{eff}) \nabla \ln c_{Li^+} \quad (106)$$

Here the relationship between the conductivity and ion diffusivity can be in principle established by using the Nernst-Einstein equation [174,175], different from that in Eq. 4. At higher $Li^+$ concentrations (e.g., 1.0 M), the concentrated solution theory should be applied using the similar equations as introduced in Section 3.1. Since the formed product is soluble in the electrolyte, the porosity of the cathode remains constant. However, the solvent (water) is consumed according to:

$$\frac{dm_{H_2O}}{dt} = -\frac{I_{app} M_{H_2O}}{2F} \tag{107}$$

where $M_{H_2O}$ is the molecular weight of $H_2O$, $m_{H_2O}$ is the amount of water. As a result, the concentrations of species ($Li^+$ and $OH^-$) change during the discharge process due to the electrochemical reaction and the consumption of water. Hence, the transport coefficients should be updated due to the changed concentrations.

### 4.2.2 After saturation

When reaching the saturation of LiOH in water, precipitation of $LiOH \cdot H_2O$ occurs according to Reaction IX. First, the equation for the lithium transport is slightly modified to consider the $Li^+$ and $OH^-$ consumption due to precipitation ( $Pr_{Li^+}$ ) as:

$$\frac{\partial(\varepsilon_e c_{Li^+})}{\partial t} = -\nabla \cdot \boldsymbol{N}_{Li^+} + S_{Li^+} + Pr_{Li^+} \tag{108}$$

and the concentrated solution theory should be applied. Second, because water is also consumed during the precipitation process, Eq. 107 is modified to:

$$\frac{dm_{H_2O}}{dt} = -\frac{3I_{app} M_{H_2O}}{2F} \tag{109}$$

After saturation, the discharge product $LiOH \cdot H_2O$ decreases the local volume in the air electrode. The volume fraction of electrolyte changes as:

$$\frac{\partial \varepsilon_{\mathrm{e}}}{\partial t} = -\frac{M_{\mathrm{LiOH}}}{\rho_{\mathrm{LiOH}} V_{\mathrm{tot}}} \cdot \frac{\partial n_{\mathrm{s}}}{\partial t} \tag{110}$$

where $M_{\mathrm{LiOH}}$ and $\rho_{\mathrm{LiOH}}$ are the molecular weight and mass density of deposited $LiOH{\cdot}H_2O$, respectively. $n_{\mathrm{s}}$ is the number of moles of $LiOH{\cdot}H_2O$ that have been deposited by time $t$. Hence, the transport process is tangled with the electrode structure changes as the scenario in non-aqueous Li-air batteries.

In aqueous and hybrid Li-air batteries, the solvent (water) transport is a major issue for two reasons [272]: First, water is consumed during discharge, making a constant flux of water into the GDE necessary. Second, in the GDE with the phase coexistence of gas and liquid, a pressure gradient drives water transport. The electrolyte velocity should also be considered, which is determined from Darcy's law as:

$$\boldsymbol{u}_{\mathrm{e}} = -\frac{B_{\mathrm{e}}}{\mu_{\mathrm{e}}} \nabla P_{\mathrm{e}} \tag{111}$$

and the gas velocity obeys the analogous equation as:

$$\boldsymbol{u}_{\mathrm{g}} = -\frac{B_{\mathrm{g}}}{\mu_{\mathrm{g}}} \nabla P_{\mathrm{g}} \tag{112}$$

where $B$ is the permeability of porous material, $\mu$ is the viscosity, and $P$ is the partial pressure.

### 4.3 Nucleation and growth of $LiOH{\cdot}H_2O$

In Section 3.3.2, the nucleation and growth of solid $Li_2O_2$ in non-aqueous Li-air batteries have been modeled to determine the resultant surface coverage [206]. In contrast to the situation that the solid $Li_2O_2$ deposits in the air electrode from the beginning, in aqueous and hybrid Li-air batteries, when the lithium ion concentration increases sufficiently beyond the solubility limit, small stable crystal clusters nucleate and start to

grow (Reaction IX). The nucleation of seed crystals and the subsequent growth of $LiOH \cdot H_2O$ were modeled by Horstmann *et al.* using the classical theory of nucleation and growth [272]. The reaction enthalpy of formation of a single crystal nucleus of size *n* consists of a bulk and a surface term:

$$\Delta G = \Delta G_{\text{bulk}} + \Delta G_{\text{surface}} = -n2kT \ln Sr + A(n)\gamma_{\text{s}} \tag{113}$$

where $A(n)$ is the surface area of $LiOH \cdot H_2O$ nucleus, $\gamma_{\text{s}}$ is the macroscopic surface energy and the factor of 2 arises for a binary salt. The supersaturation ratio $Sr = c_{\text{Li}^+} / c_{\text{Li}^+}^{\text{sat}}$ is the driving force for nucleation. For larger nucleus sizes the bulk energy is increasingly negative, whereas the surface energy is increasingly positive. To grow in a stable way, crystal clusters must exceed a critical size. In the case of heterogeneous disc-shaped nucleation, the critical formation energy is expressed as [276]:

$$\Delta G_{\text{crit}} = \frac{\gamma_s^2 L_{\text{LiOH}\cdot\text{H}_2\text{O}}^4}{2kT \ln Sr} \tag{114}$$

where $L_{\text{LiOH}\cdot\text{H}_2\text{O}}$ is the length scale of $LiOH \cdot H_2O$. The rate of nucleation of critical nuclei is estimated as [277]:

$$\dot{N} = \frac{D_{\text{sd}}}{L_{\text{LiOH}}^2} Z N_{\text{s}} \exp\left(-\frac{\Delta G_{\text{crit}}}{kT}\right) \tag{115}$$

where $D_{\text{sd}}$ is the self-diffusion coefficient of $Li^+$, $L_{\text{LiOH}}$ is the length scale of LiOH, $Z$ is the Zeldovich factor to express the fact that a critical nucleus can disintegrate again, and $N_{\text{s}}$ is the number of sites on which nucleation can occur.

For crystal growth, the linear growth is the simplest case, which is predicted by the bulk diffusion model at large supersaturation ratios ($Sr > 10^{-5}$) [277]. The reaction rate for this growth process is:

$$\dot{S}_{\mathrm{cg}} = \frac{D_{\mathrm{sd}}}{\delta_{\mathrm{dl}}}(c_{\mathrm{Li^+}} - c_{\mathrm{Li^+}}^{\mathrm{sat}}) \tag{116}$$

where $\delta_{\mathrm{dl}}$ is the diffusion layer thickness.

When applying Eqs. 115 and 116 in aqueous and hybrid Li-air batteries, two cases were considered in Horstmann's work [272]. The first one is that nucleation occurs on the surfaces of the air electrode (**Fig. 21**). The disc-shaped heterogeneous nucleation was assumed to be valid for nucleation on crystal material itself. The area supporting the nucleus evolves as:

$$\frac{\partial a}{\partial t} = \pi r_{\mathrm{crit}}^2 \dot{N}(N_{\mathrm{s}}) \tag{117}$$

where $a$ is the surface area per unit electrode volume, $r_{\mathrm{crit}}$ is the critical radius, and $N_{\mathrm{s}} = a^0 / L_{\mathrm{LiOH\cdot H_2O}}^2$ . LiOH·H2O can subsequently crystallize on top of these discs according to Eq. 116, where a constant diffusion layer thickness $\delta_{\mathrm{dl}}$ is assumed to be determined by the pore structure. The crystal growth is described with a single volume fraction:

$$\frac{\partial \varepsilon_{\mathrm{cg}}}{\partial t} = a\dot{S}_{\mathrm{cg}} V_{\mathrm{LiOH\cdot H_2O}}^{\mathrm{m}} \tag{118}$$

Through this approach, the nucleation and growth of column-shaped precipitations in the air electrode can be simulated.

The other case is that a reservoir of pure electrolyte is applied between the solid membrane and the air electrode, as schematically shown in **Fig. 2b**. In this liquid reservoir, the crystal nuclei sediment due to gravity and form a reservoir of precipitations at the bottom [278]. Under this condition, crystal nuclei of different sizes can coexist [279], and the size distribution of spherical crystal nuclei was described as:

$$N(r) = f(r)\mathrm{d}r \tag{119}$$

with radii $r$ via the equation:

$$\frac{\partial f(r)}{\partial t} = \dot{N}\,\mathrm{d}r_0^{-1}\delta_{r_0} - f\tau^{-1} - \frac{\partial}{\partial r}\left(f\frac{\mathrm{d}r}{\mathrm{d}t}\right) \tag{120}$$

The first term describes nucleation of crystals where the nucleation rate is $\dot{N}$ with a constant $N_s$ and the first discretization compartment contains radii from 0 to $\mathrm{d}r_0$. The second term describes the sedimentation due to gravity as:

$$\tau(r) = \frac{h_{\mathrm{bat}}\varepsilon_{\mathrm{e}}}{v_{\mathrm{s}}(r)} \tag{121}$$

where $h_{\mathrm{bat}}$ is the height of the battery and $v_{\mathrm{s}}(r)$ is the sedimentation velocity from Stoke's law. The last term represents crystal growth with radial growth rate [280]:

$$\frac{\mathrm{d}r}{\mathrm{d}t} = \dot{S}_{\mathrm{cg}}(\delta_{\mathrm{dl}})V^{\mathrm{m}}_{\mathrm{LiOH\cdot H_2O}} \tag{122}$$

where the diffusion layer thickness $\delta_{\mathrm{dl}}$ is determined by sedimentation. By integrating the crystal size distribution (Eq. 119), the volume fraction of sedimenting crystals is:

$$\frac{\partial \varepsilon_{\mathrm{cg}}}{\partial t} = V^{\mathrm{m}}_{\mathrm{LiOH\cdot H_2O}} N_a^{-1} \int \frac{4}{3}\pi r^3 f\mathrm{d}r \tag{123}$$

This approach expands the precipitation area to the whole region of the battery with the aqueous electrolyte. Actually, this phenomenon was also observed in non-aqueous Li-air batteries in which solid $Li_2O_2$ particles were coated on the glass fiber separator that saturated with the liquid electrolyte [204]. Hence, although in non-aqueous and aqueous systems the solid products are formed from different mechanisms, they may share some similar nucleation and growth characters. Developing a general approach to describe these processes, therefore, is in great need for future modeling work.

### 4.4 Performance estimation

#### 4.4.1 Power density

Although the discharge process of aqueous and hybrid Li-air batteries has two regimes and may introduce complex transport issues as those in non-aqueous Li-air batteries, the unique feature of the aqueous-based batteries is that the air electrode structure does not change in the first regime. Hence, if the battery structure is well designed with refreshing the electrolyte [122], the second discharge regime may be avoided so that a stable power can be delivered. Andrei *et al.* developed a model to predict the maximum theoretical power density [281] of aqueous-based Li-air batteries, from which the battery voltage ($V_{bat}$) was written as:

$$V_{bat} = E^0 - \eta_a - \eta_c - R_{Sep} I_{app} - R_0 I_{app} \tag{124}$$

where $R_{Sep}$ is the resistance of the separator including the separator-anode and separator-cathode interfaces, $R_0$ is the combined resistance of the electrolyte, electrons, and contacts.

The overpotential at the anode was obtained through setting the charge transfer coefficient $\beta$ as 0.5 to obtain:

$$\eta_a = \frac{2RT}{F} \sinh^{-1}\left(\frac{I_{app}}{2S_{cs} i_a}\right) \tag{125}$$

where $\sinh^{-1}$ is the inverse sinh function. To obtain a closed-form solution for the cathode overpotential, the cathode reaction is assumed to be limited by oxygen diffusion due to the slow oxygen diffusion coefficient. Considering the steady-state one-dimensional mass transfer along the cathode thickness ($L_{Cat}$) and setting the charge transfer coefficient as 0.5, the overpotential at the cathode was obtained as:

$$\eta_{\mathrm{c}} = \frac{2RT}{nF}\sinh^{-1}\left(\frac{D_{\mathrm{O_2,e}}^{\mathrm{eff}}}{2\lambda^2 k_{\mathrm{c}} a}\right) \tag{126}$$

where $\lambda$ is the oxygen diffusion length is related to the applied current:

$$I_{\mathrm{app}} = \frac{nS_{\mathrm{cs}}FD_{\mathrm{O_2,e}}^{\mathrm{eff}}k_{\mathrm{f}}\,p_{\mathrm{O_2}}}{\lambda k_{\mathrm{f}} H\coth(L_{\mathrm{Cat}}/\lambda) + D_{\mathrm{O_2,e}}^{\mathrm{eff}}} \tag{127}$$

where $p_{\mathrm{O_2}}$ is the outside partial pressure of the oxygen.

The resistance of the separator can be written as the sum of the bulk resistance of the separator ($R_{\mathrm{bulk}}$) and the resistances of the separator/anode ($R_{\mathrm{SA}}$) and separator/cathode ($R_{\mathrm{SC}}$) interfaces:

$$R_{\mathrm{Sep}} = \frac{R_{\mathrm{bulk}} + R_{\mathrm{SA}} + R_{\mathrm{SC}}}{S_{\mathrm{cs}}} \tag{128}$$

The validation of this model is made by comparing the theoretical predictions of the voltage and power of the battery with experimental data [115], which shows good agreement (**Fig. 23a**). Because the oxygen diffusion coefficient is expected to become a limiting factor for achieving high power density, the maximum power density as a function of the oxygen diffusion coefficient and partial pressure can also be analyzed, as presented in **Fig. 23b**. A ten-fold increase in $p_{\mathrm{O_2}}$ results in a slightly better improvement on power density than a ten-fold increase in $D_{\mathrm{O_2,e}}$. This result indicates that to achieve higher power densities, decreasing the internal ohmic losses, especially those caused by the solid-state electrolyte membrane, is needed.

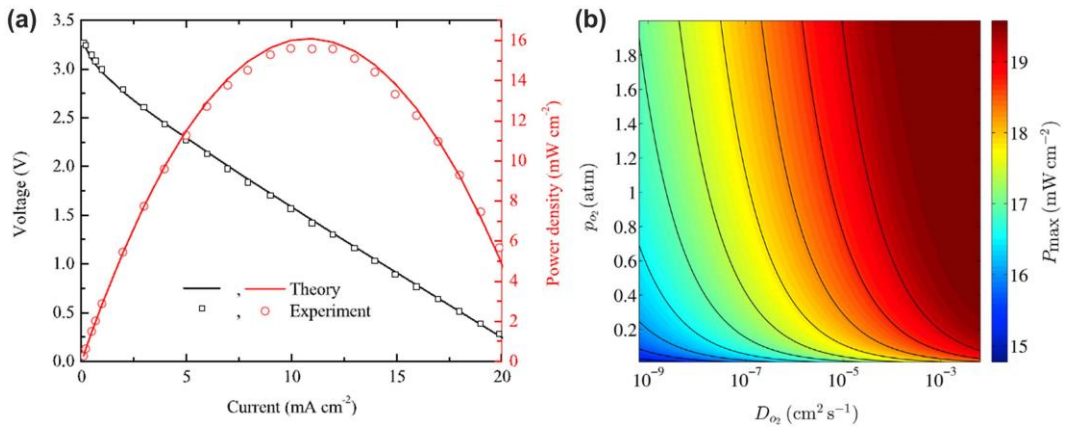


**Fig. 23** (a) Comparison between experimental data and analytical predictions. (b) Contour plot of the maximum power density as a function of the oxygen partial pressure and diffusion coefficient. Adapted from [281] with permission of Elsevier.

### 4.4.2 State of charge

Although the first discharge regime (dissolved LiOH discharge product) can yield a high power density, the second discharge regime (solid $LiOH{\cdot}H_2O$ discharge product) can yield a high specific energy density. To take this two-stage behavior into account, Grübl *et al.* defined the state of charge (SOC) in the first regime as the concentration of dissolved LiOH relative to its solubility limit ($c_{Li^+}^{sat}$) as [274]:

$$SOC_l = 1 - \frac{c_{Li^+}}{c_{Li^+}^{sat}} \tag{129}$$

In the second regime, $SOC_s$ was defined as the ratio of volume fraction of solid $LiOH{\cdot}H_2O$ and the total available pore volume $\varepsilon$ as:

$$SOC_s = 1 - \frac{\varepsilon_{LiOH{\cdot}H_2O}}{\varepsilon} \tag{130}$$

The global *SOC* was then defined as the sum of both weighted by their maximum capacities $C_l$ and $C_s$ related to the total capacity $C_{total}$ ($C_{total} = C_l + C_s$):

$$SOC = SOC_{\mathrm{l}} \frac{C_{\mathrm{l}}}{C_{\mathrm{total}}} + SOC_{\mathrm{s}} \frac{C_{\mathrm{s}}}{C_{\mathrm{total}}} \tag{131}$$

Using this definition, the performance of an aqueous Li-air battery in a virtual electric vehicle can be further estimated in a system level.

**4.5 Temperature effects**

As shown in **Fig. 24a**, the solubility of LiOH in water increases apparently with temperature, indicating that a higher operating temperature can lead to a longer first discharge regime. In the second regime, the surface energy of $LiOH{\cdot}H_2O$ was taken from the theoretical prediction as [282]:

$$\gamma_{\mathrm{s}} = -0.414 \frac{kT}{a_{\mathrm{LiOH{\cdot}H_2O}}} \ln(c^{\mathrm{sat}}_{\mathrm{Li^+}} V^{\mathrm{m}}_{\mathrm{LiOH{\cdot}H_2O}}) \tag{132}$$

The solubility of oxygen in alkaline water depends on the temperature and the salt concentration, which is referred to as salting-out, as shown in **Fig. 24b**. If $LiOH{\cdot}H_2O$ is added to the solution, the solubility of oxygen is reduced and gaseous molecular oxygen evolves. This phenomenon was described via the empirical Setchenov relation as [283]:

$$\frac{\mu_{\mathrm{O_2}} - \mu^0_{\mathrm{O_2}}}{RT} = \ln(\frac{c_{\mathrm{O_2}}}{\mathrm{mol \cdot L^{-1}}}) + k_{\mathrm{sca}} c_{\mathrm{Li^+}} \tag{133}$$

where $\mu_{\mathrm{O_2}}$ is the potential of oxygen and $k_{\mathrm{sca}}$ is the salting-out parameter.

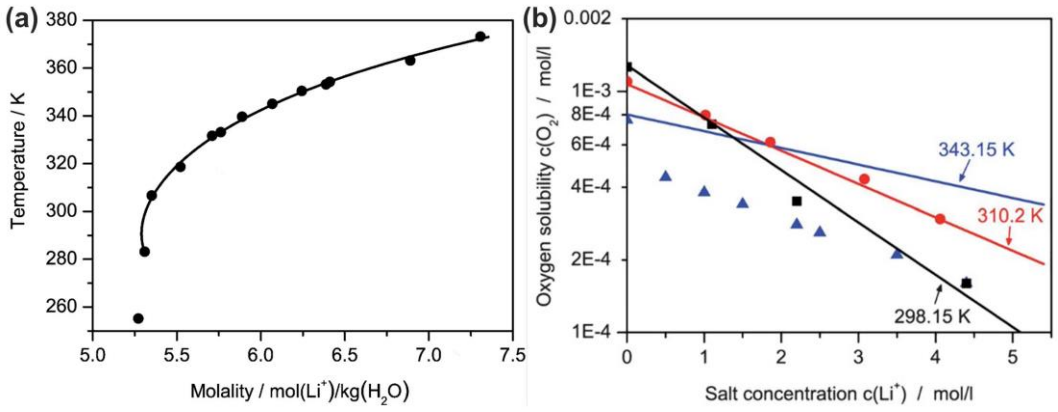

**Fig. 24** Parameters change with temperature: (a) Solubility of lithium hydroxide in aqueous solution for various temperatures. (b) Oxygen solubility at various salt concentrations and temperatures. Adapted from [272] with permission of The Royal Society of Chemistry.

Besides the solubility of oxygen, other properties such as the electrolyte density, the diffusion coefficient, and the ionic conductivity all change with temperature and can be described through empirical equations or data fitting [272]. In addition to considering the transport and kinetics changes in the air electrode, an important feature for aqueous and hybrid Li-air batteries is that temperature can tremendously affect the ionic conductivity of the solid-state lithium ion conducting membrane [284]. Thus, the performance at high temperatures, including the discharge capacity, cell voltage, and the power density, should be carefully addressed through taking this into account [285].

### 4.6 Critical challenges for aqueous systems

As little attention has been paid to aqueous and hybrid Li-air batteries, the corresponding modeling works are also limited, as listed in **Table 2**. Due to the two regimes during discharge, aqueous and hybrid Li-air batteries share some similar features of alkaline fuel cells and non-aqueous Li-air batteries, so that some well-developed theories and models can be adopted. Even so, some unique aspects are worth attention, and the critical challenges are shown below.

**Table 2** Summary of modeling works of aqueous and hybrid Li-air batteries

| Published year | $Li^+$ transport | $O_2$ transport | LiOH dissolution | $LiOH \cdot H_2O$ precipitation | Transport through $LiOH \cdot H_2O$ | Reaction kinetics | Electrode structure | Power/SOC estimation | Battery type | Ref. |
|---|---|---|---|---|---|---|---|---|---|---|
| 2012 | ✓ | ✓ | ✓ | ✓ | ✓ | ✓ | ✓ | | Hybrid | [275] |
| 2013 | ✓ | ✓ | ✓ | ✓ | | ✓ | ✓ | | Aqueous | [272] |
| 2014 | ✓ | ✓ | ✓ | ✓ | | ✓ | ✓ | ✓ | Aqueous | [274] |

| | | | | | | | | | |
|---|---|---|---|---|---|---|---|---|---|
| | ✓ | ✓ | ✓ | ✓ | | ✓ | ✓ | | Aqueous [286] |
| 2015 | | ✓ | ✓ | | | ✓ | | ✓ | Hybrid [281] |
| | ✓ | ✓ | ✓ | ✓ | | ✓ | ✓ | | Aqueous [287] |

First, phase states of the air electrode should be carefully treated. Attributed to the hydrophobic materials applied in the air electrode, both gas and liquid electrolyte coexist in the electrode. Various approaches have been applied to describe the phase states, while more precise results are in the great demand for further analyses. Different from the wetted electrode in non-aqueous Li-air batteries, the electrolyte solvent (water) in aqueous and hybrid Li-air batteries also participates in electrochemical reactions. In the first discharge regime, although the electrode structure does not change, the total amount of liquid electrolyte solvent decreases due to the consumption of water. In the second regime, both the electrochemical consumption and the solid product precipitation change the distribution of the electrolyte inside the electrode. The electrolyte movement not only introduces convection into the transport mechanisms, but also continuously changes the phase states inside the air electrode, resulting in a complex moving boundary problem.

Second, the transport and reaction kinetics during discharge should be well addressed. In non-aqueous Li-air batteries, atmospheric oxygen molecules dissolve first into the non-aqueous electrolyte, and then are reduced at the two-phase boundaries. While in aqueous and hybrid Li-air batteries, the coexisted liquid electrolyte and gas enable the electrochemical reactions to occur at the triple-phase boundaries among gaseous oxygen (gas), electrolyte (liquid), and active material (solid) [93]. Although in some reported modeling works only dissolved oxygen was considered [275], a detailed description of the transport and reaction processes among different phases is essential for a practical air electrode.

Third, the electrolyte components are complex in practice. In modeling works, the electrolyte is usually taken as a binary solution (LiOH solution). To improve the theoretical specific capacity and energy density, acid solutions such as HCl and $HClO_3$ with a high solubility of discharge products may be applied [122]. In addition, as the aqueous electrolytes with high or low pH can cause stability issues of the solid-state electrolyte membrane [114,288], some buffer additives are used in the aqueous electrolytes [289,290]. As a result, the electrolyte is no longer a binary solution but with complex anions and cations.

Fourth, the solid discharge product, $LiOH{\cdot}H_2O$, receives little attention. In the second discharge regime, the precipitation of $LiOH{\cdot}H_2O$ occurs, which is similar to the formation of solid $Li_2O_2$ in non-aqueous Li-air batteries. In modeling works, the nucleation and growth of $LiOH{\cdot}H_2O$ have been considered [272], and the corresponding influence on the electrode structure has also been analyzed [275]. However, the morphology of the precipitation is usually taken as a disc or a sphere, while the actual formation of more complex morphologies, along with the corresponding influences on the electrode microstructure (e.g., pore size, shape, and distribution) and the transport kinetics, have been rarely considered in modeling. Besides, the relationship between nucleation and surface conditions (e.g., with or without catalysts) has few been investigated [286]. To give a better description of this phenomenon, more experimental works with advanced characterization techniques are required.

Fifth, the charge process has not been modeled yet. Although the charge performance of aqueous and hybrid Li-air batteries has been investigated experimentally [124,291], no relevant modeling works have been conducted. To describe the charge

process, a lot of aspects should be considered, including the catalytic activities, transport kinetics, etc. Moreover, the charge process started from the solid $LiOH \cdot H_2O$ involves its dissolution with the formation of water, causing another moving boundary issues and aggravating the modeling complexity.

Last but not least, analyses on novel aqueous and hybrid Li-air battery systems are important. To facilitate the transport kinetics, a new Li-air flow battery system has been proposed and experimentally demonstrated [292]. Model is a powerful tool in evaluating the feasibility of different battery structures and concepts [287]. However, it is worth noting to evaluate the feasibility of a new battery structure, not only the performance improvements but also the extra energy consumptions due to the introduction of new components (e.g., the energy consumption of the pump for a flow system) should be considered in a system level [274].

## 5. Summary and outlook

Li-air batteries have potential to be the next generation of power sources for many emerging technologies due largely to the high theoretical energy density. To commercialize this promising technology, tremendous efforts have been devoted to overcoming the technical hurdles through experimental and computational approaches. In this paper, we have reviewed the latest developments in modeling and simulation of different types of Li-air batteries. Unlike previous reviews that focused mainly on the continuum models, we center on the modeling and simulation of the detailed physical, chemical, and electrochemical phenomena associated with the discharge and charge processes. We have outlined the modeling descriptions of various transport and reaction processes in non-aqueous Li-air batteries, including the lithium ion and oxygen transport

in the porous air electrode, the formation mechanism, morphology, and transport of the solid product $Li_2O_2$, the kinetics of electrode reactions, the evolution of electrode structure, the distribution of active site, the side reactions, the volume change phenomena, and the charge process with considering the effects of $Li_2CO_3$, $Li_2O_2$ morphology, and redox mediator. Undoubtedly, substantial challenges still remain for modeling non-aqueous Li-air batteries as we summarized in Section 3.10. The modeling works of aqueous and hybrid Li-air batteries, especially the phenomena that different from the non-aqueous ones, have also been reviewed. The unique aspects that worth attention and the critical challenges are also discussed in Section 4.6. To develop more powerful predictive models that can be used for rational design of high-performance Li-air batteries, attention should be paid particularly to the following areas:

First, a better understanding of the reaction kinetics on the surface of porous air electrodes is needed. For non-aqueous Li-air batteries, although detailed descriptions have been proposed for different reaction steps and routes during discharge (Section 3.3.1), a simplified overall reaction has always been used (Section 3.4) when considered together with the transport processes, which may result in inaccurate results. During charge, the related modeling descriptions are quite limited due to the lack of detailed reaction mechanisms. Similar scenarios exist in modeling aqueous and hybrid Li-air batteries, with less detailed reaction steps being taken into account. For solid-state Li-air batteries, unfortunately, the related modeling and simulation are not yet reported in the literature, due largely to the lack of reaction mechanisms, especially the formation and growth mechanism of the solid product $Li_2O_2$ in an all-solid-state battery system. In addition, most reported modeling works have only considered the ORR and OER

processes. When operating in ambient air, the other gases and contaminants encountered in ambient air may participate in the reactions and lead to side products; their corresponding influences on the battery performance should be further investigated.

Second, the reliability and accuracy of the input parameters are essential for predictive modeling and simulation. The values of many parameters may critically affect the predicted performance of Li-air batteries, including the electrolyte properties (e.g., oxygen solubility, lithium ion conductivity), the electrode geometries (e.g., specific surface area, porosity, pore size distribution), and the reaction kinetics (e.g. reaction rate constant). However, some of these parameters are often unavailable or incomplete, limiting the accuracy in prediction and evaluation of battery performance. Efforts should be devoted to advancing characterization and measurement techniques in order to provide accurate values for these important parameters.

Third, a comprehensive modeling of the whole battery system is required. Most reported models focus mainly on the reactions occur in the air electrode. To assess the performance of the whole battery system, the behavior of the lithium electrode should also be included, considering the lithium dissolution and deposition processes with possible dendrite formation and growth. In addition, temperature effects are usually ignored when the current densities are relatively low. However, for Li-air batteries or cell stacks of large power, thermal management could become critical to battery performance, such as start-up in cold areas. Thus, thermal transport and temperature distribution may have to be taken into consideration. Moreover, the mass flow (e.g., air) arrangement may also affect battery performance. A comprehensive model considering all battery

components and the effects of operating conditions (e.g., current, temperature, air flow) is required in the performance assessment and optimization.

Fourth, multiscale and multiphase modeling, in which the physicochemical processes occur in different scales and different phases can be solved simultaneously, is in great need. With the development of modeling technology, the transport and electrochemical processes from micro to macro scale and the detailed phase transition in Li-air batteries can be taken into consideration. With the help of experimental validation, predictive models can be used to optimize a specific design and tune the operating conditions for improved performance.

These advances will not only accelerate the development of Li-air battery technologies, but also provide useful guidance for better designs of other electrochemical energy systems such as lithium-sulfur batteries and sodium-air batteries.

**Acknowledgement**

M. NI thanks the funding support from The Hong Kong Polytechnic University (G-YBJN and G-YW2D), the Environment Conservation Fund (ECF 54/2015) and a fund from RISUD (1-ZVEA).

**Nomenclature**

| | |
|---|---|
| $A$ | Total active area of the air electrode ($m^3$) |
| $a$ | Active surface area per unit electrode volume ($m^2\ m^{-3}$) |
| $B$ | Permeability of porous material ($m^2$) |
| $b$ | Tafel slope ($V\ dec^{-1}$) |
| $C_{emp}$ | Empirical constant |
| $c$ | Concentration ($mol\ m^{-3}$) |
| $D$ | Diffusion coefficient ($m^2\ s^{-1}$) |
| $d$ | Distance (m) |
| $E$ | Voltage (V) |
| $e$ | Electron charge |

| | |
|---|---|
| $F$ | Faraday constant (96,485 C $mol^{-1}$) |
| $f_{\pm}$ | Activity coefficient of a lithium salt |
| $G$ | Gibbs free energy (J $mol^{-1}$) |
| $H$ | Henry's constant |
| $h$ | Height of the $Li_2O_2$ crystal (m) |
| $I$ | Current (A) |
| $i$ | Current density (A $m^{-2}$) |
| $J$ | Nucleation rate |
| $j$ | Local transfer current density (A $m^{-2}$) |
| $K_{+0}$ | Frequency factor |
| $k$ | Rate constant |
| $k_B$ | Boltzmann constant ($1.38\times10^{-23}$ J $K^{-1}$) |
| L | Length (m) |
| $M$ | molecular weight |
| $N_0$ | Surface concentration of active sites |
| $\boldsymbol{N}$ | Molar flux |
| $n$ | Number of electrons transferred |
| $P$ | Partial pressure of species (Pa) |
| $P_r$ | Precipitation rate |
| $p$ | Geometrical factor |
| $R$ | Universal gas constant (8.314 J $mol^{-1}$ $K^{-1}$) |
| $R_f$ | Roughness factor |
| $r$ | Radius (nm) |
| $S$ | Reaction rate (mol $m^{-3}$ $s^{-1}$); Cross section area ($m^2$) |
| $Sr$ | Supersaturation ratio |
| $s$ | Stoichiometric coefficient |
| $T$ | temperature (K) |
| $t$ | Time (s) |
| $t_+$ | Transference number of cation |
| $U_0$ | Energy barrier to attachment |
| $\boldsymbol{u}$ | Velocity (m $s^{-1}$) |
| $V$ | Volume ($m^3$) |
| $v$ | Boundary velocity (m $s^{-1}$) |
| $w$ | Dimensionless factor of the three constant |
| $z_+$ | Charge number |

***Greek***

| | |
|---|---|
| $\alpha$ | Charge transfer coefficient |
| $\alpha_v$ | Velocity of the grid points (m $s^{-1}$) |
| $\beta$ | Charge transfer symmetry factor |
| $\Gamma$ | Maximum surface-site concentration |
| $\gamma$ | Cathode geometry parameter |
| $\gamma_{\ddagger}$ | Activity coefficient of the transition state |
| $\delta$ | Thickness (m) |
| $\varepsilon$ | Porosity or volume fraction |
| $\varepsilon_{dp}$ | Dielectric permittivity |
| $\zeta$ | Volume ratio of secondary to primary pores |
| $\eta$ | Overpotential (V) |
| $\theta$ | Fraction of covered surface |
| $\kappa$ | Ionic conductivity (S $m^{-1}$) |
| $\lambda$ | Oxygen diffusion length (m) |
| $\mu$ | Potential (V); Viscosity (Pa·s) |
| $\nu$ | Numbers of anion/cation |
| $\xi$ | Moving coordinate |
| $\xi_{esc}$ | Escape probability factor |
| $\rho$ | Density (kg $m^{-3}$) |
| $\sigma$ | Electrical conductivity (S $m^{-1}$); Surface tension (N $m^{-1}$) |
| $\Phi$ | Electrostatic potential in the electrolyte phase (V) |
| $\phi$ | Electric potential (V) |
| $\chi$ | Escape function |
| $\psi$ | Electrode potential (V) |
| $\omega$ | Molar volume (L $mol^{-1}$) |

***Superscripts and subscripts***

| | |
|---|---|
| + | anion |
| − | cation |
| 0 | equilibrium or initial value |
| app | applied value |
| bat | battery |
| cap | capillary |
| cg | crystal growth |
| crit | critical value |
| d | dimensionless |
| dl | diffusion layer |

| | |
|---|---|
| e | electrolyte |
| eff | effective value |
| eq | Equilibrium state |
| g | gas |
| K | Knudsen diffusion |
| l | liquid |
| s | solid |
| sat | saturation value |
| sd | self-diffusion |
| sur | surface |

**References**


[1] Wagner FT, Lakshmanan B, Mathias MF. Electrochemistry and the Future of the Automobile. J Phys Chem Lett 2010;1:2204-19.

[2] Cairns EJ, Albertus P. Batteries for Electric and Hybrid-Electric Vehicles. Annu Rev Chem Biomol 2010;1:299-320.

[3] Wang Z, Xu D, Xu J, Zhang X. Oxygen electrocatalysts in metal–air batteries: from aqueous to nonaqueous electrolytes. Chem Soc Rev 2014;43:7746-86.

[4] Zu C, Li H. Thermodynamic analysis on energy densities of batteries. Energy Environ Sci. 2011;4:2614-24.

[5] Lee J, Kim ST, Cao R, Choi N, Liu M, Lee KT et al. Metal-Air Batteries with High Energy Density: Li-Air versus Zn-Air. Adv Energy Mater 2011;1:34-50.

[6] Girishkumar G, McCloskey B, Luntz AC, Swanson S, Wilcke W. Lithium-Air Battery: Promise and Challenges. J Phys Chem Lett 2010;1:2193-203.

[7] Abraham K, Jiang Z. A polymer electrolyte-based rechargeable lithium/oxygen battery. J Electrochem Soc 1996;143:1-5.

[8] Bruce PG, Freunberger SA, Hardwick LJ, Tarascon J. Li-$O_2$ and Li-S batteries with high energy storage. Nat Mater 2012;11:19-29.

[9] Christensen J, Albertus P, Sanchez-Carrera RS, Lohmann T, Kozinsky B, Liedtke R et al. A Critical Review of Li/Air Batteries. J Electrochem Soc 2012;159:R1-R30.

[10] Capsoni D, Bini M, Ferrari S, Quartarone E, Mustarelli P. Recent advances in the development of Li-air batteries. J Power Sources 2012;220:253-63.

[11] Lu Y, Gallant BM, Kwabi DG, Harding JR, Mitchell RR, Whittingham MS et al. Lithium-oxygen batteries: bridging mechanistic understanding and battery performance. Energy Environ Sci 2013;6:750-68.

[12] Garcia-Araez N, Novak P. Critical aspects in the development of lithium-air batteries. J Solid State Electrochem 2013;17:1793-807.

[13] Bhatt MD, Geaney H, Nolan M, O'Dwyer C. Key scientific challenges in current rechargeable non-aqueous Li-$O_2$ batteries: experiment and theory. Phys Chem Chem Phys 2014;16:12093-130.

[14] Padbury R, Zhang X. Lithium–oxygen batteries—Limiting factors that affect performance. J Power Sources 2011;196:4436-44.

[15] Grew KN, Chiu WK. A review of modeling and simulation techniques across the length scales for the solid oxide fuel cell. J Power Sources 2012;199:1-13.

[16] Meng YS, Arroyo-de Dompablo ME. First principles computational materials design for energy storage materials in lithium ion batteries. Energy Environ Sci 2009;2:589-609.

[17] Cramer CJ. Essentials of computational chemistry: theories and models. John Wiley & Sons, 2013.

[18] Sanchez JMC, Danner T, Gross J. Grand canonical Monte Carlo simulations of vapor-liquid equilibria using a bias potential from an analytic equation of state. J Chem Phys 2013;138:234106.

[19] Chen S, Doolen GD. Lattice Boltzmann method for fluid flows. Annu Rev Fluid Mech 1998;30:329-64.

[20] Danner T. Modeling and experimental investigation of transport processes in the porous cathode of aqueous Li-air batteries. Doctoral dissertation, Universität Stuttgart 2015.

[21] Shi S, Gao J, Liu Y, Zhao Y, Wu Q, Ju W et al. Multi-scale computation methods: Their applications in lithium-ion battery research and development. Chinese Physics B 2015;25:018212.

[22] Ramadesigan V, Northrop PW, De S, Santhanagopalan S, Braatz RD, Subramanian VR. Modeling and simulation of lithium-ion batteries from a systems engineering perspective. J Electrochem Soc 2012;159:R31-45.

[23] Franco AA. Multiscale modelling and numerical simulation of rechargeable lithium ion batteries: concepts, methods and challenges. RSC Adv 2013;3:13027-58.

[24] Sun Y. Lithium ion conducting membranes for lithium-air batteries. Nano Energy 2013;2:801-16.

[25] Balaish M, Kraytsberg A, Ein-Eli Y. A critical review on lithium-air battery electrolytes. Phys Chem Chem Phys 2014;16:2801-22.

[26] Younesi R, Veith GM, Johansson P, Edstrom K, Vegge T. Lithium salts for advanced lithium batteries: Li-metal, Li-$O_2$, and Li-S. Energy Environ Sci 2015;8:1905-22.

[27] Li Q, Cao R, Cho J, Wu G. Nanostructured carbon-based cathode catalysts for nonaqueous lithium-oxygen batteries. Phys Chem Chem Phys 2014;16:13568-82.

[28] Kim H, Lim H, Kim J, Kang K. Graphene for advanced Li/S and Li/air batteries. J Mater Chem A 2014;2:33-47.

[29] Mahmood N, Zhang C, Yin H, Hou Y. Graphene-based nanocomposites for energy storage and conversion in lithium batteries, supercapacitors and fuel cells. J Mater Chem A 2014;2:15-32.

[30] Hardwick LJ, Bruce PG. The pursuit of rechargeable non-aqueous lithium-oxygen battery cathodes. Curr Opin Solid State Mater Sci 2012;16:178-85.

[31] Wen Z, Shen C, Lu Y. Air Electrode for the Lithium-Air Batteries: Materials and Structure Designs. ChemPlusChem 2015;80:270-87.

[32] Ma Z, Yuan X, Li L, Ma Z, Wilkinson DP, Zhang L et al. A review of cathode materials and structures for rechargeable lithium-air batteries. Energy Environ Sci 2015;8:2144-98.

[33] Chang Z, Xu J, Liu Q, Li L, Zhang X. Recent Progress on Stability Enhancement for Cathode in Rechargeable Non-Aqueous Lithium-Oxygen Battery. Adv Energy Mater 2015;5:1500633.

[34] McCloskey BD, Burke CM, Nichols JE, Renfrew SE. Mechanistic insights for the development of Li–$O_2$ battery materials: addressing $Li_2O_2$ conductivity limitations and electrolyte and cathode instabilities. Chem Commun 2015;51:12701-15.

[35] Aurbach D, McCloskey BD, Nazar LF, Bruce PG. Advances in understanding mechanisms underpinning lithium–air batteries. Nat Energy 2016;1:16128.

[36] Franco AA, Xue K. Carbon-based electrodes for lithium air batteries: scientific and technological challenges from a modeling perspective. ECS J Solid State Sc 2013;2:M3084-100.

[37] Yuan J, Yu J, Sundén B. Review on mechanisms and continuum models of multi-phase transport phenomena in porous structures of non-aqueous Li-Air batteries. J Power Sources 2015;278:352-69.

[38] Li X, Huang J, Faghri A. A critical review of macroscopic modeling studies on Li $O_2$ and Li–air batteries using organic electrolyte: Challenges and opportunities. J Power Sources 2016;332:420-46.

[39] Wu HY, Zhang H, Cheng XL, Cai LC. The thermodynamic properties of lithium peroxide, $Li_2O_2$. Phys Lett A 2006;360:352-6.

[40] Mo Y, Ong SP, Ceder G. First-principles study of the oxygen evolution reaction of lithium peroxide in the lithium-air battery. Phys Rev B 2011;84:205446.

[41] Radin MD, Rodriguez JF, Tian F, Siegel DJ. Lithium Peroxide Surfaces Are Metallic, While Lithium Oxide Surfaces Are Not. J Am Chem Soc 2012;134:1093-103.

[42] Dathar GKP, Shelton WA, Xu Y. Trends in the Catalytic Activity of Transition Metals for the Oxygen Reduction Reaction by Lithium. J Phys Chem Lett 2012;3:891-5.

[43] Yang G, Wang Y, Ma Y. A Stable, Magnetic, and Metallic $Li_3O_4$ Compound as a Discharge Product in a Li-Air Battery. J Phys Chem Lett 2014;5:2516-21.

[44] Zheng Y, Song K, Jung J, Li C, Heo Y, Park M et al. Critical Descriptor for the Rational Design of Oxide-Based Catalysts in Rechargeable Li–$O_2$ Batteries: Surface Oxygen Density. Chem Mater 2015;27:3243-9.

[45] Zhang J, Wang D, Xu W, Xiao J, Williford RE. Ambient operation of Li/Air batteries. J Power Sources 2010;195:4332-7.

[46] Xu W, Xiao J, Zhang J, Wang D, Zhang J. Optimization of Nonaqueous Electrolytes for Primary Lithium/Air Batteries Operated in Ambient Environment. J Electrochem Soc 2009;156:A773-9.

[47] Zhang D, Fu Z, Wei Z, Huang T, Yu A. Polarization of Oxygen Electrode in Rechargeable Lithium Oxygen Batteries. J Electrochem Soc 2010;157:A362-5.

[48] Mirzaeian M, Hall PJ. Characterizing capacity loss of lithium oxygen batteries by impedance spectroscopy. J Power Sources 2010;195:6817-24.

[49] Laoire CO, Mukerjee S, Abraham KM, Plichta EJ, Hendrickson MA. Elucidating the Mechanism of Oxygen Reduction for Lithium-Air Battery Applications. J Phys Chem C 2009;113:20127-34.

[50] Laoire CO, Mukerjee S, Abraham KM, Plichta EJ, Hendrickson MA. Influence of Nonaqueous Solvents on the Electrochemistry of Oxygen in the Rechargeable Lithium-Air Battery. J Phys Chem C 2010;114:9178-86.

[51] Mizuno F, Nakanishi S, Kotani Y, Yokoishi S, Iba H. Rechargeable Li-Air Batteries with Carbonate-Based Liquid Electrolytes. Electrochemistry 2010;78:403-5.

[52] Bryantsev VS, Giordani V, Walker W, Blanco M, Zecevic S, Sasaki K et al. Predicting Solvent Stability in Aprotic Electrolyte Li-Air Batteries: Nucleophilic Substitution by the Superoxide Anion Radical (O-2(center dot-)). J Phys Chem A 2011;115:12399-409.

[53] Wang H, Xie K. Investigation of oxygen reduction chemistry in ether and carbonate based electrolytes for Li-$O_2$ batteries. Electrochim Acta 2012;64:29-34.

[54] Lu Y, Kwabi DG, Yao KPC, Harding JR, Zhou J, Zuin L et al. The discharge rate capability of rechargeable Li-$O_2$ batteries. Energy Environ Sci 2011;4:2999-3007.

[55] McCloskey BD, Bethune DS, Shelby RM, Girishkumar G, Luntz AC. Solvents' Critical Role in Nonaqueous Lithium-Oxygen Battery Electrochemistry. J Phys Chem Lett 2011;2:1161-6.

[56] Wang Z, Xu D, Xu J, Zhang L, Zhang X. Graphene Oxide Gel-Derived, Free-Standing, Hierarchically Porous Carbon for High-Capacity and High-Rate Rechargeable Li-$O_2$ Batteries. Adv Funct Mater 2012;22:3699-705.

[57] Gallant BM, Kwabi DG, Mitchell RR, Zhou J, Thompson CV, Shao-Horn Y. Influence of Li2O2 morphology on oxygen reduction and evolution kinetics in Li-O2 batteries. Energy Environ Sci. 2013;6:2518-28.

[58] Laoire CO, Mukerjee S, Plichta EJ, Hendrickson MA, Abraham KM. Rechargeable Lithium/TEGDME-LiPF6/O-2 Battery. J Electrochem Soc 2011;158:A302-8.

[59] Jung H, Hassoun J, Park J, Sun Y, Scrosati B. An improved high-performance lithium-air battery. Nat Chem 2012;4:579-85.

[60] Oh SH, Nazar LF. Oxide Catalysts for Rechargeable High-Capacity Li-$O_2$ Batteries. Adv Energy Mater 2012;2:903-10.

[61] Ma S, Sun L, Cong L, Gao X, Yao C, Guo X et al. Multiporous $MnCo_2O_4$ Microspheres as an Efficient Bifunctional Catalyst for Nonaqueous Li-$O_2$ Batteries. J Phys Chem C 2013;117:25890-7.

[62] Liu S, Wang Z, Yu C, Zhao Z, Fan X, Ling Z et al. Free-standing, hierarchically porous carbon nanotube film as a binder-free electrode for high-energy Li-$O_2$ batteries. J Mater Chem A 2013;1:12033-12037.

[63] Guo Z, Zhou D, Dong X, Qiu Z, Wang Y, Xia Y. Ordered Hierarchical Mesoporous/Macroporous Carbon: A High-Performance Catalyst for Rechargeable Li-$O_2$ Batteries. Adv Mater 2013;25:5668-72.

[64] Lu J, Lei Y, Lau KC, Luo X, Du P, Wen J et al. A nanostructured cathode architecture for low charge overpotential in lithium-oxygen batteries. Nat Commun 2014;5:3290.

[65] Zhang Z, Zhou G, Chen W, Lai Y, Li J. Facile Synthesis of $Fe_2O_3$ Nanoflakes and Their Electrochemical Properties for Li-Air Batteries. ECS Electrochem Lett 2014;3:A8-A10.

[66] Xu D, Wang Z, Xu J, Zhang L, Zhang X. Novel DMSO-based electrolyte for high performance rechargeable Li-$O_2$ batteries. Chem Commun 2012;48:6948-50.

[67] Peng Z, Freunberger SA, Chen Y, Bruce PG. A Reversible and Higher-Rate Li-$O_2$ Battery. Science 2012;337:563-6.

[68] Wei ZH, Tan P, An L, Zhao TS. A non-carbon cathode electrode for lithium-oxygen batteries. Appl Energy 2014;130:134-8.

[69] Tan P, Shyy W, Wei ZH, An L, Zhao TS. A carbon powder-nanotube composite cathode for non-aqueous lithium-air batteries. Electrochim Acta 2014;147:1-8.

[70] Viswanathan V, Thygesen KS, Hummelshoj JS, Norskov JK, Girishkumar G, McCloskey BD et al. Electrical conductivity in $Li_2O_2$ and its role in determining capacity limitations in non-aqueous Li-$O_2$ batteries. J Chem Phys 2011;135:214704.

[71] Ding N, Chien SW, Hor TSA, Lum R, Zong Y, Liu Z. Influence of carbon pore size on the discharge capacity of Li-$O_2$ batteries. J Mater Chem A 2014;2:12433-41.

[72] Meini S, Piana M, Beyer H, Schwaemmlein J, Gasteiger HA. Effect of Carbon Surface Area on First Discharge Capacity of Li-$O_2$ Cathodes and Cycle-Life Behavior in Ether-Based Electrolytes. J Electrochem Soc 2012;159:A2135-42.

[73] Chervin CN, Wattendorf MJ, Long JW, Kucko NW, Rolison DR. Carbon Nanofoam-Based Cathodes for Li-$O_2$ Batteries: Correlation of Pore Solid Architecture and Electrochemical Performance. J Electrochem Soc 2013;160:A1510-6.

[74] Tan P, Shyy W, An L, Wei ZH, Zhao TS. A gradient porous cathode for non-aqueous lithium-air batteries leading to a high capacity. Electrochem Commun 2014;46:111-4.

[75] Johnson L, Li C, Liu Z, Chen Y, Freunberger SA, Ashok PC et al. The role of $LiO_2$ solubility in $O_2$ reduction in aprotic solvents and its consequences for Li-$O_2$ batteries. Nat Chem 2014;6:1091-9.

[76] Abraham KM. Electrolyte-Directed Reactions of the Oxygen Electrode in Lithium-Air Batteries. J Electrochem Soc 2015;162:A3021-31.

[77] Aetukuri NB, McCloskey BD, GarcÃa JM, Krupp LE, Viswanathan V, Luntz AC. Solvating additives drive solution-mediated electrochemistry and enhance toroid growth in non-aqueous Li-$O_2$ batteries. Nat Chem 2015;7:50-6.

[78] Sharon D, Hirsberg D, Salama M, Afri M, Frimer AA, Noked M et al. Mechanistic Role of Li+ Dissociation Level in Aprotic Li-$O_2$ Battery. ACS Appl Mater Interfaces 2016;8:5300-7.

[79] Yang Y, Zhang T, Wang X, Chen L, Wu N, Liu W et al. Tuning the Morphology and Crystal Structure of $Li_2O_2$: A graphene model electrode study for Li–$O_2$ Battery. ACS Appl Mater Interfaces 2016;8:21350-7.

[80] Liu Z, De Jesus LR, Banerjee S, Mukherjee PP. A Mechanistic Evaluation of $Li_xO_y$ formation on $\delta$-$MnO_2$ in Non-Aqueous Li-air Batteries. ACS Appl Mater Interfaces 2016;8:23028-36.

[81] Fan W, Wang B, Guo X, Kong X, Liu J. Nanosize stabilized Li-deficient $Li_{2-x}O_2$ through cathode architecture for high performance Li-$O_2$ batteries. Nano Energy 2016;27:577-86.

[82] Lu J, Lee YJ, Luo X, Lau KC, Asadi M, Wang H et al. A lithium-oxygen battery based on lithium superoxide. Nature 2016;529:377-83.

[83] Ottakam Thotiyl MM, Freunberger SA, Peng Z, Bruce PG. The Carbon Electrode in Nonaqueous Li-$O_2$ Cells. J Am Chem Soc 2013;135:494-500.

[84] Yilmaz E, Yogi C, Yamanaka K, Ohta T, Byon HR. Promoting Formation of Noncrystalline $Li_2O_2$ in the Li-$O_2$ battery with $RuO_2$ nanoparticles. Nano Lett 2013;13:4679-84.

[85] Jian Z, Liu P, Li F, He P, Guo X, Chen M et al. Core-Shell-Structured CNT@$RuO_2$ Composite as a High-Performance Cathode Catalyst for Rechargeable Li-$O_2$ Batteries. Angew Chem Int Ed 2014;53:442-6.

[86] Xu Y, Chen Y, Xu G, Zhang X, Chen Z, Li J et al. $RuO_2$ nanoparticles supported on $MnO_2$ nanorods as high efficient bifunctional electrocatalyst of lithium-oxygen battery. Nano Energy 2016;28:63-70.

[87] McCloskey BD, Scheffler R, Speidel A, Bethune DS, Shelby RM, Luntz AC. On the Efficacy of Electrocatalysis in Nonaqueous Li-$O_2$ Batteries. J Am Chem Soc 2011;133:18038-41.

[88] Lu Y, Shao-Horn Y. Probing the Reaction Kinetics of the Charge Reactions of Nonaqueous Li-$O_2$ Batteries. J Phys Chem Lett 2013;4:93-9.

[89] Black R, Lee J, Adams B, Mims CA, Nazar LF. The Role of Catalysts and Peroxide Oxidation in Lithium-Oxygen Batteries. Angew Chem Int Ed 2013;52:392-6.

[90] Xia C, Waletzko M, Chen L, Peppler K, Klar PJ, Janek J. Evolution of $Li_2O_2$ Growth and Its Effect on Kinetics of Li-$O_2$ Batteries. ACS Appl Mater Interfaces 2014;6:12083-92.

[91] Ganapathy S, Adams BD, Stenou G, Anastasaki MS, Goubitz K, Miao X et al. Nature of $Li_2O_2$ oxidation in a Li-$O_2$ Battery Revealed by Operando X-ray Diffraction. J Am Chem Soc 2014;136:16335-44.

[92] Xu J, Wang Z, Xu D, Zhang L, Zhang X. Tailoring deposition and morphology of discharge products towards high-rate and long-life lithium-oxygen batteries. Nat Commun 2013;4.

[93] Zhang SS, Foster D, Read J. Discharge characteristic of a non-aqueous electrolyte Li/$O_2$ battery. J Power Sources 2010;195:1235-40.

[94] Gallagher KG, Goebel S, Greszler T, Mathias M, Oelerich W, Eroglu D et al. Quantifying the promise of lithium-air batteries for electric vehicles. Energy Environ Sci 2014;7:1555-63.

[95] Meini S, Tsiouvaras N, Schwenke KU, Piana M, Beyer H, Lange L et al. Rechargeability of Li-air cathodes pre-filled with discharge products using an ether-based electrolyte solution: implications for cycle-life of Li-air cells. Phys Chem Chem Phys 2013;15:11478-93.

[96] Wang G, Huang L, Liu S, Xie J, Zhang S, Zhe P et al. Understanding Moisture and Carbon Dioxide Involved Interfacial Reactions on Electrochemical Performance of Lithium-Air Batteries Catalyzed by Gold/Manganese-Dioxide. ACS Appl Mater Interfaces 2015;7:23876-84.

[97] Zhang J, Xu W, Liu W. Oxygen-selective immobilized liquid membranes for operation of lithium-air batteries in ambient air. J Power Sources 2010;195:7438-44.

[98] Crowther O, Keeny D, Moureau DM, Meyer B, Salomon M, Hendrickson M. Electrolyte optimization for the primary lithium metal air battery using an oxygen selective membrane. J Power Sources 2012;202:347-51.

[99] Shui J, Okasinski JS, Kenesei P, Dobbs HA, Zhao D, Almer JD et al. Reversibility of anodic lithium in rechargeable lithium-oxygen batteries. Nat Commun 2013;4:2255.

[100] Assary RS, Lu J, Du P, Luo X, Zhang X, Ren Y et al. The Effect of Oxygen Crossover on the Anode of a Li-$O_2$ Battery using an Ether-Based Solvent: Insights from Experimental and Computational Studies. ChemSusChem 2013;6:51-5.

[101] Younesi R, Hahlin M, Roberts M, Edstrom K. The SEI layer formed on lithium metal in the presence of oxygen: A seldom considered component in the development of the Li-$O_2$ battery. J Power Sources 2013;225:40-5.

[102] Lopez CM, Vaughey JT, Dees DW. Morphological Transitions on Lithium Metal Anodes. J Electrochem Soc 2009;156:A726-9.

[103] Nishikawa K, Mori T, Nishida T, Fukunaka Y, Rosso M. Li dendrite growth and $Li^+$ ionic mass transfer phenomenon. J Electroanal Chem 2011;661:84-9.

[104] Ding F, Xu W, Chen X, Zhang J, Engelhard MH, Zhang Y et al. Effects of Carbonate Solvents and Lithium Salts on Morphology and Coulombic Efficiency of Lithium Electrode. J Electrochem Soc 2013;160:A1894-901.

[105] Nishida T, Nishikawa K, Rosso M, Fukunaka Y. Optical observation of Li dendrite growth in ionic liquid. Electrochim Acta 2013;100:333-41.

[106] Park MS, Ma SB, Lee DJ, Im D, Doo S, Yamamoto O. A Highly Reversible Lithium Metal Anode. Scientific Reports 2014;4:3815.

[107] Visco SJ, Nimon E, Katz B, De Jonghe LC, Chu MY. Lithium/air semi-fuel cells: High energy density batteries based on lithium metal electrodes. The 12th International Meeting on Lithium Batteries Abstracts, Nara, Japan 2004;Abstract No. 53.

[108] Zhang T, Imanishi N, Hasegawa S, Hirano A, Xie J, Takeda Y et al. Water-Stable Lithium Anode with the Three-Layer Construction for Aqueous Lithium-Air Secondary Batteries. Electrochem Solid State Lett 2009;12:A132-5.

[109] Zhang T, Imanishi N, Shimonishi Y, Hirano A, Takeda Y, Yamamoto O et al. A novel high energy density rechargeable lithium/air battery. Chem Commun 2010;46:1661-3.

[110] Shimonishi Y, Zhang T, Johnson P, Imanishi N, Hirano A, Takeda Y et al. A study on lithium/air secondary batteries-Stability of NASICON-type glass ceramics in acid solutions. J Power Sources 2010;195:6187-91.

[111] Zhang T, Imanishi N, Shimonishi Y, Hirano A, Xie J, Takeda Y et al. Stability of a Water-Stable Lithium Metal Anode for a Lithium-Air Battery with Acetic Acid-Water Solutions. J Electrochem Soc 2010;157:A214-8.

[112] Zhang T, Liu S, Imanishi N, Hirano A, Takeda Y, Yamamoto O. Water-Stable Lithium Electrode and Its Application in Aqueous Lithium/Air Secondary Batteries. Electrochemistry 2010;78:360-2.

[113] Puech L, Cantau C, Vinatier P, Toussaint G, Stevens P. Elaboration and characterization of a free standing LiSICON membrane for aqueous lithium-air battery. J Power Sources 2012;214:330-6.

[114] Zhang T, Imanishi N, Takeda Y, Yamamoto O. Aqueous Lithium/Air Rechargeable Batteries. Chem Lett 2011;40:668-73.

[115] Wang Y, Zhou H. A lithium-air battery with a potential to continuously reduce $O_2$ from air for delivering energy. J Power Sources 2010;195:358-61.

[116] He P, Wang Y, Zhou H. A Li-air fuel cell with recycle aqueous electrolyte for improved stability. Electrochem Commun 2010;12:1686-9.

[117] He P, Wang Y, Zhou H. Titanium nitride catalyst cathode in a Li-air fuel cell with an acidic aqueous solution. Chem Commun 2011;47:10701-3.

[118] Yoo E, Zhou H. Li-Air Rechargeable Battery Based on Metal-free Graphene Nanosheet Catalysts. Acs Nano 2011;5:3020-6.

[119] He H, Niu W, Asl NM, Salim J, Chen R, Kim Y. Effects of aqueous electrolytes on the voltage behaviors of rechargeable Li-air batteries. Electrochim Acta 2012;67:87-94.

[120] Wang S, Dong S, Wang J, Zhang L, Han P, Zhang C et al. Oxygen-enriched carbon material for catalyzing oxygen reduction towards hybrid electrolyte Li-air battery. J Mater Chem 2012;22:21051-6.

[121] Zheng JP, Liang RY, Hendrickson M, Plichta EJ. Theoretical energy density of Li-air batteries. J Electrochem Soc 2008;155:A432-7.

[122] Zheng JP, Andrei P, Hendrickson M, Plichta EJ. The Theoretical Energy Densities of Dual-Electrolytes Rechargeable Li-Air and Li-Air Flow Batteries. J Electrochem Soc 2011;158:A43-6.

[123] Shimonishi Y, Zhang T, Imanishi N, Im D, Lee DJ, Hirano A et al. A study on lithium/air secondary batteries-Stability of the NASICON-type lithium ion conducting solid electrolyte in alkaline aqueous solutions. J Power Sources 2011;196:5128-32.

[124] Li L, Manthiram A. Decoupled bifunctional air electrodes for high-performance hybrid lithium-air batteries. Nano Energy 2014;9:94-100.

[125] Li L, Liu C, He G, Fan D, Manthiram A. Hierarchical pore-in-pore and wire-in-wire catalysts for rechargeable Zn- and Li-air batteries with ultra-long cycle life and high cell efficiency. Energy Environ Sci 2015;8:3274-82.

[126] Li F, Kitaura H, Zhou H. The pursuit of rechargeable solid-state Li-air batteries. Energy Environ Sci 2013;6:2302-11.

[127] Kumar B, Kumar J. Cathodes for Solid-State Lithium-Oxygen Cells: Roles of Nasicon Glass-Ceramics. J Electrochem Soc 2010;157:A611-6.

[128] Kumar B, Kumar J, Leese R, Fellner JP, Rodrigues SJ, Abraham KM. A Solid-State, Rechargeable, Long Cycle Life Lithium-Air Battery. J Electrochem Soc 2010;157:A50-4.

[129] Aleshin GY, Semenenko DA, Belova AI, Zakharchenko TK, Itkis DM, Goodilin EA et al. Protected anodes for lithium-air batteries. Solid State Ionics 2011;184:62-4.

[130] Kichambare P, Rodrigues S, Kumar J. Mesoporous Nitrogen-Doped Carbon-Glass Ceramic Cathodes for Solid-State Lithium-Oxygen Batteries. ACS Appl Mater Interfaces 2012;4:49-52.

[131] Kitaura H, Zhou H. Electrochemical Performance of Solid-State Lithium-Air Batteries Using Carbon Nanotube Catalyst in the Air Electrode. Adv Energy Mater 2012;2:889-94.

[132] Lu Y, Wen Z, Jin J, Cui Y, Wu M, Sun S. Mesoporous carbon nitride loaded with Pt nanoparticles as a bifunctional air electrode for rechargeable lithium-air battery. J Solid State Electrochem 2012;16:1863-8.

[133] Truong TT, Qin Y, Ren Y, Chen Z, Chan MK, Greeley JP et al. Single-Crystal Silicon Membranes with High Lithium Conductivity and Application in Lithium-Air Batteries. Adv Mater 2011;23:4947-52.

[134] Zhang D, Li R, Huang T, Yu A. Novel composite polymer electrolyte for lithium air batteries. J Power Sources 2010;195:1202-6.

[135] Zhu XB, Zhao TS, Wei ZH, Tan P, Zhao G. A novel solid-state Li-$O_2$ battery with an integrated electrolyte and cathode structure. Energy Environ Sci 2015;8:2782-90.

[136] Park M, Sun H, Lee H, Lee J, Cho J. Lithium-Air Batteries: Survey on the Current Status and Perspectives Towards Automotive Applications from a Battery Industry Standpoint. Adv Energy Mater 2012;2:780-800.

[137] Lu J, Li L, Park J, Sun Y, Wu F, Amine K. Aprotic and Aqueous Li-$O_2$ Batteries. Chem Rev 2014;114:5611-40.

[138] Shen Y, Sun D, Yu L, Zhang W, Shang Y, Tang H et al. A high-capacity lithium-air battery with Pd modified carbon nanotube sponge cathode working in regular air. Carbon 2013;62:288-95.

[139] Visco SJ, Nimon VY, Petrov A, Pridatko K, Goncharenko N, Nimon E et al. Aqueous and nonaqueous lithium-air batteries enabled by water-stable lithium metal electrodes. J Solid State Electrochem 2014;18:1443-56.

[140] Sahapatsombut U, Cheng H, Scott K. Modelling the micro–macro homogeneous cycling behaviour of a lithium–air battery. J Power Sources 2013;227:243-53.

[141] Nishikawa K, Mori T, Nishida T, Fukunaka Y, Rosso M, Homma T. In Situ Observation of Dendrite Growth of Electrodeposited Li Metal. J Electrochem Soc 2010;157:A1212-7.

[142] Zheng G, Lee SW, Liang Z, Lee H, Yan K, Yao H et al. Interconnected hollow carbon nanospheres for stable lithium metal anodes. Nat Nano 2014;9:618-23.

[143] Xu W, Wang J, Ding F, Chen X, Nasybutin E, Zhang Y et al. Lithium metal anodes for rechargeable batteries. Energy Environ Sci 2014;7:513-37.

[144] Ayers MW, Huang HS. A comprehensive finite element model for lithium–oxygen batteries. J Mater Res 2016;31:2728-35.

[145] Cui Y, Wen Z, Liu Y. A free-standing-type design for cathodes of rechargeable Li-$O_2$ batteries. Energy Environ Sci 2011;4:4727-34.

[146] Kim ST, Choi N, Park S, Cho J. Optimization of Carbon- and Binder-Free Au Nanoparticle-Coated Ni Nanowire Electrodes for Lithium-Oxygen Batteries. Adv Energy Mater 2015;5:1401030.

[147] Wu B, Zhang H, Zhou W, Wang M, Li X, Zhang H. Carbon-Free CoO Mesoporous Nanowire Array Cathode for High-Performance Aprotic Li-$O_2$ batteries. ACS Appl Mater Interfaces 2015;7:23182-9.

[148] Wei Z, Zhao T, Zhu X, An L, Tan P. Integrated Porous Cathode made of Pure Perovskite Lanthanum Nickel Oxide for Nonaqueous Lithium-Oxygen Batteries. Energy Tech 2015;3:1093-100.

[149] Wei ZH, Zhao TS, Zhu XB, Tan P. $MnO_{2-x}$ nanosheets on stainless steel felt as a carbon- and binder-free cathode for non-aqueous lithium-oxygen batteries. J Power Sources 2016;306:724-32.

[150] Zhao G, Zhang L, Niu Y, Sun K, Rooney D. Enhanced durability of Li-$O_2$ batteries employing vertically standing Ti nanowire array supported cathodes. J Mater Chem A 2016;4:4009-14.

[151] Shui J, Du F, Xue C, Li Q, Dai L. Vertically Aligned N-Doped Coral-like Carbon Fiber Arrays as Efficient Air Electrodes for High-Performance Nonaqueous Li-$O_2$ Batteries. ACS Nano 2014;8:3015-22.

[152] Adams BD, Black R, Radtke C, Williams Z, Mehdi BL, Browning ND et al. The Importance of Nanometric Passivating Films on Cathodes for Li-Air Batteries. ACS Nano 2014;8:12483-93.

[153] Tan P, Wei Z, Shyy W, Zhao TS, Zhu X. A nano-structured $RuO_2$/NiO cathode enables the operation of non-aqueous lithium-air batteries in ambient air. Energy Environ Sci 2016;9:1783-93.

[154] Sun B, Munroe P, Wang G. Ruthenium nanocrystals as cathode catalysts for lithium-oxygen batteries with a superior performance. Sci Rep 2013;3:2247.

[155] Yao KPC, Lu Y, Amanchukwu CV, Kwabi DG, Risch M, Zhou J et al. The influence of transition metal oxides on the kinetics of $Li_2O_2$ oxidation in Li-$O_2$ batteries: high activity of chromium oxides. Phys Chem Chem Phys 2014;16:2297-304.

[156] Sandhu SS, Brutchen GW, Fellner JP. Lithium/air cell: Preliminary mathematical formulation and analysis. J Power Sources 2007;170:196-209.

[157] Li X, Faghri A. Optimization of the Cathode Structure of Lithium-Air Batteries Based on a Two-Dimensional, Transient, Non-Isothermal Model. J Electrochem Soc 2012;159:A1747-54.

[158] Sandhu SS, Fellner JP, Brutchen GW. Diffusion-limited model for a lithium/air battery with an organic electrolyte. J Power Sources 2007;164:365-71.

[159] Williford RE, Zhang J. Air electrode design for sustained high power operation of Li/air batteries. J Power Sources 2009;194:1164-70.

[160] Read J. Characterization of the lithium/oxygen organic electrolyte battery. J Electrochem Soc 2002;149:A1190-5.

[161] Read J, Mutolo K, Ervin M, Behl W, Wolfenstine J, Driedger A et al. Oxygen transport properties of organic electrolytes and performance of lithium/oxygen battery. J Electrochem Soc 2003;150:A1351-6.

[162] Andrei P, Zheng JP, Hendrickson M, Plichta EJ. Some Possible Approaches for Improving the Energy Density of Li-Air Batteries. J Electrochem Soc 2010;157:A1287-95.

[163] Andrei P, Zheng J, Hendrickson M, Plichta E. Solid-State and Integrated Circuit Technology, 2010 10th IEEE International Conference. 2010:2016-8.

[164] Lai W, Ciucci F. Mathematical modeling of porous battery electrodes—Revisit of Newman's model. Electrochim Acta 2011;56:4369-77.

[165] Marcicki J, Conlisk A, Rizzoni G. A lithium-ion battery model including electrical double layer effects. J Power Sources 2014;251:157-69.

[166] Doyle M, Fuller TF, Newman J. Modeling of galvanostatic charge and discharge of the lithium/polymer/insertion cell. J Electrochem Soc 1993;140:1526-33.

[167] Fuller TF, Doyle M, Newman J. Simulation and optimization of the dual lithium ion insertion cell. J Electrochem Soc 1994;141:1-10.

[168] Xue K, Plett GL. A convective transport theory for high rate discharge in lithium ion cells. Electrochim Acta 2013;87:575-90.

[169] Latz A, Zausch J. Thermodynamic consistent transport theory of Li-ion batteries. J Power Sources 2011;196:3296-302.

[170] Liu Y, Suo L, Lin H, Yang W, Fang Y, Liu X et al. Novel approach for a high-energy-density Li-air battery: tri-dimensional growth of $Li_2O_2$ crystals tailored by electrolyte Li+ ion concentrations. J Mater Chem A 2014;2:9020-4.

[171] Jung CY, Zhao TS, An L. Modeling of lithium–oxygen batteries with the discharge product treated as a discontinuous deposit layer. J Power Sources 2015;273:440-7.

[172] Sergeev AV, Chertovich AV, Itkis DM, Goodilin EA, Khokhlov AR. Effects of cathode and electrolyte properties on lithium–air battery performance: Computational study. J Power Sources 2015;279:707-12.

[173] Sergeev AV, Chertovich AV, Itkis DM. Modeling of the lithium-air battery cathodes with broad pore size distribution. Chemical Physics Letters 2016;660:149-54.

[174] Newman J, Thomas-Alyea KE. Electrochemical systems. John Wiley & Sons, 2012.

[175] Boden N, Leng S, Ward I. Ionic conductivity and diffusivity in polyethylene oxode/electrolyte solutions as models for polymer electrolytes. Solid State Ionics 1991;45:261-70.

[176] Chintapalli M, Timachova K, Olson KR, Mecham SJ, Devaux D, DeSimone JM et al. Relationship between conductivity, ion diffusion, and transference number in perfluoropolyether electrolytes. Macromolecules 2016;49:3508-15.

[177] Quiroga MA, Xue K, Nguyen T, Tułodziecki M, Huang H, Franco AA. A multiscale model of electrochemical double layers in energy conversion and storage devices. J Electrochem Soc 2014;161:E3302-10.

[178] Cui ZH, Fan WG, Guo XX. Lithium-oxygen cells with ionic-liquid-based electrolytes and vertically aligned carbon nanotube cathodes. J Power Sources 2013;235:251-5.

[179] Adams BD, Black R, Williams Z, Fernandes R, Cuisinier M, Berg EJ et al. Towards a Stable Organic Electrolyte for the Lithium Oxygen Battery. Adv Energy Mater 2015;5:1400867.

[180] Elia GA, Hassoun J, Kwak W-, Sun Y-, Scrosati B, Mueller F et al. An Advanced Lithium-Air Battery Exploiting an Ionic Liquid-Based Electrolyte. Nano Lett 2014;14:6572-7.

[181] Khan A, Zhao C. Enhanced performance in mixture DMSO/ionic liquid electrolytes: Toward rechargeable Li–$O_2$ batteries. Electrochem Commun 2014;49:1-4.

[182] Ara M, Meng T, Nazri G, Salley SO, Simon Ng KY. Ternary Imidazolium-Pyrrolidinium-Based Ionic Liquid Electrolytes for Rechargeable Li-$O_2$ Batteries. J Electrochem Soc 2014;161:A1969-75.

[183] Ferrari S, Quartarone E, Tomasi C, Bini M, Galinetto P, Fagnoni M et al. Investigation of Ether-Based Ionic Liquid Electrolytes for Lithium-$O_2$ Batteries. J Electrochem Soc 2015;162:A3001-6.

[184] Xie J, Dong Q, Madden I, Yao X, Cheng Q, Dornath P et al. Achieving Low Overpotential Li–$O_2$ battery operations by $Li_2O_2$ Decomposition through One-Electron Processes. Nano Lett 2015;15:8371-6.

[185] Lim H, Song H, Kim J, Gwon H, Bae Y, Park K et al. Superior Rechargeability and Efficiency of Lithium-Oxygen Batteries: Hierarchical Air Electrode Architecture Combined with a Soluble Catalyst. Angew Chem Int Ed 2014;53:3926-31.

[186] Xu W, Xiao J, Wang D, Zhang J, Zhang J. Effects of Nonaqueous Electrolytes on the Performance of Lithium/Air Batteries. J Electrochem Soc 2010;157:A219-24.

[187] Gwak G, Ju H. Three-dimensional transient modeling of a non-aqueous electrolyte lithium-air battery. Electrochim Acta 2016;201:395-409.

[188] Tan P, Shyy W, Zhao T. What is the ideal distribution of electrolyte inside cathode pores of non-aqueous lithium-air batteries? Science Bulletin 2015;60:975-6.

[189] Zhang T, Zhou H. From Li?O2 to Li?Air Batteries: Carbon Nanotubes/Ionic Liquid Gels with a Tricontinuous Passage of Electrons, Ions, and Oxygen. Angew Chem Int Ed 2012;51:11062-7.

[190] Xia C, Bender CL, Bergner B, Peppler K, Janek J. An electrolyte partially-wetted cathode improving oxygen diffusion in cathodes of non-aqueous Li-air batteries. Electrochem Commun 2013;26:93-6.

[191] Balaish M, Kraytsberg A, Ein-Eli Y. Realization of an Artificial Three-Phase Reaction Zone in a Li-Air Battery. ChemElectroChem 2014;1:90-4.

[192] Kim DS, Park YJ. A simple method for surface modification of carbon by polydopamine coating for enhanced Li–air batteries. Electrochim Acta 2014;132:297-306.

[193] Lee HC, Roev V, Kim TY, Park MS, Lee DJ, Im D et al. Numerical predictions and experimental verification of Li-$O_2$ battery capacity limits for cathodes with spherical conductors and solid electrolytes. J Power Sources 2016;331:122-31.

[194] Ye L, Lv W, Zhang KH, Wang X, Yan P, Dickerson JH et al. A new insight into the oxygen diffusion in porous cathodes of lithium-air batteries. Energy 2015;83:669-73.

[195] Caravella A. Dusty-Gas Model (DGM). In: Drioli E, Giorno L, editors. Encyclopedia of Membranes, Berlin, Heidelberg 2016:604-605.

[196] Veldsink J, Van Damme R, Versteeg G, Van Swaaij W. The use of the dusty-gas model for the description of mass transport with chemical reaction in porous media. The Chemical Engineering Journal and the Biochemical Engineering Journal 1995;57:115-25.

[197] Suwanwarangkul R, Croiset E, Fowler M, Douglas P, Entchev E, Douglas M. Performance comparison of Fick's, dusty-gas and Stefan–Maxwell models to predict the concentration overpotential of a SOFC anode. J Power Sources 2003;122:9-18.

[198] Safari M, Adams B, Nazar L. Kinetics of oxygen reduction in aprotic Li–$O_2$ cells: a model-based study. J Phys Chem Lett 2014;5:3486-91.

[199] Rinaldi A, Wijaya O, Hoster H. Lithium–Oxygen Cells: An Analytical Model to Explain Key Features in the Discharge Voltage Profiles. ChemElectroChem 2016;3:1944-50.

[200] Xue K, McTurk E, Johnson L, Bruce PG, Franco AA. A comprehensive model for non-aqueous lithium air batteries involving different reaction mechanisms. J Electrochem Soc 2015;162:A614-21.

[201] Griffith LD, Sleightholme AES, Mansfield JF, Siegel DJ, Monroe CW. Correlating Li/$O_2$ Cell Capacity and Product Morphology with Discharge Current. ACS Appl Mater Interfaces 2015;7:7670-8.

[202] Tan P, Shyy W, Zhao TS, Wei ZH, An L. Discharge product morphology versus operating temperature in non-aqueous lithium-air batteries. J Power Sources 2015;278:133-40.

[203] Tan P, Shi L, Shyy W, Zhao T. Morphology of the Discharge Product in Non-aqueous Lithium–Oxygen Batteries: Furrowed Toroid Particles Correspond to a Lower Charge Voltage. Energy Tech 2016;4:393-400.

[204] Adams BD, Radtke C, Black R, Trudeau ML, Zaghib K, Nazar LF. Current density dependence of peroxide formation in the Li-$O_2$ battery and its effect on charge. Energy Environ Sci 2013;6:1772-8.

[205] Horstmann B, Gallant B, Mitchell R, Bessler WG, Shao-Horn Y, Bazant MZ. Rate-dependent morphology of $Li_2O_2$ growth in Li–$O_2$ batteries. J Phys Chem Lett 2013;4:4217-22.

[206] Lau S, Archer LA. Nucleation and Growth of Lithium Peroxide in the Li–O2 Battery. Nano lett 2015;15:5995-6002.

[207] Milchev A, Stoyanov S, Kaischev R. Atomistic theory of electrolytic nucleation: I. Thin Solid Films 1974;22:255-65.

[208] Liu J, Khaleghi Rahimian S, Monroe CW. Capacity-limiting mechanisms in Li/$O_2$ batteries. Phys Chem Chem Phys 2016;18:22840-51.

[209] Wang Y. Modeling discharge deposit formation and its effect on lithium-air battery performance. Electrochim Acta 2012;75:239-46.

[210] Bevara V, Andrei P. Changing the cathode microstructure to improve the capacity of Li-air batteries: theoretical predictions. J Electrochem Soc 2014;161:A2068-79.

[211] Radin MD, Siegel DJ. Charge transport in lithium peroxide: relevance for rechargeable metal-air batteries. Energy Environ Sci 2013;6:2370-9.

[212] Andersen CP, Hu H, Qiu G, Kalra V, Sun Y. Pore-Scale Transport Resolved Model Incorporating Cathode Microstructure and Peroxide Growth in Lithium-Air Batteries. J Electrochem Soc 2015;162:A1135-45.

[213] Luntz A, Viswanathan V, Voss J, Varley J, Nørskov J, Scheffler R et al. Tunneling and polaron charge transport through $Li_2O_2$ in $Li–O_2$ batteries. J Phys Chem Lett 2013;4:3494-9.

[214] Xue K, Nguyen T, Franco AA. Impact of the cathode microstructure on the discharge performance of lithium air batteries: a multiscale model. J Electrochem Soc 2014;161:E3028-35.

[215] Radin MD, Monroe CW, Siegel DJ. Impact of Space-Charge Layers on Sudden Death in $Li/O_2$ Batteries. J Phys Chem Lett 2015;6:3017-22.

[216] Wang Y, Cho SC. Analysis of air cathode perfomance for lithium-air batteries. J Electrochem Soc 2013;160:A1847-55.

[217] Wang Y, Cho SC. Analysis and multi-dimensional modeling of lithium-air batteries. J Electrochem Soc 2015;162:A114-24.

[218] Wang Y, Wang Z, Yuan H, Li T. Discharge oxide storage capacity and voltage loss in li-air battery. Electrochim Acta 2015;180:382-93.

[219] Olivares-Marín M, Palomino P, Enciso E, Tonti D. Simple method to relate experimental pore size distribution and discharge capacity in cathodes for Li/$O_2$ batteries. J Phys Chem C 2014;118:20772-83.

[220] Oh SH, Black R, Pomerantseva E, Lee J, Nazar LF. Synthesis of a metallic mesoporous pyrochlore as a catalyst for lithium-$O_2$ batteries. Nat Chem 2012;4:1004-10.

[221] Nimon VY, Visco SJ, De Jonghe LC, Volfkovich YM, Bograchev DA. Modeling and experimental study of porous carbon cathodes in Li-$O_2$ cells with non-aqueous electrolyte. ECS Electrochem Lett 2013;2:A33-5.

[222] Chen X, Bevara V, Andrei P, Hendrickson M, Plichta E, Zheng J. Combined effects of oxygen diffusion and electronic resistance in Li-air batteries with carbon nanofiber cathodes. J Electrochem Soc 2014;161:A1877-83.

[223] Li X. A modeling study of the pore size evolution in lithium-oxygen battery electrodes. J Electrochem Soc 2015;162:A1636-45.

[224] Blanquer G, Yin Y, Quiroga MA, Franco AA. Modeling Investigation of the Local Electrochemistry in Lithium-$O_2$ Batteries: A Kinetic Monte Carlo Approach. J Electrochem Soc 2016;163:A329-37.

[225] Jithin M, Das M, De A. Lattice Boltzmann Simulation of Lithium Peroxide Formation in Lithium-Oxygen Battery. J Electrochem En Conv Stor 2016;13:031003.

[226] Ryan EM, Ferris K, Tartakovsky A, Khaleel M. Computational modeling of transport limitations in Li-air batteries. ECS Transactions 2013;45:123-36.

[227] Bao J, Xu W, Bhattacharya P, Stewart M, Zhang J, Pan W. Discharge Performance of Li–$O_2$ Batteries Using a Multiscale Modeling Approach. The J Phys Chem C 2015;119:14851-60.

[228] Ryu W, Gittleson FS, Li J, Tong X, Taylor AD. A new design strategy for observing lithium oxide growth-evolution interactions using geometric catalyst positioning. Nano Lett 2016;16:4799-806.

[229] Dabrowski T, Struck A, Fenske D, Maaß P, Ciacchi LC. Optimization of Catalytically Active Sites Positioning in Porous Cathodes of Lithium/Air Batteries Filled with Different Electrolytes. J Electrochem Soc 2015;162:A2796-804.

[230] Lim H, Park K, Gwon H, Hong J, Kim H, Kang K. The potential for long-term operation of a lithium-oxygen battery using a non-carbonate-based electrolyte. Chem Commun 2012;48:8374-6.

[231] Sahapatsombut U, Cheng H, Scott K. Modelling of electrolyte degradation and cycling behaviour in a lithium–air battery. J Power Sources 2013;243:409-18.

[232] Peng Z, Freunberger SA, Hardwick LJ, Chen Y, Giordani V, Barde F et al. Oxygen Reactions in a Non-Aqueous $Li^+$ Electrolyte. Angew Chem Int Ed 2011;50:6351-5.

[233] Welford PJ, Brookes BA, Wadhawan JD, McPeak HB, Hahn CE, Compton RG. The Electro-reduction of Carbon Dioxide in Dimethyl Sulfoxide at Gold Microdisk Electrodes: Current| Voltage Waveshape Analysis. The J Phys Chem B 2001;105:5253-61.

[234] Cheng H, Scott K. Selection of oxygen reduction catalysts for rechargeable lithium-air batteries-Metal or oxide? Applied Catalysis B-Environmental 2011;108:140-51.

[235] Sahapatsombut U, Cheng H, Scott K. Modelling of operation of a lithium-air battery with ambient air and oxygen-selective membrane. J Power Sources 2014;249:418-30.

[236] Ling C, Zhang R, Takechi K, Mizuno F. Intrinsic Barrier to Electrochemically Decompose $Li_2CO_3$ and LiOH. J Phys Chem C 2014;118:26591-8.

[237] Tan P, Wei Z, Shyy W, Zhao TS. Prediction of the theoretical capacity of non-aqueous lithium-air batteries. Appl Energy 2013;109:275-82.

[238] Yoo K, Banerjee S, Dutta P. Modeling of volume change phenomena in a Li–air battery. J Power Sources 2014;258:340-50.

[239] Huang J, Faghri A. Analysis of electrolyte level change in a lithium air battery. J Power Sources 2016;307:45-55.

[240] Hirt C, Amsden AA, Cook J. An arbitrary Lagrangian-Eulerian computing method for all flow speeds. J Comput Phys 1974;14:227-53.

[241] McCloskey BD, Speidel A, Scheffler R, Miller DC, Viswanathan V, Hummelshoj JS et al. Twin Problems of Interfacial Carbonate Formation in Nonaqueous Li-$O_2$ Batteries. J Phys Chem Lett 2012;3:997-1001.

[242] Yin Y, Gaya C, Torayev A, Thangavel V, Franco AA. Impact of $Li_2O_2$ Particle Size on Li-$O_2$ Battery Charge Process: Insights from a Multi-Scale Modeling Perspective. J Phys Chem Lett 2016;7:3897-902.

[243] Zhai D, Wang H, Yang J, Lau KC, Li K, Amine K et al. Disproportionation in Li-$O_2$ Batteries Based on a Large Surface Area Carbon Cathode. J Am Chem Soc 2013;135:15364-72.

[244] Chen Y, Freunberger SA, Peng Z, Fontaine O, Bruce PG. Charging a Li-$O_2$ battery using a redox mediator. Nat Chem 2013;5:489-94.

[245] Sun D, Shen Y, Zhang W, Yu L, Yi Z, Yin W et al. A Solution-Phase Bifunctional Catalyst for Lithium-Oxygen Batteries. J Am Chem Soc 2014;136:8941-6.

[246] Bergner BJ, Schurmann A, Peppler K, Garsuch A, Janek J. TEMPO: A Mobile Catalyst for Rechargeable Li-$O_2$ Batteries. J Am Chem Soc 2014;136:15054-64.

[247] Zhang T, Liao K, He P, Zhou H. A self-defense redox mediator for efficient lithium-$O_2$ batteries. Energy Environ Sci. 2016;9:1024-30.

[248] Kwak W, Hirshberg D, Sharon D, Afri M, Frimer AA, Jung H et al. Li–$O_2$ cells with LiBr as an electrolyte and a redox mediator. Energy Environ Sci 2016;9:2334-45.

[249] Bergner BJ, Hofmann C, Schürmann A, Schröder D, Peppler K, Schreiner PR et al. Understanding the fundamentals of redox mediators in Li–$O_2$ batteries: A case study on nitroxides. Phys Chem Chem Phys 2015;17:31769-79.

[250] Grübl D, Bergner BJ, Schröder D, Janek J, Bessler WG. Multi-Step Reaction Mechanisms in Non-Aqueous Lithium-Oxygen Batteries with Redox Mediator: A Model-Based Study. The J Phys Chem C 2016;120:24623-36.

[251] Albertus P, Girishkumar G, McCloskey B, Sanchez-Carrera RS, Kozinsky B, Christensen J et al. Identifying Capacity Limitations in the Li/Oxygen Battery Using Experiments and Modeling. J Electrochem Soc 2011;158:A343-51.

[252] Yoo K, Banerjee S, Dutta P. Modeling of volume change phenomena in a Li–air battery. J Power Sources 2014;258:340-50.

[253] Yuan J, Yu J, Sundén B. CFD Analysis of Multi-phase Reacting Transport Phenomena in Discharge Process of Non-aqueous Lithium-Air Battery. International Journal of Electrical, Computer, Energetic, Electronic and Communication Engineering 2015;9:283-91.

[254] Ren Y, Zhao T, Tan P, Wei Z, Zhou X. Modeling of an aprotic Li-$O_2$ battery incorporating multiple-step reactions. Appl Energy 2017;187:706-16.

[255] Yin Y, Zhao R, Deng Y, Franco AA. Compactness of Lithium Peroxide Thin Film Formed in Li-$O_2$ Batteries and Its Link to Charge Transport Mechanism: Insights from Stochastic Simulations. J Phys Chem Lett 2017;8:599-604.

[256] Mohazabrad F, Wang F, Li X. Influence of the Oxygen Electrode Open Ratio and Electrolyte Evaporation on the Performance of Li-$O_2$ Batteries. ACS Appl Mater Interfaces 2017;9:15459-69.

[257] Gittleson FS, Jones RE, Ward DK, Foster ME. Oxygen solubility and transport in Li–air battery electrolytes: establishing criteria and strategies for electrolyte design. Energy Environ Sci 2017;10:1167-79.

[258] Olivares-Marín M, Sorrentino A, Lee R, Pereiro E, Wu N, Tonti D. Spatial distributions of discharged products of lithium–oxygen batteries revealed by synchrotron X-ray transmission microscopy. Nano Lett 2015;15:6932-8.

[259] Zheng H, Xiao D, Li X, Liu Y, Wu Y, Wang J et al. New Insight in Understanding Oxygen Reduction and Evolution in Solid-State Lithium–Oxygen Batteries Using an in Situ Environmental Scanning Electron Microscope. Nano Lett 2014;14:4245-9.

[260] Mitchell RR, Gallant BM, Thompson CV, Shao-Horn Y. All-carbon-nanofiber electrodes for high-energy rechargeable Li-$O_2$ batteries. Energy Environ Sci 2011;4:2952-8.

[261] Li F, Wu S, Li D, Zhang T, He P, Yamada A et al. The water catalysis at oxygen cathodes of lithium-oxygen cells. Nat Commun 2015;6:7843.

[262] Wu S, Tang J, Li F, Liu X, Yamauchi Y, Ishida M et al. A Synergistic System for Lithium–Oxygen Batteries in Humid Atmosphere Integrating a Composite Cathode and a Hydrophobic Ionic Liquid-Based Electrolyte. Adv Funct Mater 2016;26:3291-8.

[263] Hong M, Choi HC, Byon HR. Nanoporous NiO Plates with a Unique Role for Promoted Oxidation of Carbonate and Carboxylate Species in the Li-$O_2$ Battery. Chem Mater 2015;27:2234-41.

[264] Wang R, Yu X, Bai J, Li H, Huang X, Chen L et al. Electrochemical decomposition of $Li_2CO_3$ in NiO-$Li_2CO_3$ nanocomposite thin film and powder electrodes. J Power Sources 2012;218:113-8.

[265] Song S, Xu W, Zheng J, Luo L, Engelhard MH, Bowden ME et al. Complete Decomposition of $Li_2CO_3$ in Li–$O_2$ Batteries Using Ir/$B_4C$ as Noncarbon-Based Oxygen Electrode. Nano Lett 2017;17:1417-24.

[266] Yang S, Qiao Y, He P, Liu Y, Cheng Z, Zhu J et al. A reversible lithium–$CO_2$ battery with Ru nanoparticles as a cathode catalyst. Energy Environ Sci 2017;10:972-8.

[267] Zhu YG, Jia C, Yang J, Pan F, Huang Q, Wang Q. Dual redox catalysts for oxygen reduction and evolution reactions: towards a redox flow Li-$O_2$ battery. Chem.Commun. 2015;51:9451-4.

[268] Zhu YG, Wang X, Jia C, Yang J, Wang Q. Redox-Mediated ORR and OER Reactions: Redox Flow Lithium Oxygen Batteries Enabled with a Pair of Soluble Redox Catalysts. ACS Catalysis 2016;6:6191-7.

[269] Ruggeri I, Arbizzani C, Soavi F. A novel concept of Semi-solid, Li Redox Flow Air ($O_2$) Battery: a breakthrough towards high energy and power batteries. Electrochim Acta 2016;206:291-300.

[270] Li X, Huang J, Faghri A. Modeling study of a Li–$O_2$ battery with an active cathode. Energy 2015;81:489-500.

[271] Huang J, Faghri A. Capacity Enhancement of a Lithium Oxygen Flow Battery. Electrochim Acta 2015;174:908-18.

[272] Horstmann B, Danner T, Bessler WG. Precipitation in aqueous lithium-oxygen batteries: a model-based analysis. Energy Environ Sci 2013;6:1299-314.

[273] Li Y, Dai H. Recent advances in zinc–air batteries. Chem Soc Rev 2014;43:5257-75.

[274] Grübl D, Danner T, Schulz VP, Latz A, Bessler WG. Multi-methodology modeling and design of lithium-air cells with aqueous electrolyte. ECS Transactions 2014;62:137-49.

[275] Andrei P, Zheng JP, Hendrickson M, Plichta EJ. Modeling of Li-Air Batteries with Dual Electrolyte. J Electrochem Soc 2012;159:A770-80.

[276] Kashchiev D, Van Rosmalen G. Review: nucleation in solutions revisited. Crystal Research and Technology 2003;38:555-74.

[277] Nývlt J, Söhnel O, Matachová M, Broul M. The kinetics of industrial crystallization, Elsevier 1985.

[278] Stevens P, Toussaint G, Caillon G, Viaud P, Vinatier P, Cantau C et al. Development of a lithium air rechargeable battery. ECS Transactions 2010;28:1-12.

[279] Rinaldo SG, Lee W, Stumper J, Eikerling M. Model-and theory-based evaluation of Pt dissolution for supported Pt nanoparticle distributions under potential cycling. Electrochem Solid-State Lett 2011;14:B47-9.

[280] Nielsen AE. Electrolyte crystal growth mechanisms. J Cryst Growth 1984;67:289-310.

[281] Mehta M, Bevara V, Andrei P. Maximum theoretical power density of lithium–air batteries with mixed electrolyte. J Power Sources 2015;286:299-308.

[282] Mersmann A. Calculation of interfacial tensions. J Cryst Growth 1990;102:841-7.

[283] Lang W, Zander R. Salting-out of oxygen from aqueous electrolyte solutions: prediction and measurement. Ind Eng Chem Fundam 1986;25:775-82.

[284] Kitaura H, Zhou H. All-solid-state lithium-oxygen battery with high safety in wide ambient temperature range. Sci Rep 2015;5:13271.

[285] He P, Wang Y, Zhou H. The effect of alkalinity and temperature on the performance of lithium-air fuel cell with hybrid electrolytes. J Power Sources 2011;196:5611-6.

[286] Danner T, Horstmann B, Wittmaier D, Wagner N, Bessler WG. Reaction and transport in $Ag/Ag_2O$ gas diffusion electrodes of aqueous $Li–O_2$ batteries: Experiments and modeling. J Power Sources 2014;264:320-32.

[287] Grübl D, Bessler WG. Cell design concepts for aqueous lithium–oxygen batteries: A model-based assessment. J Power Sources 2015;297:481-91.

[288] He K, Zu C, Wang Y, Han B, Yin X, Zhao H et al. Stability of lithium ion conductor NASICON structure glass ceramic in acid and alkaline aqueous solution. Solid State Ionics 2014;254:78-81.

[289] Li L, Zhao X, Manthiram A. A dual-electrolyte rechargeable Li-air battery with phosphate buffer catholyte. Electrochem Commun 2012;14:78-81.

[290] Li L, Fu Y, Manthiram A. Imidazole-buffered acidic catholytes for hybrid Li-air batteries with high practical energy density. Electrochem Commun 2014;47:67-70.

[291] Yang W, Salim J, Li S, Sun C, Chen L, Goodenough JB et al. Perovskite $Sr_{0.95}Ce_{0.05}CoO_{3-\delta}$ loaded with copper nanoparticles as a bifunctional catalyst for lithium-air batteries. J Mater Chem 2012;22:18902-7.

[292] Chen XJ, Shellikeri A, Wu Q, Zheng JP, Hendrickson M, Plichta EJ. A High-Rate Rechargeable Li-Air Flow Battery. J Electrochem Soc 2013;160:A1619-23.